576
5-14-79

LA-7771-MS
Informal Report

DR. 2575

Hot Dry Rock Energy Extraction Field Test: 75 Days of Operation of a Prototype Reservoir at Fenton Hill

Segment 2 of Phase I

University of California
LOS ALAMOS SCIENTIFIC LABORATORY
Post Office Box 1663 Los Alamos, New Mexico 87545

DISCLAIMER

UNITED STATES
DEPARTMENT OF ENERGY
CONTRACT W-7405-ENG. 36

LA-7771-MS
Informal Report
UC-66a
Issued: April 1979

Hot Dry Rock Energy Extraction Field Test: 75 Days of Operation of a Prototype Reservoir at Fenton Hill

Segment 2 of Phase I

Edited by
Jefferson W. Tester
James N. Albright

CONTENTS

ABSTRACT 1

1. INTRODUCTION AND SCOPE 1

2. EQUIPMENT DESCRIPTION AND OPERATING PARAMETERS 4
   2.1 Equipment 4
   2.2 Operations 7
   2.3 Operational Problems 8
   System Perturbations 8

3. RESERVOIR HEAT EXTRACTION CHARACTERISTICS 12
   3.1 Measurements and Data 12
   3.2 Thermal Drawdown Analysis 14
   3.3 Heat Extraction 15

4. RESERVOIR FLOW CHARACTERISTICS AND MODELS 19
   4.1 Flow Impedance 19
   4.2 Fracture System Size and Degree of Mixing 24
   4.3 Fluid Loss and Storage 30
   4.4 Injection and Production Zones 34
   4.5 Flow Models 36

5. FLUID GEOCHEMISTRY 42
   5.1 Major Element Analysis 42
   Procedures 42
   Results 43
   Preliminary Interpretation - Reservoir 56
   Preliminary Interpretation - Surface Equipment 64
   5.2 Trace Element Analysis 67
   5.3 Strontium Isotope Ratio Measurements 72
   5.4 Radon 77

6. MONITORING FOR INDUCED SEISMIC EFFECTS 87

7. SUMMARY OF SYSTEM PERFORMANCE AND MODELS 89

APPENDIX A: FRACTURE OPENING BY COOLING 99

APPENDIX B: THERMAL EFFECTS IN SPHERICALLY COOLED REGIONS 103

HOT DRY ROCK ENERGY EXTRACTION FIELD TEST: 75 DAYS OF OPERATION OF A PROTOTYPE RESERVOIR AT FENTON HILL

SEGMENT 2 OF PHASE I

Edited by

Jefferson W. Tester
James N. Albright

ABSTRACT

Results from the first extensive field test of a man-made hot dry rock (HDR) geothermal reservoir in low permeability crystalline rock are presented. A reservoir with a small heat transfer area was utilized to study the characteristics of a prototype HDR system over a shortened lifetime. The resulting accelerated thermal drawdown was modeled to yield an effective area of 8000 m^2. In addition to the thermal effects, this test provided an opportunity to examine equipment operation, water permeation into the formation, geochemical interaction between the circulating fluid and the rock and flow characteristics including impedance and residence time distributions. Continuous monitoring for induced seismic effects showed that no activity to a Richter threshold of -1.0 was detected during the 75-day experiment.

---

1. INTRODUCTION AND SCOPE

The major prerequisite for full-scale testing of the Los Alamos Scientific Laboratory's (LASL) Hot Dry Rock concept was achieved. By redrilling the production well, GT-2, at the Fenton Hill site along a planned trajectory, we intersected a low-impedance hydraulic fracture that directly communicated with the injection well, EE-1. It should be emphasized that the redrilling program of GT-2 was designed to produce the largest heat transfer surface area possible with the inherent geometric limitations of the wellbores and with an acceptable initial flow impedance of less than 21 bar-ℓ/s (20 psi/gpm). Having achieved this, the Hot Dry Rock (HDR) concept could be tested by establishing a high-flow

rate between wells at low wellhead differential pressures. Previously, the only communication with EE-1 had been through and between high-impedance fractures, and flow was insufficient to evaluate the heat-extraction concept.

In September, with much of the work on the surface plant of the energy-extraction loop nearly complete, a preliminary test of the entire system which includes the surface plant and downhole flow paths was conducted. During 96 h of closed-loop circulation, fluid total dissolved solids remained low (<400 ppm), water losses continually decreased, and no induced seismic activity occurred. The operating power level was 3.2 MW (thermal), and fluid temperature reached 130°C at the surface. This test demonstrated for the first time that heat could be extracted at a usefully high rate from hot dry rock at depth and transported to the surface by a manmade system. The test further indicated a high probability that no significant problem would be encountered during sustained operation of the system.

Full-scale operation of the loop occurred from January 27 to April 13, 1978. This part of Phase I is referred to as Segment 2 and was designed to examine the thermal drawdown, flow characteristics, water losses, and fluid geochemistry of the system in detail. In addition, the experimental area was closely monitored for induced seismic activity. Results of these studies are the major topic of this report.

Because the anticipated effective heat transfer surface area was small (<10 000 m^2), the Segment 2 test was structured to examine reservoir performance in a compressed time scale with accelerated thermal drawdown. From a practical point of view, a rapid drawdown rate will hasten the development of thermal stress cracks and hence our evaluation of the concept. To induce cracks into the fracture surface under the Fenton Hill reservoir stress conditions, an excess of 75°C of cooling is required to produce cracks wide enough to provide low-impedance flow paths.[1,2]

It was planned that circulation flow rates would be maintained at their maximum values as determined by the system impedance and the maximum possible drop across the reservoir. With an initial impedance of 11-16 bar-s/ℓ (10-15 psi/gpm), circulating flows of about 6-10 ℓ/s (100-150 gpm) were anticipated. With this flow rate and an active fracture surface area of 10 000 m^2, about 90°C of cooling might occur after 60 days with no change in reservoir size due to thermal stress cracking or other effects. Consequently,

the difference between observed and calculated thermal drawdown could be used to identify changes in reservoir size. In addition, changes in fluid chemistry, water losses, residence time, flow impedance and production zones in GT-2 would be used to correlate with observed thermal effects.

The major purpose of the Phase I test was to evaluate hot dry rock reservoir engineering concepts in a prototype system. This evaluation will improve reservoir design and modeling capabilities to aid in the development of larger in-situ surface areas required for future commercial systems. The plans for Phase II are to enlarge the present reservoir to a capacity of 20-50 MW(t) with extended lifetime by directionally drilling to a deeper region (~250°C) and produce a multiply fractured system between two high-angle inclined wellbores.

This report is divided into seven sections. The surface circulation loop equipment and instrumentation are described in Section 2. Thermal behavior of the reservoir and associated heat extraction modeling results are presented in Section 3, with flow characteristics and water permeation effects covered in Section 4. Major and trace element geochemistry and kinetic flow models appear in Section 5, while reconnaissance data for induced seismic effects are discussed in Section 6. Section 7 summarizes the physical, geometric, and chemical behavior of the reservoir. In order to develop a consistent model the effects of hydraulically activated, parallel, natural joints are coupled to a vertical fracture system producing the existing flow connections between EE-1 and GT-2B. This report assumes that the reader is familiar with the chronological drilling sequence. It also assumes a familiarity with the geometry of the wellbores including the original EE-1 wellbore and the GT-2 wellbore with its sidetracked trajectories GT-2A and GT-2B. Readers who need a review of this background information should read Section 7 as a further introduction to the preceding sections.

2. EQUIPMENT DESCRIPTION AND OPERATING PARAMETERS (J. H. Hill, R. H. Hendron, E. Horton, B. R. Dennis, and the Geothermal Operations Staff)

2.1 Equipment

Equipment used in this segment of Phase I included the makeup system, the main circulating pumps, the control valve, the heat exchanger, the surface piping, the vent system, pressure lock system, and flow meters. The schematic of the loop (Fig. 2-1) shows the component locations. Pressure, temperature, and flow measurements are indicated by P, T, and F symbols respectively.

The makeup system furnished the initial water to fill the entire loop and any makeup water required during the run. The principal feature was a two-stage centrifugal pump capable of 8.2-ℓ/s (130-gpm) flow at ∿13.1 bar (190 psi). The water was drawn from the EE-1 reserve pond with a capacity of 1.5×10^6 liters (400 000 gal). Makeup water was supplied at a maximum rate of ∿2.5 ℓ/s (40 gpm) from a 122-m (400-ft) deep well.

Each centrifugal circulating pump module had seven vertical stages capable of raising the pressure 41 bar (600 psi). Two pumps were used in series

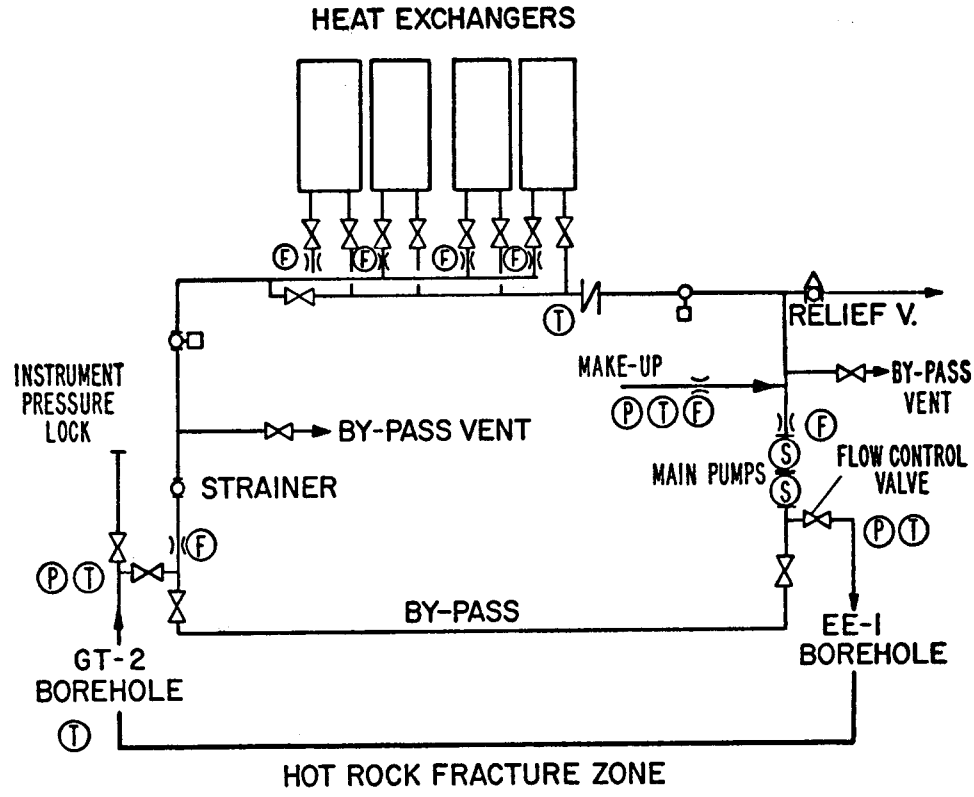

Fig. 2-1.
Schematic of the Fenton Hill circulation loop.

with an inlet pressure of 12 bar (175 psi) to produce a discharge pressure of 95 bar (1375 psi). Each pump module was driven by a 200-hp electric motor and on the flat part of the performance curve could deliver up to 32 ℓ/s (500 gpm). The final control element, located at the EE-1 wellhead, was a 5.0-cm (2-in.), linear trim, high-pressure, hand-controlled valve with an operating characteristic C_v of 14.6.

The water-to-air heat exchanger units were arranged for vertical forced draft across aluminum-finned, carbon steel tubes. The straight-tube sections with plugged headers may be mechanically or chemically cleaned in the event of scaling. Design point conditions were: 172 bar (2500 psi) working pressure; 12.1 MW(t) per bay of two tube bundles with an inlet water temperature of 250°C and a 65°C outlet, air inlet at 21°C, and a total flow of 18.3 ℓ/s (290 gpm) per module. Each bay was cooled by two axial flow fans driven by 30-hp motors. The louvers were automatically controlled to maintain a specified exit temperature.

The majority of the surface piping was 10 cm (4 in.) Schedule 160 carbon steel with a working pressure of 172.4 bar (2500 psi). The last 1 m of piping at the EE-1 borehole was 5.0-cm Schedule 160 and included the control valve mentioned above. The bypass vent system immediately downstream of the GT-2 wellhead leading to the GT-2 pond was included for start up, and the 5.0-cm line could isolate the flow from the heat exchangers, if required. The instrument pressure-lock system for the wellheads enabled borehole logging, tool retrieval, and reinsertion of a tool during operation of the system. Other equipment used in this system were a 15-cm (6-in.) gate valve, a water-cooled section of 19-cm (7 5/8-in.) casing, and a "control head" to pack off the cable. Seven venturi flow meters were placed throughout the loop to measure flow. In addition a totalizer (water meter) integrated the makeup water.

The Control and Data Acquisition System (CDA) used a Hewlett Packard 3050 B data acquisition system that consisted of a Hewlett Packard 9830 calculator and its peripheral equipment as shown in Fig. 2-2. During the 75-day run, 20 channels of loop information were recorded: 7 flow rates, 8 pressures (3 in line and 5 differential across heat exchanger tube bundles) and 5 temperatures. In addition to the loop instrumentation, 80 channels of thermocouple data were recorded. These thermocouples were strategically located on the heat exchanger to study possible scaling or fouling problems.

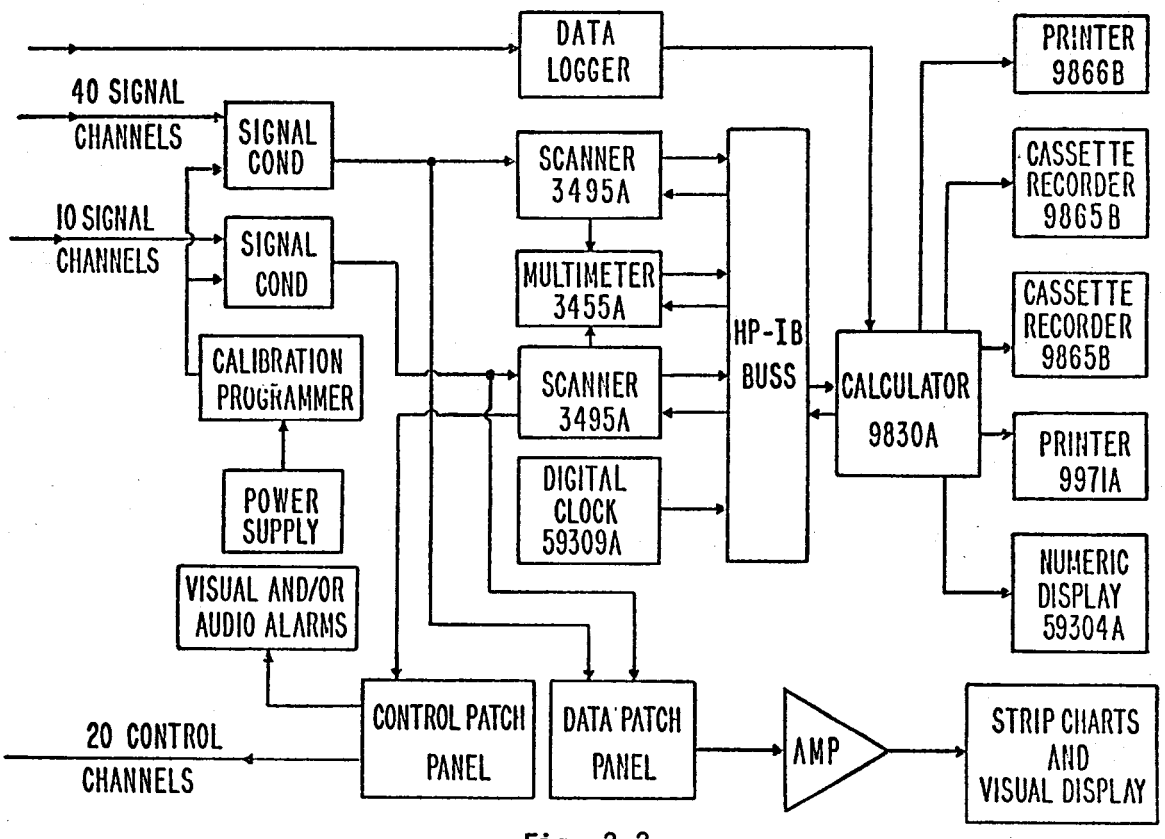

Fig. 2-2.
Schematic diagram of Control and Data Acquisition System.

Flow rates were measured with venturi meters using differential pressure transducers. Pressures were measured with pressure transducers, and Chromel-Alumel thermocouples monitored the temperatures.

All loop signals were hard-wired from the transducers and thermocouples to the signal conditioners, which provided power, shunt calibration, and balance networks for the transducers. The outputs of the signal conditioner were connected to an HP 3495 A scanner consisting of six decades of low thermal relays and two decades of actuators (control relays). The calculators controlled each relay individually allowing the HP 3455 A multimeter to read any selected data channel. The multimeter then passed the voltage reading upon command to the calculator via the HP-IB buss. The HP 9830 calculator then performed the necessary calculations and transmitted the reduced data to the 59304 A numeric displays and the 9971 A line printer, while the raw data went to the HP 9865 B cassette recorders.

In addition, the 80 heat-exchanger thermocouple channels were hard-wired directly to a data logger, which entered the data into a buffer. On command, individual thermocouple outputs were transmitted to the HP 9830 calculator in ASCII code.

Control functions for the Phase I loop during this run were minimal. The CDA operator could manually start and stop four fans on the heat exchanger and manually stop the makeup pumps and main circulating pumps. The HP 9830 was programmed to check all measurements for predetermined minimum and maximum values. If these parameters were exceeded, the calculator would sound an alarm and define the problem with a printed statement. If the problem could possibly result in damage to the pumps, the calculator would also turn off all pumps automatically.

The numeric displays were updated every 15 seconds. All data channels were recorded on magnetic tape and on the line printer at 15-minute intervals. If any one of the predetermined parameters mentioned was exceeded, the recording interval changed to one minute. In addition, certain experiments during the loop operation required more frequent output.

An uninterruptible power supply backed up the local power to prevent loss of data.

2.2. Operations

Operation began with the pumps drawing makeup water from the EE-1 storage pond. Within a few minutes, the output pressure at GT-2 reached 12 bar (175 psi) and the main circulating pumps were turned on. This level of back pressure was used to avoid flashing in the system. Fluid was injected into the EE-1 borehole, pumped through the fracture system, and out of GT-2, where the flow was vented to the GT-2 pond to clean out the system in an initial purge. After approximately 150 000 liters (40 000 gal.) of water had been vented and the outlet total dissolved solids was <400 ppm, the flow was then routed through the heat exchangers and back to the main pumps. The closed loop was then in operation. The inlet pressure to the main pumps was controlled by the makeup pump pressure, which in turn was controlled by a back pressure valve. This valve was set at 12 bar (175 psi), and it automatically diverted the makeup flow to the EE-1 holding pond when that pressure was exceeded. As the return flow from the heat exchanger gradually increased, the makeup flow was proportionately reduced. The EE-1 borehole pressure was kept below 90 bar (1300 psi) to avoid fracture extension. As the pressure approached 90 bar, flow was throttled at the control

valve. After a few days the pressure and flow had stabilized at ∿ 90 bar and 7.9 ℓ/s (125 gpm). (A schematic of the surface facility is shown in Fig. 2-3.

After three weeks of operation in this mode, the impedance of the fracture system started to decrease. This created a demand for a higher injection flow rate to maintain the wellhead pressure at 1300 psi. The control valve was opened to increase the rate. Finally, the control valve was wide open, with the injection rate at approximately 17 ℓ/s (270 gpm), and the 90-bar injection pressure could not be maintained as the impedance continued to decrease. At that time, we decided to control the flow rate at 14.5 ℓ/s (230 gpm). This was a compromise due to our concern for the inordinately high fluid velocities in the 5.0-cm piping at EE-1, and also for the desired flow and what could be achieved. The loop was operated under these constraints until it was "shut in" on April 13, 1978. This condition was maintained for 10 days, and then the system was vented.

2.3. Operational Problems

The operation of the system for the 75-day period was without major problems with a total of only 2% down time. Figure 2-4 indicates the shutdown periods greater than 1 h occurring during the 75-day run. Following are some of the specific problems.

The main pump seals failed within the first few days of operation. The seals were changed in the field by the pump manufacturer on day 18 and have since operated without mishap. The total downtime was ∿6 hours. The seals on the makeup pump failed near the end of the test, and a substitute pump was temporarily connected to carry the operation through the last 3 days. The turbine meter failed after 4 days, then operated intermittantly during the remainder of the test. The control head on the pressure lock system leaked excessively >38 ℓ/min (>10 gpm) after 65 days of operation because of progressive degradation caused by repeated temperature logging performed almost daily during that period. The temperature probe had to be removed from the hole, and the control head rebuilt.

Power to the site was furnished by Jemez Electric COOP. Most of the run was conducted during the winter months, and there were frequent momentary power interruptions, which caused pump failure for short periods. More serious power failures occurred on two occasions when power was out in excess of 12 hours. Because these outages occurred during winter storms, special efforts were needed to prevent freezing the exposed plumbing.

System Perturbations. The loop operation was perturbed at times by excessive flow. Ordinarily, the fracture system acts as a large (>38.0-m^3) accumulator

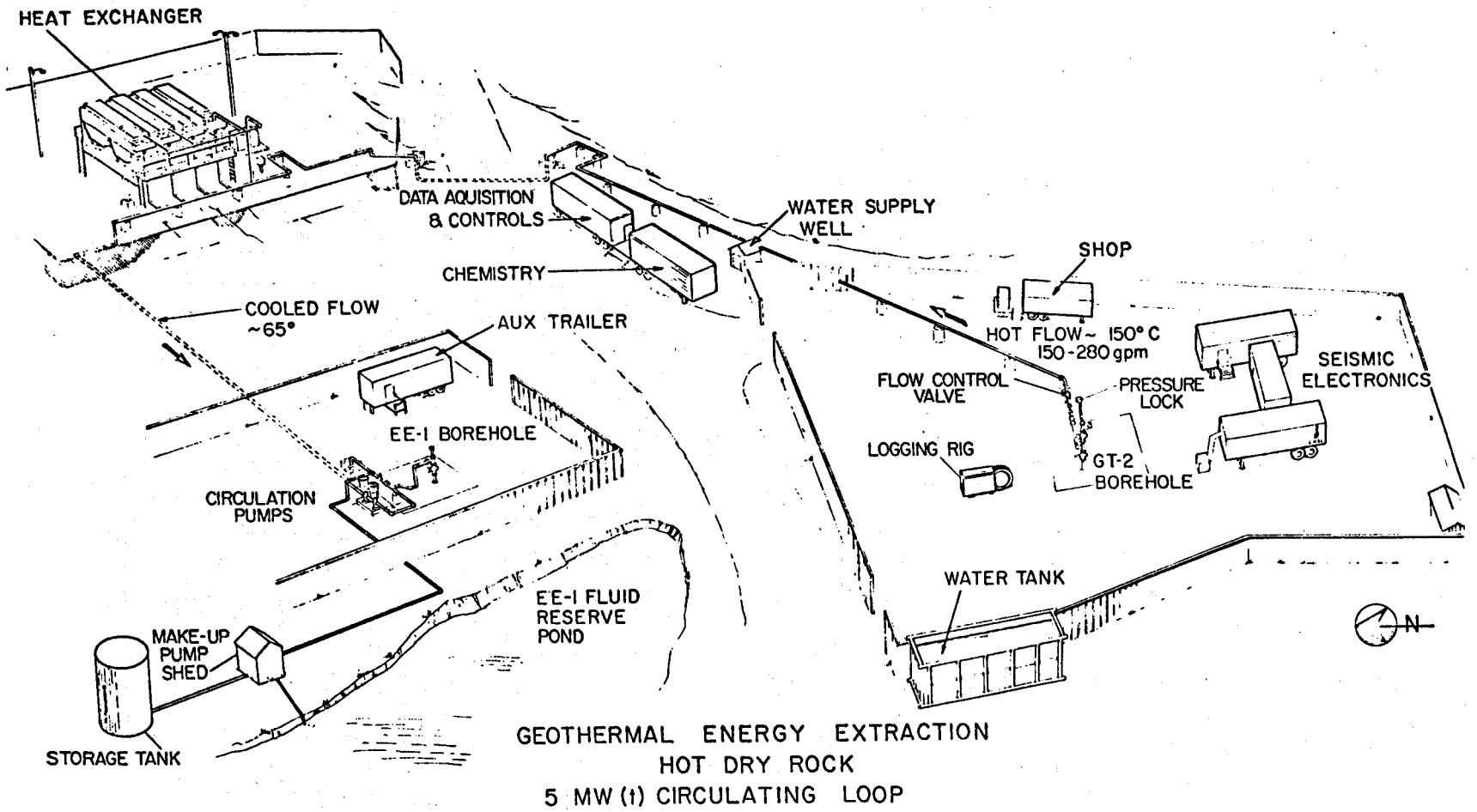

Fig. 2-3.
Fenton Hill surface facility showing major components and structures.

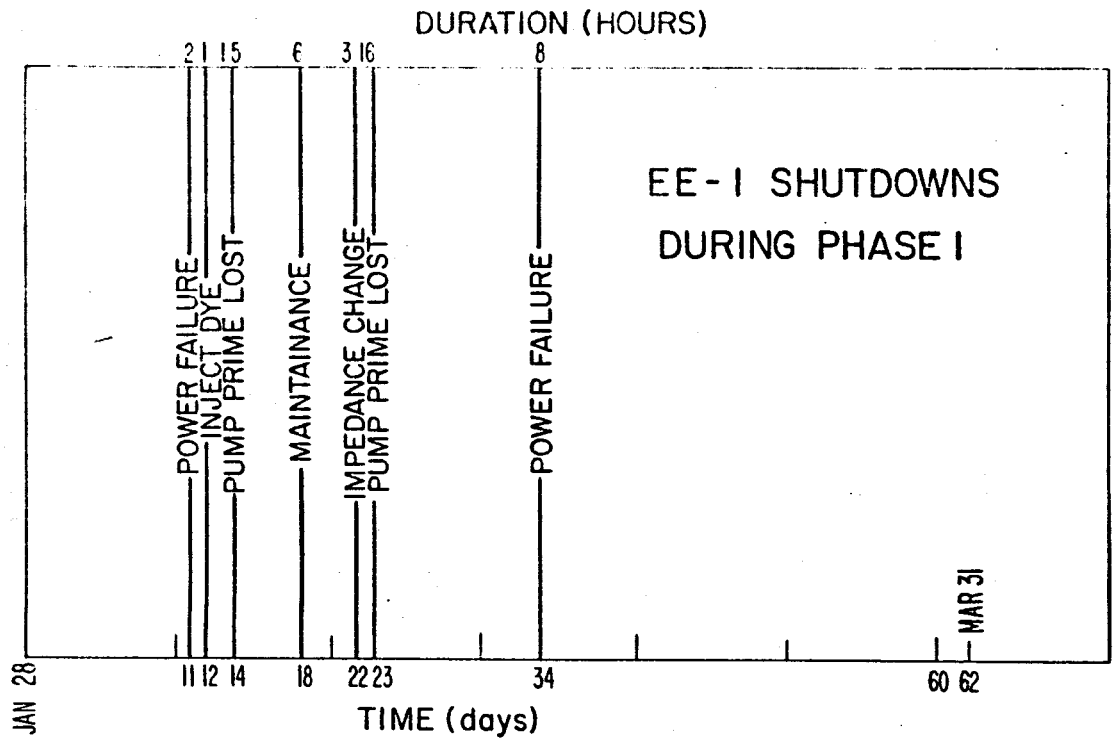

Fig. 2-4.
Indicated shutdowns during Phase I greater than 1 h in duration.

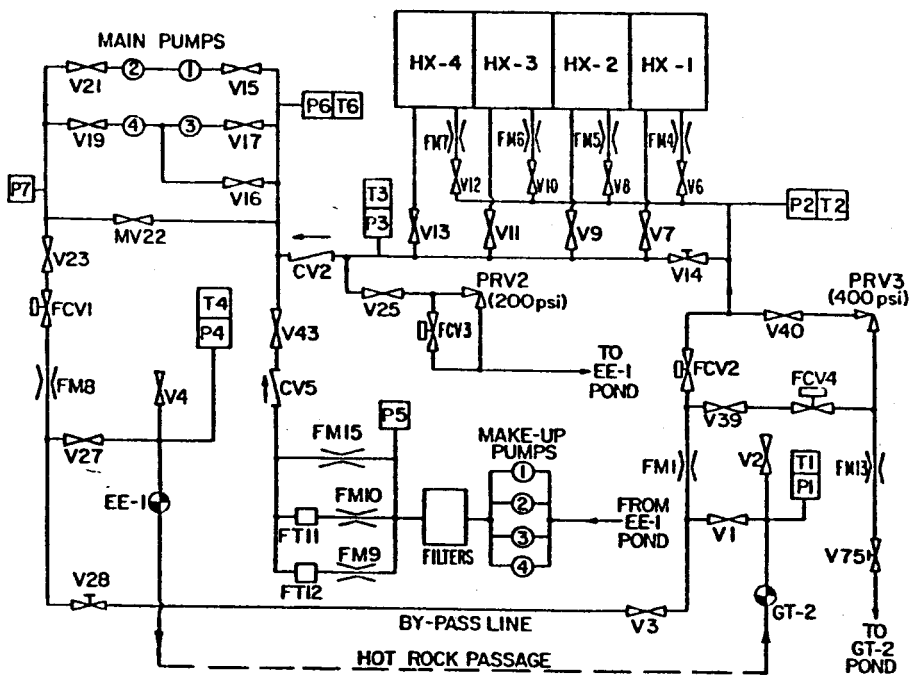

Fig. 2-5.
Schematic of the Fenton Hill circulation system with modifications.

where the output flows through a restriction or impedance. If this restriction is suddenly reduced, a higher flow out of the reservoir will result. This occurred several times, and twice the change in impedance was sufficient to cause problems in loop operation. At these times there were increases in the flow from the production wellbore, the flow and temperature to the heat exchanger, and the heat exchanger exit flow and temperature. When the pump inlet pressure exceeds the makeup limiting discharge pressure, the makeup flow ceases. When the heat exchanger output temperature (pump inlet temperature) exceeds the specified limit for the seals, the pumps are programmed to shut down. In two instances, the loop was shut down automatically by these perturbations, at one time for as long as 3 h as shown in Fig. 2-4. It took many hours to get the system running smoothly after a large change in impedance. This involved adjusting flow rates, makeup pressures, heat exchanger louver settings, and throttle valve settings.

To streamline operation and increase injection flow capacity, several modifications to the loop have been made as shown on Fig. 2-5. These are (1) the installation of a new makeup pumping system with a capacity of ∿14.2 ℓ/s (225 gpm), (2) the addition of flow control valves at GT-2 (FCV2 and FCV4) to maintain smooth operation when perturbations in reservoir impedance or flow occur, (3) the installation of two new multistage centrifugal pump units to increase circulation rate capacity to ∿32.6 ℓ/s (500 gpm) at a differential pressure of 93 bar (1350 psi), (4) the addition of an antifreeze circulation system to avoid freeze up during emergency shutdowns, and (5) installation of a larger capacity flow control valve and piping at EE-1 to accommodate up to 40 ℓ/s. A pressure lock system was also installed at the EE-1 wellhead to allow logging in EE-1 during operation.

3. RESERVOIR HEAT EXTRACTION CHARACTERISTICS (H. Murphy)

3.1. Measurements and Data

Injection and production flow rates were measured with venturi meters and differential pressure transducers. Surface injection and production temperatures were measured by thermocouples inserted into the wellheads. In addition, a temperature surveying tool with a 0.05°C resolution employing a thermistor was positioned downhole in the GT-2B production well for almost the entire duration of the test. A total of 58 logs or surveys were taken during the 75-day run. Between surveys the tool was stationed at 2.6 km (8600 ft), just above all the known producing zones in GT-2B. In this fashion the mean temperature due to the mixed fluid flows converging upon GT-2B was continuously monitored.

A typical set of temperature surveys is presented in Fig. 3-1. Only the downhole region where the produced fluid enters the well is shown. The uppermost survey was obtained on February 4, 1978, 7 days after the start of power production, while the middle and lower surveys were obtained after 12 and 16 days, respectively. Even a cursory look at these surveys indicates a complex reservoir-to-production well connectivity. The major temperature changes at the depths indicated with arrows are associated with flow connections identified in earlier testing.[3] (See Section 4.4 also). These earlier results showed that 20% and 80% of the flow enter the deepest and next deepest of these four main connections whereas the flow rates in the upper two were too small to be measured. The more precise logs taken during Segment 2, in which digitized temperature data were obtained every 0.15 m, showed that even these major connections seemed to have fine structures that changed with time. For example, both major connections 1 and 2 actually consist of two connections each. At connection 2, a colder flow rate entered at the bottom, but 2 meters farther up, water at least 5°C hotter entered the well. The second survey and even more visibly the third survey show the development of new flow connections located between the previously established major connections 1 and 2, and in fact, the magnitude of the temperature change at 2.68 km (8800 ft) suggests that a major connection has developed there. In Section 4.4 this information along with flowing spinner surveys and radioactive tracer logs are used to characterize the production and injection zones.

Figure 3-2 presents the variation of temperature at 2.6 km (8500 ft) with time. As stated earlier, the measurement is made above all the flow connections

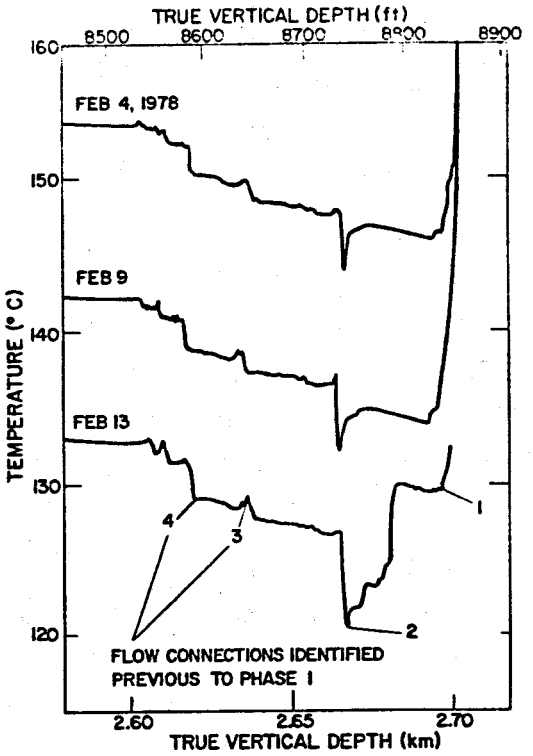

Fig. 3-1.
Three temperature surveys taken in the bottom section of GT-2B during Phase I.

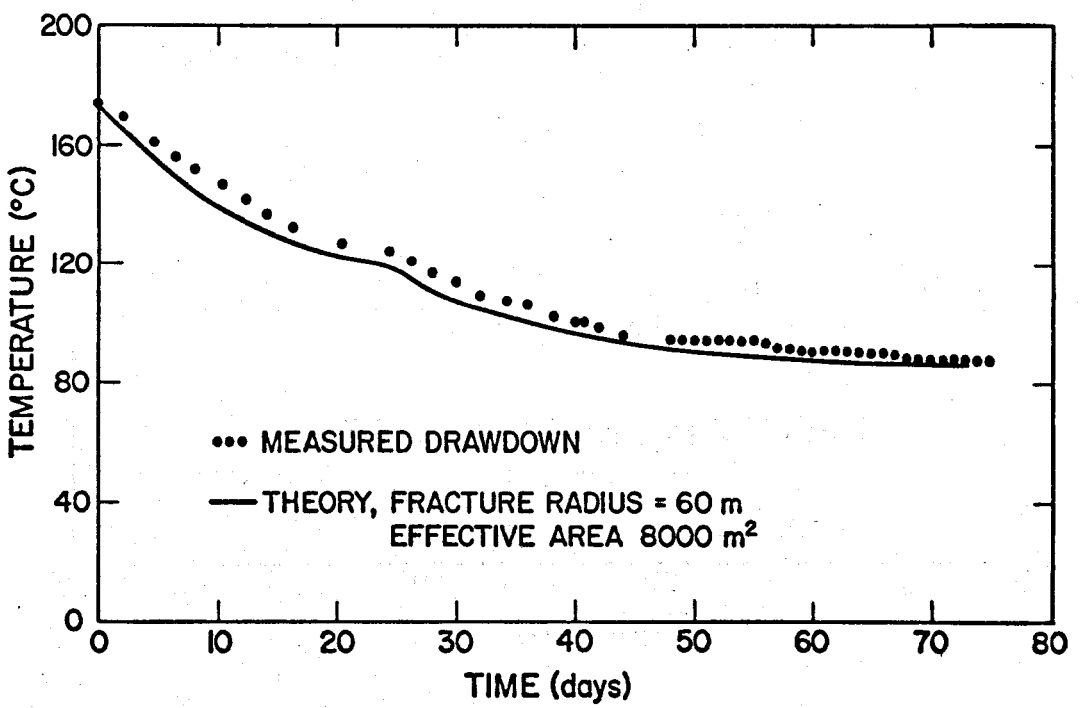

Fig. 3-2.
Thermal drawdown of produced fluid measured at a 2.6 km (8500 ft) depth in GT-2B.

so that the temperature represents the mean temperature of the mixed fluid in the production wellbore and thus provides an indication of the overall thermal drawdown of the reservoir. Figure 3-2 also shows the predicted drawdown for a reservoir with a surface area (one side only) of 8000 m^2 ($8.6 \times 10^4 ft^2$). These theoretical results are described in the next section. The "scallop" in Fig. 3-2 results from a doubling of the production flow rate.

Figure 3-3 presents the net thermal power produced using a constant 25°C surface reinjection temperature in the calculation. Despite the declining production temperatures, the increasing flow rate allowed the power to be kept roughly constant for the last 40 days. Peak power was 5 MW(t).

3.2. Thermal Drawdown Analysis

To interpret the drawdown results of Fig. 3-2 in terms of effective heat transfer area it was assumed that the fracture system could be described as a single circular fracture. This is indeed an approximation -- the actual fracture need not be circular, and in fact multiple fractures may be possible,[3] but our

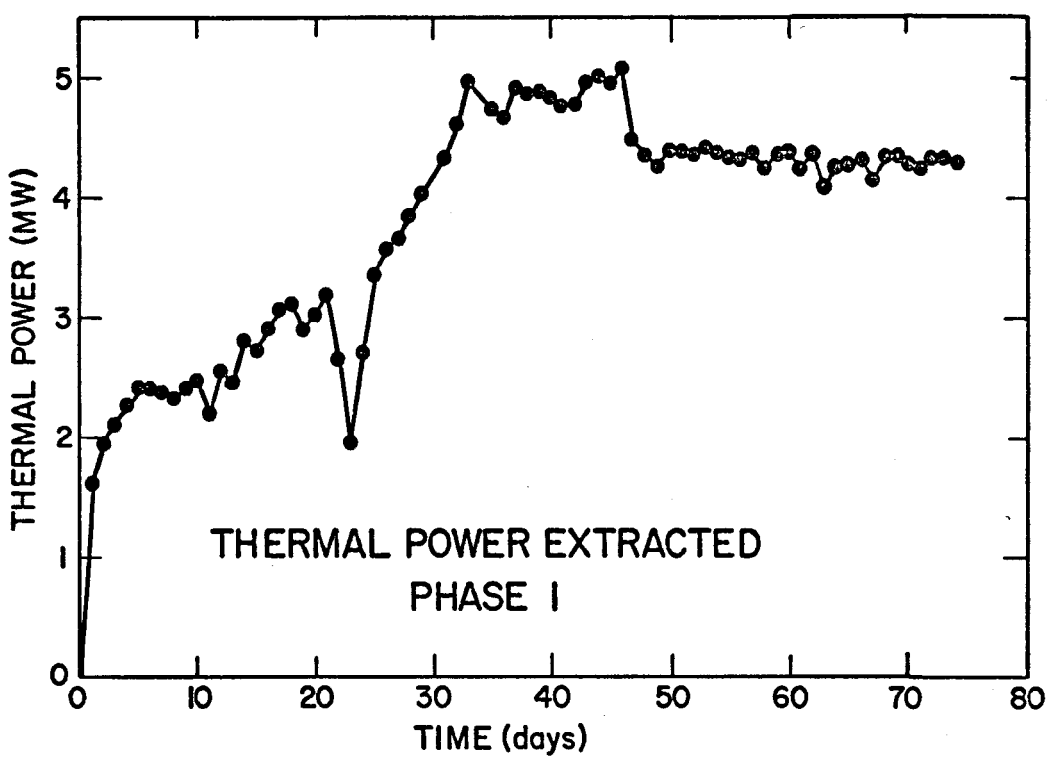

Fig. 3-3.
Net thermal power extracted during Phase I.

intent is to provide an estimate of the fracture area effective for heat transfer; thus the assumption of a single circular fracture is reasonable for a first estimate.

Because the hydraulic fracture itself is much more permeable than the surrounding rock, it was assumed that fluid was confined to the fracture and that heat from the rock was transported to the fluid in the fracture only by means of thermal conduction in the rock. (The possible enhancement of the heat transfer area because of thermal stress cracking is not considered in this model.) In fact, a small amount of fluid did penetrate the surrounding rock, particularly at very early times as evidenced by the makeup losses. (See Section 4.3.) To correct for this effect fluid loss was assumed to occur uniformly over the fracture area. Thus the permeation effect can be approximated by assuming that on the average, heat was removed from the reservoir by all of the produced water flow and half the difference between the injected and produced water flows.

3.3. Heat Extraction

To model the heat extraction process, several equations related to the fluid in the fracture and the surrounding rock are important. In the fracture plane, the horizontal coordinate is taken as x, the vertical coordinate as y. Solid rock heat conduction takes place along the z-coordinate, perpendicular to the x-y fracture plane. Using Darcy's law for flow in the open fracture with a permeability or hydraulic conductivity of $\frac{w^2}{12}$, the flow velocities u and v in the x and y directions are, respectively:

$$u = - \frac{w^2}{12\mu} \frac{\partial P}{\partial x} \qquad \text{and} \qquad (3\text{-}1)$$

$$v = - \frac{w^2}{12\mu} \left[\frac{\partial P}{\partial x} - \rho g \beta (T - T_o) \right], \qquad (3\text{-}2)$$

in which

- w = fracture aperture or width
- P = pressure
- μ = viscosity
- t = time
- T_o = reference temperature, eg. fluid injection temperature
- T = temperature of the fluid
- T_r = initial equilibrium rock temperature

g = acceleration of gravity

β = volumetric expansion coefficient of fluid

λ = thermal conductivity of rock

θ = temperature of the rock

ρ = fluid density

e = the flux of energy delivered to the fluid by one rock surface evaluated as $e(t) = \lambda \frac{\partial \theta}{\partial z}(x,y,z = 0,t)$

c = specific heat capacity of fluid,

and where the last term in the equation for v represents the effects of buoyancy.

By making the Boussinesq approximation, the equations of conservation of mass and energy in the flowing fluid are:

$$\frac{\partial}{\partial x}\left(\frac{w^3}{\mu}\frac{\partial P}{\partial x}\right) + \frac{\partial}{\partial y}\left[\frac{w^3}{\mu}\left(\frac{\partial P}{\partial y} - \rho\beta g(T - T_o)\right)\right] = 0 \quad \text{and} \tag{3-3}$$

$$\rho c w u \frac{\partial T}{\partial x} + \rho c w v \frac{\partial T}{\partial y} - 2e = 0 \quad , \tag{3-4}$$

Finally, the rock conduction equation is

$$\frac{\partial \theta}{\partial t} = \frac{\lambda}{\rho_r c_r}\frac{\partial^2 \theta}{\partial z^2} \quad , \tag{3-5}$$

where ρ_r and c_r are the density and heat capacity of the rock, respectively. Equation (3-5) is subject to the initial and boundary conditions

$$\theta(x,y,z,t=0) = T_r \quad , \tag{3-6}$$

$$\theta(x,y,z=0,t) = T(x,y,t) \quad , \text{ and} \tag{3-7}$$

$$\theta(x,y,z\to\infty,t) = T_r \quad . \tag{3-8}$$

These coupled nonlinear partial differential equations are solved numerically.[4,5]

In the calculations, the observed time variations of production and injection flow rates as well as the reservoir injection temperature were used. Initial equilibrium rock temperatures and their variation with depth were determined from borehole equilibrium temperature surveys. The downhole temperature variation was calculated by the WELLBOR code.[6] Heat transfer causes this variation by radial conduction to the convecting fluid as it is pumped down the injection well. The measured wellhead temperature and injection flow rate at

EE-1 were used as initial conditions. The accuracy of this estimate of fluid injection temperature as it enters the reservoir at 2760 m (9050 ft) can be assessed in Fig. 3-2, where the predicted downhole temperature variation in GT-2B is in good agreement with measurements. This calculation was performed using the measured downhole temperature (2.6 km or 8500 ft) on day 0 and the production flow rate, as initial conditions.

As hot fluid flows into the production wellbore and rises to the surface, it is cooled as the formation surrounding the wellbore is heated. The rate of wellbore heat loss declines continuously as the circulation continues. Consequently if fluid enters the production zone at a constant temperature, a monotomic increase in wellhead temperature approaching the production zone temperature is observed. When thermal drawdown occurs, it is superimposed on this wellbore heat loss effect. In the present system the production surface temperature peaked after 6 days because of the coupled effect of reservoir thermal drawdown and wellbore heat loss.

For these reservoir simulations, a constant value of 0.2 mm was assumed for fracture aperture (width), which results in an overall fracture impedance of 3 bar-s/ℓ (∿ 3 psi/gpm). During the early phases of the experiment, the impedance of the total system was actually as high as 16 bar-s/ℓ (15 psi/gpm) before being reduced to the former value. Earlier testing[2] showed that the total system impedance was composed of a main fracture impedance of 4 bar-s/ℓ (3.7 psi/gpm) and a fracture-to-production well impedance of 8 to 12 bar-s/ℓ (7.3 to 11 psi/gpm). This latter impedance resulted because the re-drilled production hole did not directly intersect the main fracture. The observed reduction of total impedance may simply reflect a reduction of this latter component, rather than a reduction of fracture impedance itself. Certainly, the new flow connections indicated in the production well temperature survey, Fig. 3-1, and the spinner survey results given in Section 4.4 suggest that the reduction occurred in the fracture-to-wellbore impedance.

Using the above data and assumptions, the simulator was run for several assumed fracture radii until the complete thermal drawdown history could be matched. The results for a 60-m (200-ft) radius fracture agreed quite well with the measurements, as previously shown in Fig. 3-2. Because of hydrodynamic flow inefficiencies, only about 75% of the fracture area actively transferred heat; so the effective heat transfer area was only 8000 m^2.

We emphasize that this is not a measure of the total fracture area accessible to water. The effective heat transfer area is strongly influenced by the vertical separation of the fracture water inlet and outlet locations. Because fracture flow impedances are ∿ 3-4 bar-s/ℓ buoyant forces will not significantly affect flow patterns within the fracture, and the water only partially fans out between the inlet and outlet points. Thus the effective heat transfer area swept by this flow is a direct function of the inlet and outlet spacing. In the present case the spacing between the inlet located at 2.76 km (9050 ft) in the injection well and the production well connection with the highest flow capacity is approximately 100 m. Roughly speaking, then, the effective area would be defined by a circle 50 m in radius, with an area of 7900 m^2, very close to that derived with the simulator.

The possibilities of reducing flow impedances and enhancing heat transfer area by means of thermal cracking as the reservoir cools and contracts were discussed by Murphy.[1] Subject to large uncertainties in our knowledge of the maximum horizonal earth stress, it was estimated that the effects of thermal cooling might be apparent after a cooling of about 75°C or more. A close scrutiny of the temperatures in Fig. 3-2 shows that starting at 48 days there is a period of 8 days in which the temperature was constant. Additional constant temperature intervals are noted starting at day 58, and then again on day 68. Each of these plateaus was terminated by stepwise decreases in temperature. Such behavior may have resulted from thermal stress cracking or possibly the enlargement of the heat transfer area by pore-pressure induced fracturing. Murphy suggested that a state might be sustained in which continued power production was matched by the continual creation of new heat transfer area, so that the temperature would remain essentially constant. To verify this hypothesis, an extended circulation period at the rate of 14.5 ℓ/s (230 gpm) would be required. Furthermore at this drawdown rate, a quasi-steady state condition exists where the decline rate is very small, making it difficult to discern changes due to fracture extension by thermal cracking or other effects. Future tests at higher circulation rates are planned as well as evaluation of the concept in deeper, hotter reservoirs where induced thermal stress would be higher.

4. RESERVOIR FLOW CHARACTERISTICS AND MODELS

4.1. Flow Impedance (R. L. Aamodt and R. M. Potter)

For the circulation system, the flow impedance is defined as the pressure drop through the fracture system connecting two wellbores divided by the flow rate. There is some ambiguity in the definition because the injected flow differs from the produced flow because of the fluid permeation rate into the rock surrounding the fracture. Conservatively, we adopted the production flow rate in the definition.

Since there were no downhole pressure gauges, the downhole pressure drop through the fracture system was obtained from the measured surface pressure difference between EE-1 and GT-2, corrected for the difference in fluid density between wells. This buoyancy correction requires a knowledge of the temperature distribution in each well. The corrections shown in Fig. 4-1 were derived from calculated wellbore temperatures during the first 3 weeks of operation as well as estimates based on surface and downhole temperature measurements at later times, with a few periodic checks obtained from GT-2B temperature logs over the entire wellbore.

The downhole temperature changed slowly at late times, as shown in Fig. 3-2. In addition, the injection well temperature fluctuated, but was generally lower in the last 6 weeks. As a result, the buoyancy correction remained almost constant during this time. A possible 20% error in buoyancy is reflected as less than 5% error in impedance, since the buoyancy correction was never more than 25% of the total measured pressure difference between EE-1 and GT-2B.

Figure 4-2 shows the measured impedance during the first 4 hours of the test. After a few minutes, the impedance oscillates between 14 and 17.5 bar-s/ℓ (13-16 psi/gpm), very near the steady state value of 17.5 bar-s/ℓ, which was observed on the second day through the sixth. This indicates that a large fraction of the initial flow came along a direct path with little or no diffusion in series with the path.

As seen in Fig. 4-3, the impedance began to fall after one week of flow. Figure 4-4 is an idealized graph of the flow and pressure history in EE-1. The maximum flow into EE-1 was limited by surface plumbing to less than 16 ℓ/s (250 gpm), and as the impedance dropped, it became impossible to maintain a constant injection pressure. Consequently it was decided to keep the injection flow rate constant at $\sim$ 14 ℓ/s ($\sim$ 230 gpm). This was generally done during the second

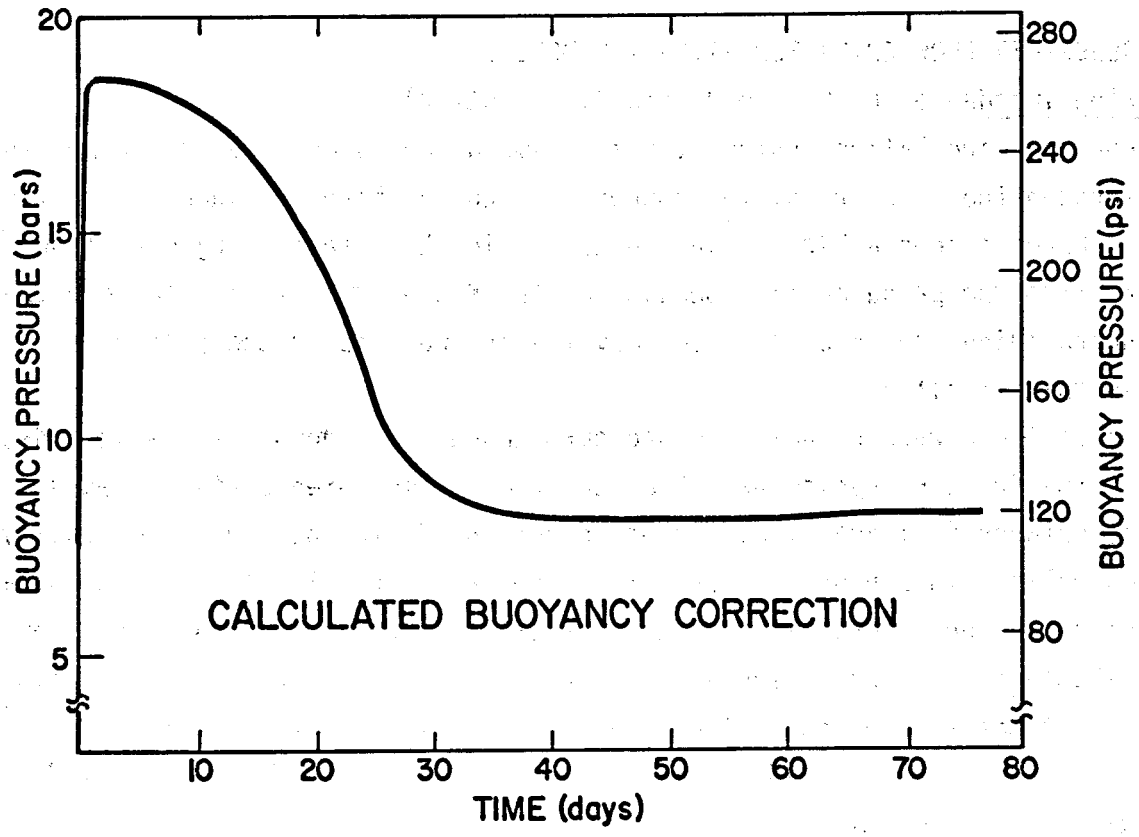

Fig. 4-1.
Calculated buoyancy correction between the GT-2B production and the EE-1 injection wellbores.

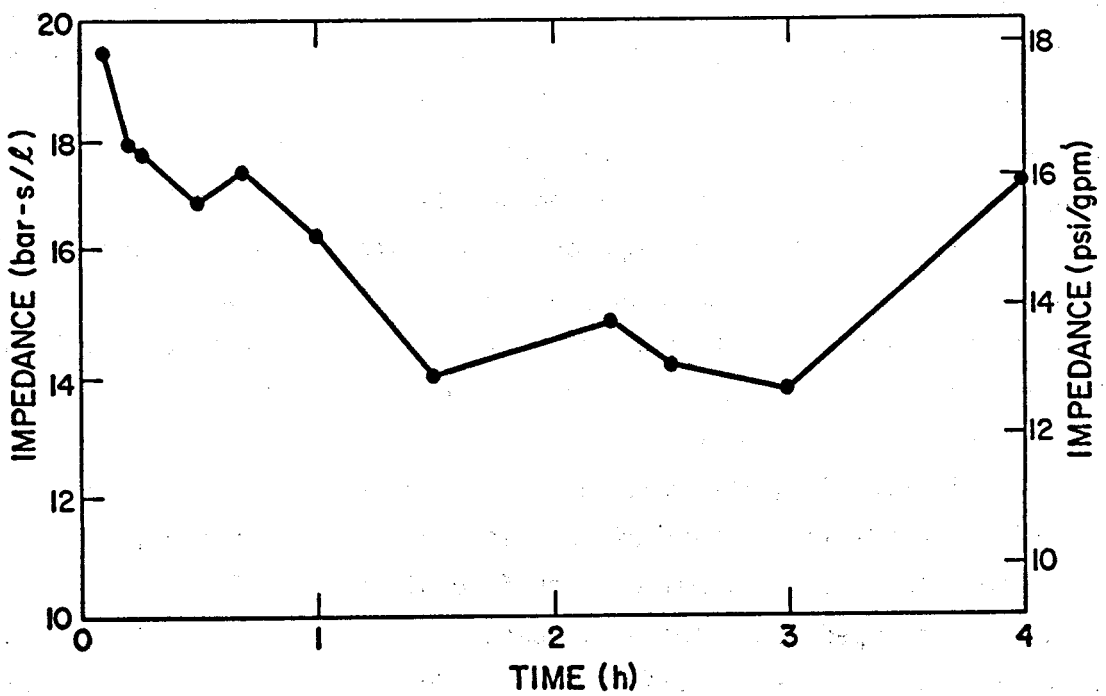

Fig. 4-2.
Early net flow impedance with buoyancy corrections included.

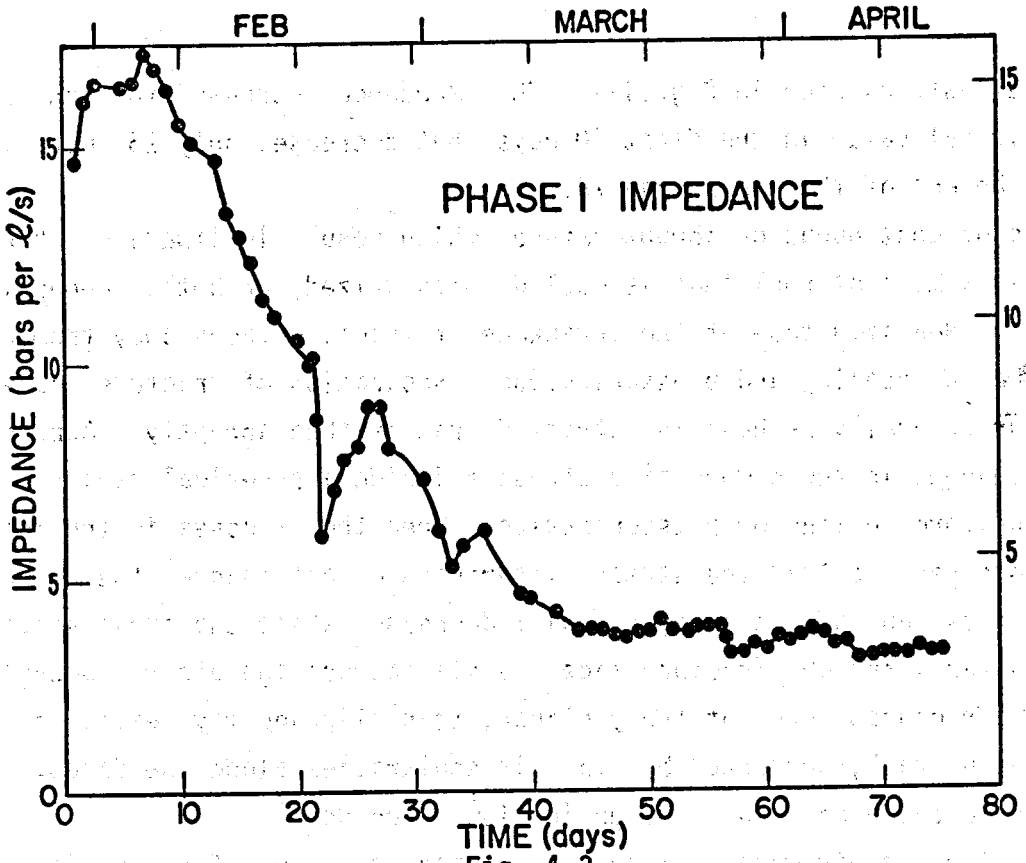

Fig. 4-3.

Net flow impedance between the GT-2B production and EE-1 injection wellbores with buoyancy corrections included.

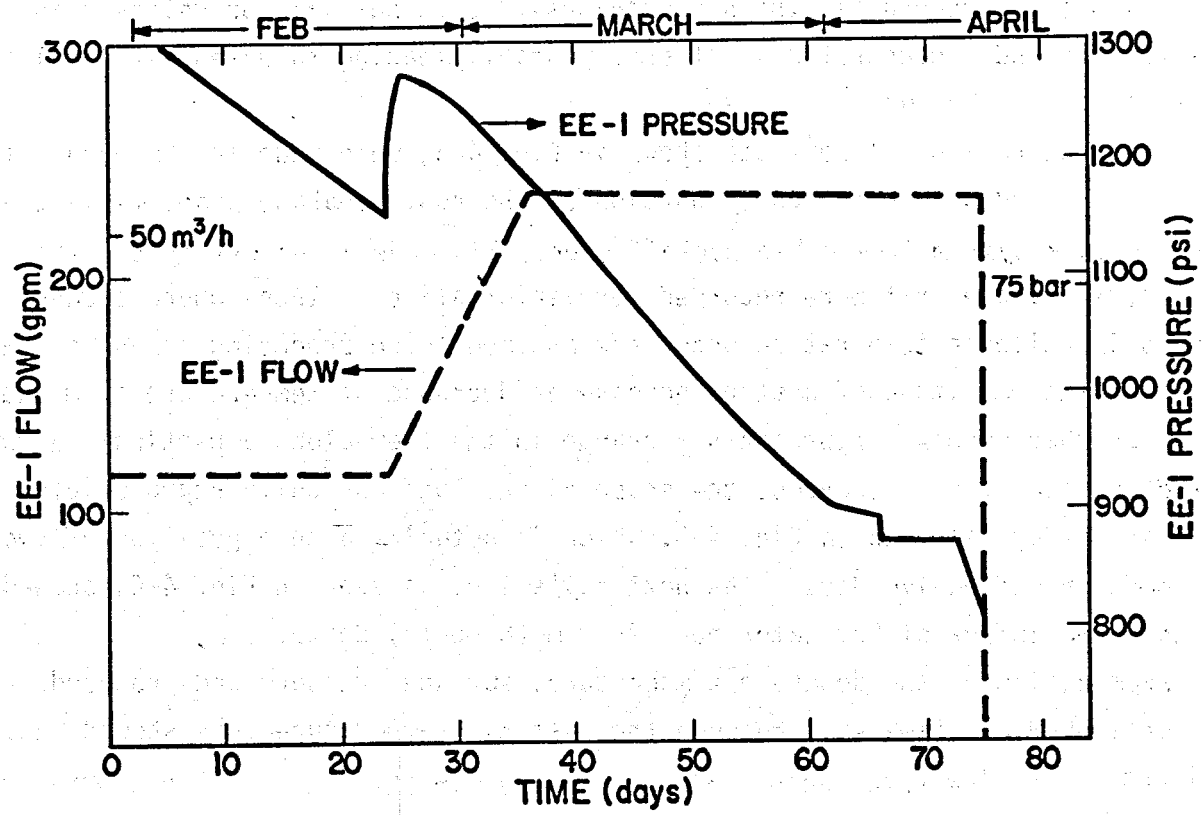

Fig. 4-4.

Idealized pressure and flow history at the EE-1 injection wellhead.

half of the test, as seen in Fig. 4-4. The impedance decreased to less than 1/3 the original value in the first 40 days, but decreased only 25% more from day 40 to the end of the run at day 75.

Events of continuous or abrupt nature, which result in impedance changes, can occur in a mass of rock that is cooled, pressurized, or both. Appendix A discusses an idealized case of the shrinkage of fracture faces away from each other, caused by cooling and pressurization. Separation of fracture faces should occur gradually as heat is extracted, rather than abruptly. Appendix B discusses changes in the compressive stresses inside a spherical region of rock, caused by uniform cooling or pressurization. When the stresses in the rock decrease together, so that the stress differences do not change, the normal stresses across many of the fractures will decrease, while the shear stress remains constant, and one fracture face may slip across the other. Because the pre-existing fractures were not truly planar, this slippage may result in a partially open crack, supported by small irregularities along the faces. Such an event would cause an abrupt change in flow impedance.

The real reservoir must be much more complex than any of these simple models, with both irregular regions of cooling and irregular regions of pressurization (not necessarily the same regions). Stresses will be relieved in some regions and concentrated in others, possibly leading to extensive localized rubblization of the rock.

Temperature logs, like those shown in Fig. 4-5, were made in the open hole portion of GT-2B during the early portion of the run. Leakage problems in the pressure lock system from cable packoff eventually made it necessary to omit these logs. Those that were recorded were informative. Places where sudden changes in wellbore temperature occur are assumed to be producing zones, and a change in the magnitude of a step increase or decrease of temperature from one log to another probably represents a change in the flow along a particular path. In the absence of such changes, the shape of the logs was quite reproducible from day-to-day, as seen in Fig. 4-5, which is actually a superposition of two logs made on successive days. The next day's log, as seen in Fig. 4-6, showed an increased influx of hot water near 2680-m (8800-ft) depth.

Examination of the downhole temperature, surface pressure and produced flow data over the time span between the last two temperature logs showed that an increase in flow rate, accompanied by changes in EE-1 and GT-2B pressure and

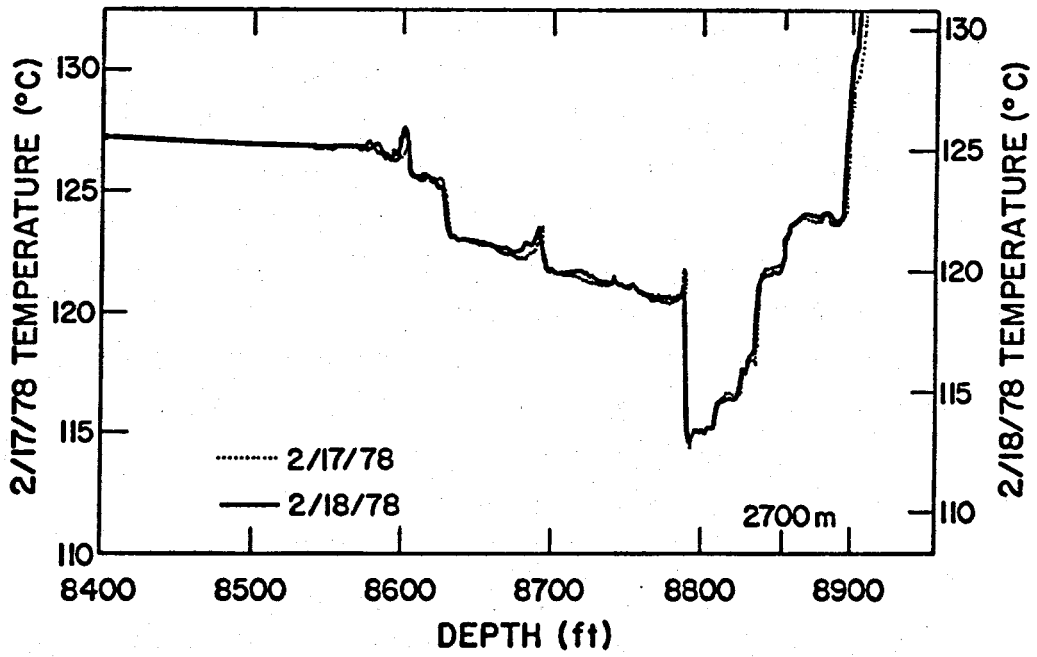

Fig. 4-5.
Temperature logs from the bottom section of GT-2B taken on February 17 and 18, 1978.

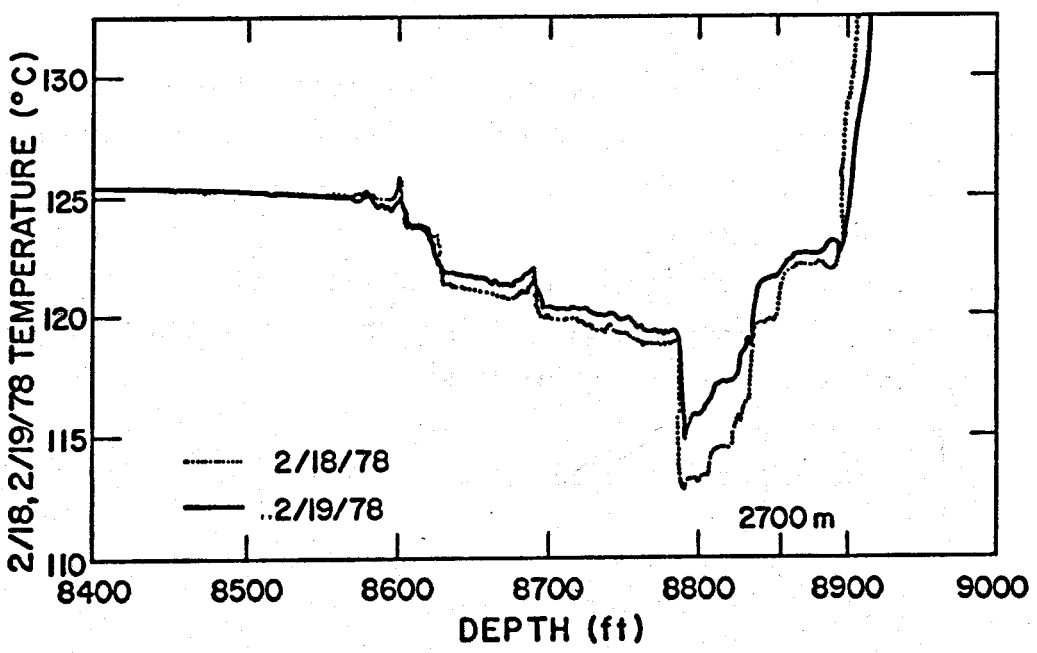

Fig. 4-6.
Temperature logs from the bottom section of GT-2B taken on February 18 and 19, 1978.

downhole temperature, occurred within a 15-min time span (the data-recording interval) just before 0100 in the morning of the second log. These changes are shown in Fig. 4-7 and 4-8. A number of such events were found in the records. When the logarithm of the number of events with step flow increases above a certain size was plotted against the logarithm of the size of the increase (Fig. 4-9), a straight line with a slope of -1 was obtained. Many small events must have been missed, but those which were observed were sufficient to account for over half the flow increase observed during the run. Thus, many of the events causing impedance changes took place within a short time span, possibly only fractions of a second. We concluded therefore that the rock may have undergone considerable dislocation during the 75-day test.

4.2. Fracture System Size and Degree of Mixing (J. W. Tester)

Dye tracer techniques developed previously[2] were used to characterize the fracture system volume and fluid residence-time distribution (RTD) within the reservoir during circulation. In the four experiments run during the 75-day test, a 200-ppm, 400-liter (100-gal) pulse of sodium-fluorescein dye was injected into the EE-1 wellhead, pumped down EE-1 and through the fractured region, and up the GT-2B wellbore. Dye concentration in the produced fluid was monitored spectrophotometrically at the surface as a function of time and volume throughput.

To evaluate the experimental residence time distributions several simple normalization procedures were used. The results of the four experiments and their statistical analysis are summarized in Table 4-I and Fig. 4-10. The distributions have been characterized using integral (first moment) mean volumes, median volumes, integral mean volumes using a trimmed section of the distribution, and variances of the normalized distributions. These can be expressed using the following equations and definitions:

$$C_\theta = C_i \Big/ \left[\frac{1}{\bar{V}} \int_0^\infty C_i dV\right] = \text{normalized concentration} \qquad (4\text{-}1)$$

$$\langle V \rangle = \int_0^\infty VC_i dV \Big/ \left[\int_0^\infty C_i dV\right] = \text{integral mean volume} \qquad (4\text{-}2)$$

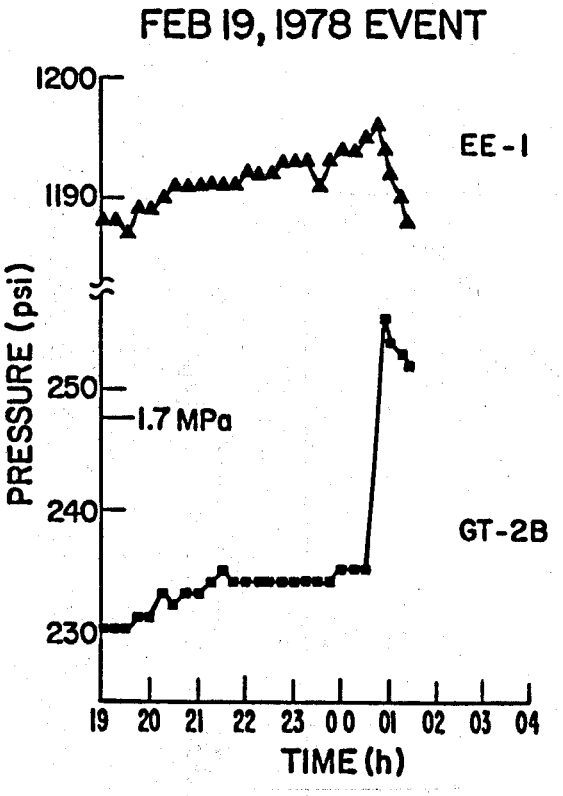

Fig. 4-7.
GT-2B and EE-1 surface pressure histories near the February 19, 1978 event.

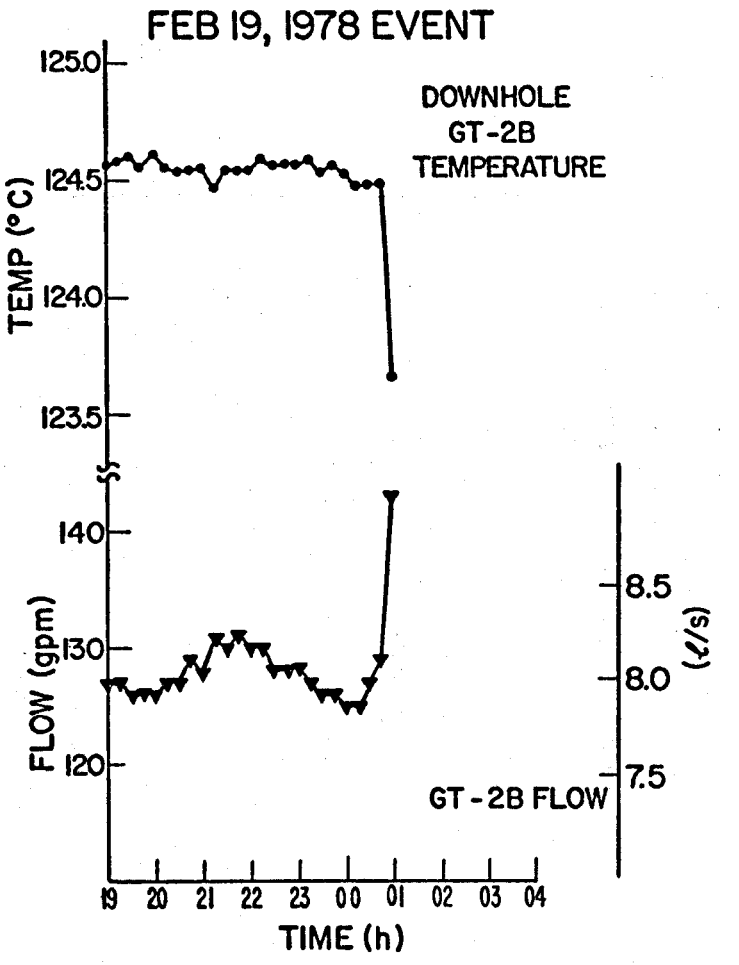

Fig. 4-8.
Downhole temperature at 2.8 km (8500 ft) in GT-2B and production flow histories near the February 19, 1978 event.

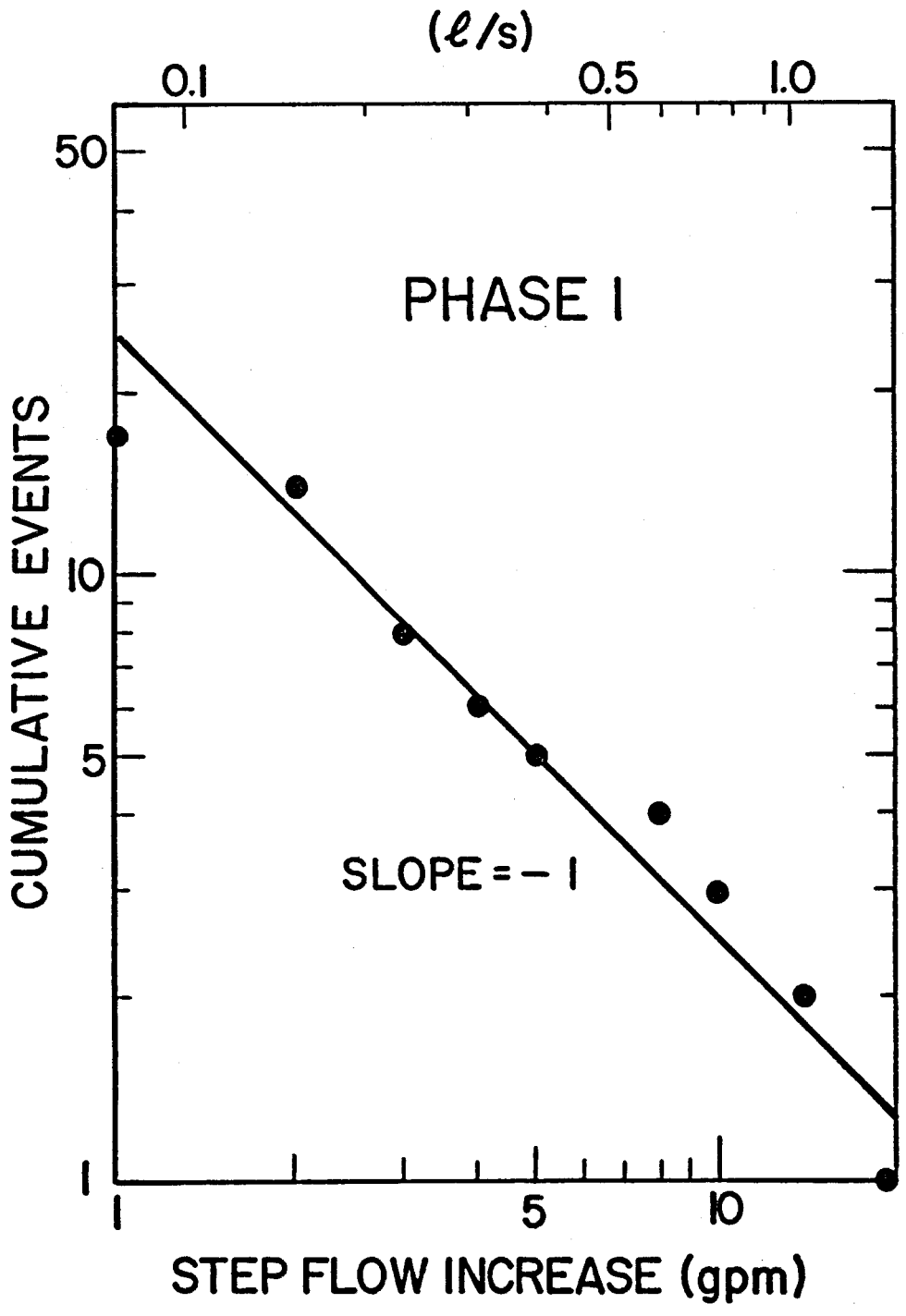

Fig. 4-9.
Correlation of the frequency of events to the size of the production flow increase in GT-2B.

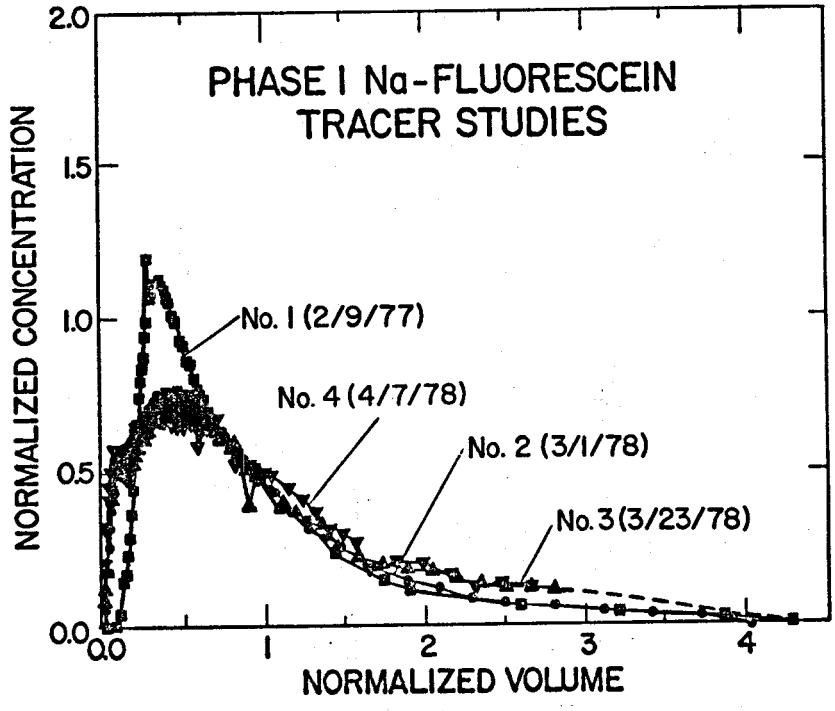

Fig. 4-10A.
Normalized tracer concentration as a function of normalized fracture system volume.

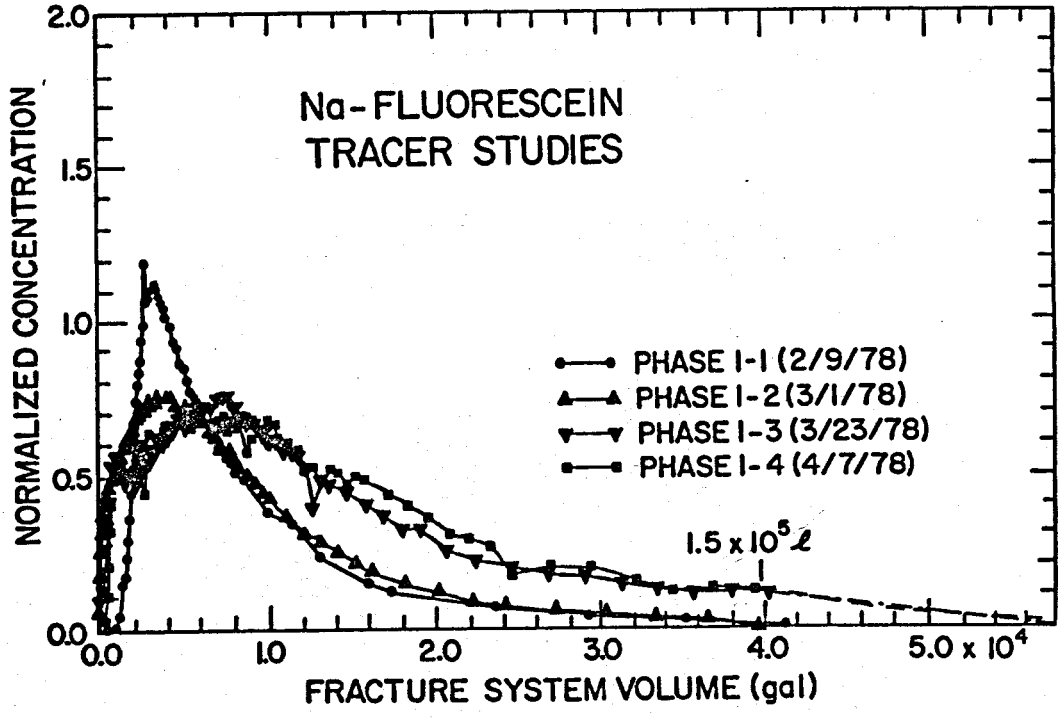

Fig. 4-10B
Normalized tracer concentration as a function of fracture system volume.

TABLE 4-I

RESIDENCE-TIME DISTRIBUTION RESULTS

EXPERIMENT	Q 10^6 gallons	$\bar{\dot{q}}$ gpm[b]	dye recovery (%)	<V> gal[c]	[V] gal	|V| at 90% gal	σ_θ^2	σ_θ^2 (90%)	Pe^{*-1}[d]
Phase 1-1 (2/9/78)	2.1	115	69	9089	6753	7728	0.65	0.44	0.591
Phase 1-2 (3/1/78)	6.9	208	65	9899	7644	8160	0.62	0.43	0.942
Phase 1-3 (3/23/78)	15.1	220	71[a]	14446	11904	12218	0.51	0.42	0.944
Phase 1-4 (4/7/78)	20.0	240	> 65[a]	14855	12786	12998	0.47	0.39	1.120

[a]Estimated from extrapolation of the RTD tail shown in Fig. 4-9; actual recovery to 40 000 gal was 63% for 1-3 and 57% for 1-4.

[b]1 gpm = 6.31×10^{-2} liters/s (ℓ/s).

[c]1 gal = 3.785 liters.

[d]$Pe^{*-1} = D/u\ell$ = inverse Peclet number.

$$[V] = \text{median volume} \int_0^{[V]} C_i dV \Big/ \left[\int_0^{\infty} C_i dV\right] = 0.5 \qquad (4\text{-}3)$$

$$|V| = \int_0^{V^*} VC_i dV \Big/ \left[\int_0^{V^*} C_i dV\right] = \text{trimmed mean volume.} \qquad (4\text{-}4)$$

$$\bar{\tau} = \langle V \rangle / \bar{\dot{q}} = \text{integral mean residence time, and} \qquad (4\text{-}5)$$

$$\sigma_\theta^2 = C_\theta \text{ distribution variance} = \int_0^{\infty} V^2 C_i dV \Big/ \left[\langle V \rangle^2 \int_0^{\infty} C_i dV\right] - 1 \ , \qquad (4\text{-}6)$$

where

C_i = measured output dye concentration
V = fracture system volume corresponding to C_i
$\bar{\dot{q}}$ = mean flow rate through the fracture system
V^* = truncation point in the trimmed distribution.

Flow in the fracture system can be described as well-mixed with no major short circuits. Dispersion of flow in a single hydraulic fracture does not account for all of the mixing. Because of this and the known existence of multiple flow paths between EE-1 and GT-2B, the observed shape of the RTD is caused by dispersion within individual flow paths as well as superposition from mixing of various production flows in the wellbore (see also Section 4.4 and 4.5). Consequently, several statistical quantities are needed to describe flow in the system. The median volume probably adequately represents the flow through the major production paths in GT-2B, while the increase in the spread of the distribution to larger volumes as evidenced by an increasing integral mean and variance are indicative of longer residence time paths possibly through more circuitous routes in the rock. The results of the RTD studies have been incorporated into a general flow model, which is discussed in detail in Section 4.5. However at this time, several general comments can be made; (1) The fracture flow system has grown considerably in size during the 75-day test, the integrated mean fracture system volume <V> increased to 56 400 ℓ (14 900 gal), up from 37 500 ℓ (9900 gal) on March 1, and the median volume became larger, 48 500 ℓ (12 800 gal) vs 28 800 ℓ (7600 gal). (2) Development of additional flow paths, was evident because of different arrivals of dye with smaller and larger residence times (or volumes), increasing the spread of the distribution. (3) The

apparent degree of mixing or dispersion (D) is virtually unchanged between the March 1 and April 7 experiments as shown by the similar shapes of the phase 1-2, 1-3, and 1-4 curves on the normalized coordinates of Fig. 4-9 and the similar inverse Peclet numbers ($Pe^{*-1} = D/u\ell$, u = velocity, ℓ = flow path length, and D = dispersion coefficient) resulting from homogeneous dispersed porous zone fits to the data of 0.942 (March 1, 1978), 0.944 (March 23, 1978) and 1.120 (April 7, 1978). (4) The increase in apparent Pe^{*-1} observed between the phase 1-1 and subsequent tests (1-2, 1-3, 1-4) cannot be explained by an increase in flow rate from 7.3 to ∿14.5 ℓ/s (115 to ∿230 gpm). Because we are operating in the freely turbulent region for porous media flow, one would expect a linear dependence of D on u and therefore a constant Pe*. Additional flow paths or a change in the character of flow in existing paths is a more likely cause of the change in apparent Pe* between the early and late tests.

4.3. Fluid Loss and Storage (H. Fisher)

The water loss, or the difference between the EE-1 injected flow and the GT-2B produced flow is determined by the fracture geometry, and an appropriate average permeability and pore (or reservoir) compressibility associated with all types of porosity accessible to the flow. The fracture area involved is not necessarily the same as the heat transfer area determined by the GT-2B temperature drawdown (see Section 3). There are other fractures intersecting the EE-1 wellbore. The fractures connected to the GT-2 and GT-2A wellbore could also contribute to the water storage and loss to permeation. Any fractures directly connected to the GT-2B wellbore did not contribute significantly to the loss, because they were maintained at close to hydrostatic pressure during Phase I. The observed permeability is an average over the large scale permeability opened by previous pressurizations, any welded joints, and the microporosity. Similarly the reservoir compressibility, or the ability of the reservoir to store water, includes the compressibility of the main fractures as well as the microporosity.

The data from past pressurization and flow experiments can be fit by a model in which the fluid pressure (P) in the reservoir is governed by a nonlinear diffusion equation (Refs. 2 and 7),

$$\nabla \cdot \left(\frac{k}{\mu} \nabla P\right) = \beta \frac{\partial P}{\partial t} \quad . \tag{4-7}$$

This equation can be derived from the conservation of fluid mass and the assumption of Darcy-type flow in all forms of porosity.

The permeability k and the compressibility β are functions of P, but the viscosity can be considered a constant. The k and β, which best fit past data, can be obtained from a porosity Φ with a pressure dependence given by

$$\Phi = \frac{\Phi_o}{(1-C_3P)^{0.6}} \quad . \tag{4-8}$$

The compressibility, $\beta = (\partial\Phi/\partial P)_T$ is, then

$$\beta = \frac{\beta_o}{(1-C_3P)^{1.6}} \quad . \tag{4-9}$$

Since the permeability is determined by the confining stress, and the two horizontal earth stresses are not necessarily equal, two components of permeability are used. Each is related to some portion of the porosity by the Karmen-Kozeny relation for small porosity $k_i \propto \Phi_i^3$. Then k_3, perpendicular to the minimum earth stress S_3, is

$$k_3 = \frac{k_o}{(1-C_3P)^{1.8}} \tag{4-10}$$

and k_2, perpendicular to the intermediate horizontal earth stress S_2, is

$$k_2 = \frac{k_o}{(1-C_2P)^{1.8}} \quad . \tag{4-11}$$

The exponents in Eqs. (4-9), (4-10), and (4-11) have been determined from previous experiments, as have C_2 and C_3. The best results are obtained for $C_3 \simeq 5.0\ C_2$. With C_2 and C_3 constant, Eqs. (4-9), (4-10), and (4-11) are an approximation that holds only for $P < C_3^{-1}$. True singularities in Eqs. (4-9), (4-10), and (4-11) do not exist because $P \to S_3$, C_3, and C_2 become functions of P. This pressure dependence of C_2 and C_3 occurs when P contributes significantly to the local value of the total stress, and complete solutions can be obtained only if Eq (4-7) is coupled with the stress-strain relations. During much of

the 75-day test the pressure was near the minimum estimates of S_3 and some adjustment of C_3 is necessary to obtain good fits to the data.

As in past experiments, the pressure and flow were calculated for a disk-shaped fracture with the diffusion code AYER.[8] Because multidimensional permeation flow was anticipated for long pumping times, two-dimensional axially symmetric problems were used. However, only one-dimensional flow was observed for the entire 75-day pumping period. The one-dimensional portion of the flow can be characterized by the magnitude of the diffusion parameter $\alpha = A\sqrt{k\beta}$ at hydrostatic pressure. If multidimensional flow develops, then the time constant $\tau = A\mu\beta/k$ is needed. Here A is the effective diffusion area of the fracture.

Fluid loss data were examined in two stages. Figure 4-11 shows the loss rate $\dot{q}$ and the EE-1 surface pressure P for the first 10 days of the test. For analysis purposes, either can be used as input, and the other results from the calculation. For the first 5 days, the input was taken to be a linear approximation of the fluid loss rate shown in Fig. 4-11. The calculated downhole pressures were then converted to equivalent surface pressures by subtracting the hydrostatic change of pressure in the wellbore corrected for temperature changes. The fit shown is for an $A\sqrt{k_0\beta_0} = 8.1 \times 10^5 m^3 MPa^{-1/2}$ (or 160 cm^3 when normalized to $\beta_0 = 2.7 \times 10^{-5} MPa^{-1}$) at hydrostatic pressure and at $C_3^{-1} \approx 8.9$ MPa. (1 MPa = 10 bar.) Most of the discrepancy at early times (0.5 days) is probably due to the initial spike in loss rate q that was not included in the input.

For the calculation of longer term water losses (times > 5 days), the EE-1 downhole pressure was used as input to AYER. The surface pressure was approximated by the straight line segments as in Fig. 4-12, and converted to a downhole pressure by adding the temperature-corrected hydrostatic pressure in the wellbore. Figure 4-13 shows the fluid loss data as recorded on the makeup pump venturi. The dashed line is the result of the AYER calculation for the model described earlier. The data of Fig. 4-14 show totalized makeup flow as recorded on the makeup-pump Crane meter. These data have been corrected for a large vent (5300 m^3 or 140 000 gal) on the 23rd day. Both the loss rate data of Fig. 4-13 and the integral data of Fig. 4-14 have been corrected for the EE-1 annulus leak occurring after the 35th day. The solid curve of Fig. 4-14 is the result of the same AYER calculation as was used to match the loss rate. Because of the pressure transient at the start of pumping, the calculated lines in Figs. 4-13 and 4-14, which are a response to a step function input, begin on the third

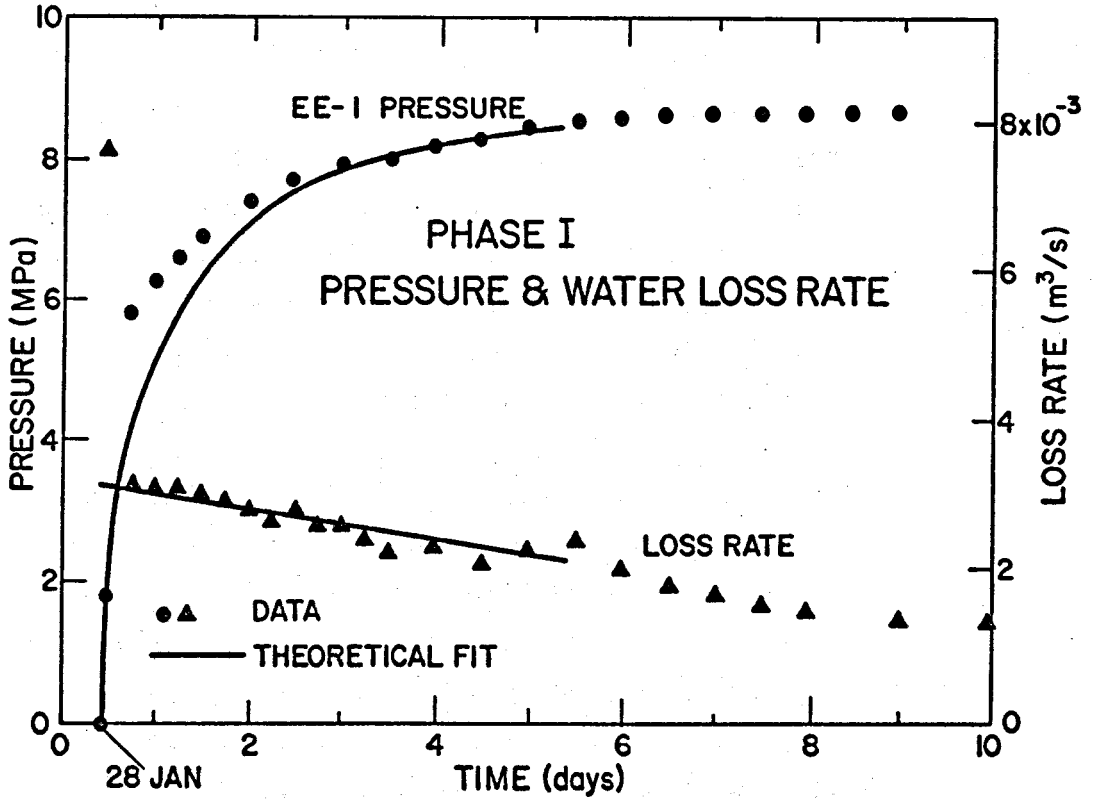

Fig. 4-11.
Early histories of surface injection pressure and water loss rate.

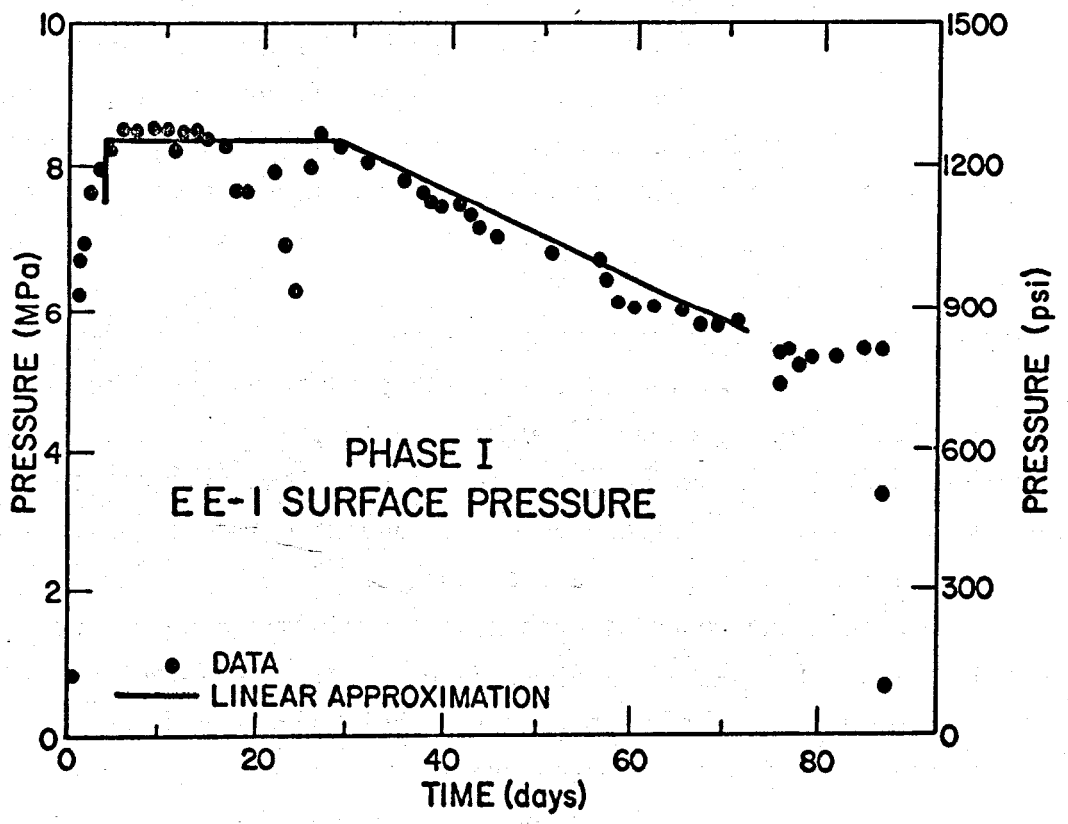

Fig. 4-12.
EE-1 surface injection pressure and modeling approximations used.

day. The parameters in the long-term calculations are $A\sqrt{k_o\beta_o} = 7.0 \times 10^{-7} m^3 MPa^{-1/2}$ (or 137 cm^3 when normalized to $\beta_o = 2.7 \times 10^{-5} MPa^{-1}$) at hydrostatic pressure and $C_3^{-1} = 9.3$ MPa. The time constant $\tau = A\mu\beta/k$ in the calculations was increased to such large values that changes in it did not significantly effect the results. Because of the sensitivity of the fits to the exact pressure dependence of k and β it is difficult to attach significance to the difference in the values of $A\sqrt{k_o\beta_o}$ as used in the short- and long-term analysis. We concluded that only a one-dimensional flow was observed in the 75-day experiment.

4.4. Injection and Production Zones (R. M. Potter, H. D. Murphy, and S. Faas)

The temperature history in the open hole region of GT-2B obtained during the Phase I operation has shown both numerous production zones and changes in the relative temperatures of the produced fluid (see Figs. 4-5 and 4-6). Unfortunately, because of the complexity of the flow, the specific flow rate in each production zone cannot be determined from the temperature alone. A velocity-measuring tool (spinner) was purchased from the Worth-Well Company in order to measure relative flow at various depths in GT-2B. Its initial test deployment was carried out on April 12, 1978 just one day before shut-in. Because of the importance that any estimate of the relative values of production flows would provide, a temporary system of recording the data was devised.

Three runs were made over the region of interest using a constant downward logging velocity of $\sim$ 0.8 m/min (29 ft/min). Inspection of the output voltage signal from the spinner circuit plotted against depth showed several distinct step changes. Actual flow increases could be calculated from the relative values of velocity and the measured GT-2B production flow. Table 4-II shows the position and magnitude of these detectable flow points.

The rather large level of fluctuation in the production zone did not allow detection much below a flow fraction of $\sim$0.05. Inspection of a typical temperature log in GT-2B during this period (Fig. 4-15) shows that in addition to the steps detected by the spinner, there are several additional temperature steps that are not correlated with observable flow changes.

Because flow enters the reservoir behind the casing in a poorly cemented 180-m (600-ft) section of EE-1 from 2740 to 2930 m, relative injection flows in this well cannot be measured with a spinner tool but have been deduced from radioiodine injection and flowing temperature logs.

Figure 4-16 is the June 2, 1978 temperature survey of EE-1. The dashed upper lines represent the radial conduction-dominated recovery of the wellbore

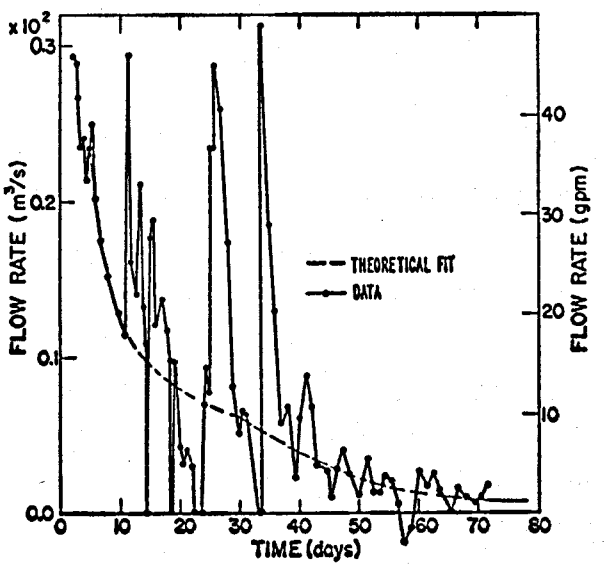

Fig. 4-13.
Makeup water loss rate as recorded on the makeup venturi flow meter.

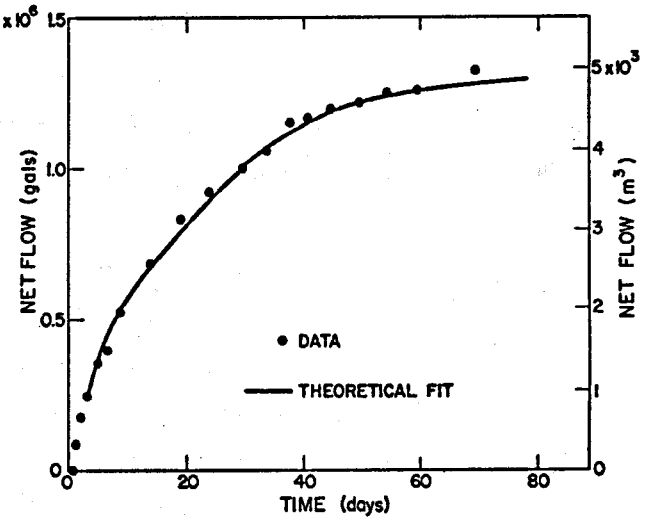

Fig. 4-14.
Total accumulated water loss in storage as recorded on the makeup Crane meter.

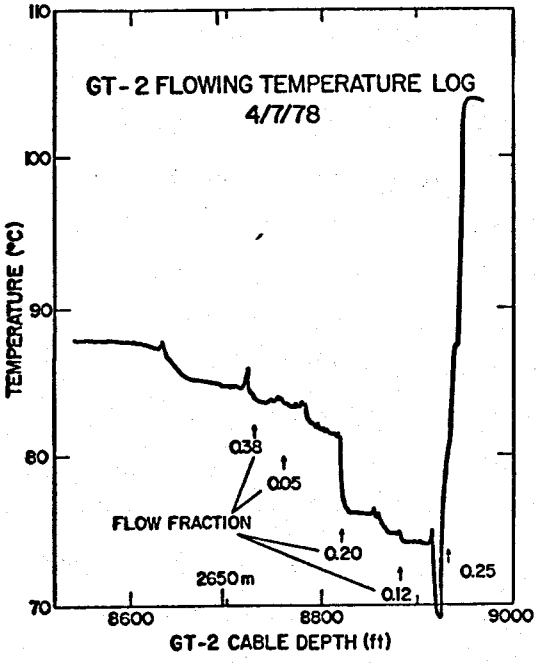

Fig. 4-15.
GT-2B flowing temperature log taken on April 7, 1978.

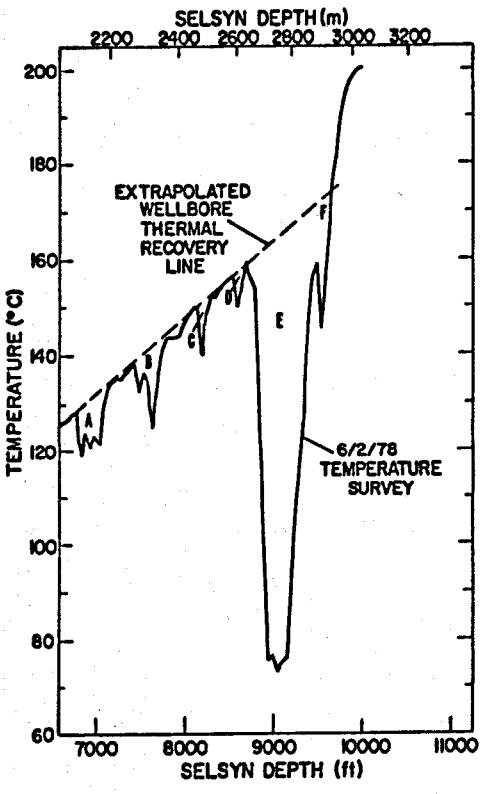

Fig. 4-16.
Shut-in temperature log taken in EE-1 on June 2, 1978.

temperature following shut-in. Departures from this line are caused by water infiltration into the formation. The principal temperature depression anomalies are labeled A through F. Subject to certain assumptions, it is possible to estimate the relative water flows into each zone corresponding to a temperature depression simply by measuring the area of each depression and normalizing by the total area of all the depressions. This was done with a planimeter, and the results are given in Table 4-III.

About 81% of the flow goes into Anomaly E, which is centered about 2760 m (9050 ft). Only 5% enters Anomaly F at $\sim$ 2930 m. It is this latter connection, which may provide a relatively high-temperature source of dissolved silica as discussed in Section 5.1. At the end of the 75-day test the net system impedance for the combined flow paths between EE-1 and GT-2B was 3 psi/gpm. Since only 1/20 of the total flow appears to be via the 2930-m path, the impedance between the 2930-m injection zone in EE-1 and GT-2B must have been about 60 psi/gpm.

4.5. Flow Models (R. M. Potter and J. W. Tester)

A two-fracture flow model based on the following assumptions has been developed. First, there is a high conductance flow path (fracture) that supplies all measurable flow increases as indicated by the spinner survey. The temperature of the fluid in this fracture with depth will be calculated. This fracture lies between GT-2B and EE-1. Secondly, there is another fracture or secondary flow path that has several small connecting fractures of high impedance that allow relatively isothermal flows into the GT-2B borehole along its length. Assuming a value for the fluid temperature, we can calculate the magnitude of these flows. This secondary flow path lies in the region beyond GT-2B opposite EE-1.

The previous analysis of the spinner survey has indicated five distinct and measurable flow changes, which are coincident with temperature steps. In addition, a measured flow near the bottom of the GT-2B borehole requires at least two flows, each with temperatures significantly different. The temperature log taken on April 7 (Fig. 4-15) shows at least four temperature steps that have no measurable (via spinner survey) accompanying flow changes. This behavior suggests two sources for the flows, one that provides relatively high flow at moderate temperature and another with flows below the limit of resolution but whose temperatures are great enough to produce measurable temperature changes.

TABLE 4-II

POSITION AND MAGNITUDE OF GT-2B EXIT FLOWS

GT-2B LASL Cable Depth (m)	GT-2B LASL Cable Depth (ft)	Voltage Change (mv)	Flow Fraction	Absolute Flow (gpm)	ℓ/min
2660-2661	8726-8729	6.0	.38	92	348
2671-2672	8764-8765	0.8	.05	12	45
2686-2688	8812-8820	3.2	.20	48	182
2705-2706	8876-8879	1.8	.12	29	110
2719	8920	3.9	.25	61	231
	Total	15.7	1.00	242	916

TABLE 4-III

POSITION AND MAGNITUDE OF RELATIVE EE-1 INJECTION FLOWS

Anomaly	Cable Depth Interval (m)	Cable Depth Interval (ft)	Flow Fraction
A	2073-2179	6800-7150	0.05
B	2271-2377	7450-7800	0.06
C	2484-2530	8150-8300	0.01
D	2606-2652	8550-8700	0.01
E	2652-2896	8700-9500	0.81
F	2896-2957	9500-9700	0.05
		Total	1.00

Figure 4-17 provides an explanation for these observations, which use the measured flows and the observed GT-2B wellbore temperature profile (Fig. 4-15) along with an assumed 180°C temperature in the secondary fracture flow path. All the calculated flows from this secondary zone are less than the resolution of the spinner survey. In addition, the derived temperature gradient profile shown in Fig. 4-18 appears to be consistent with the drawdown of a 100-m-diam fracture.

This temperature choice comes from the pre-test unperturbed rock temperature in this region and from geochemical data that indicate a steady flow with a quartz saturation temperature of ∿180-190°C (see Section 5.1). Figure 4-19 shows a temperature log of GT-2B after shut-in. The maximum temperature at a depth of 2640 m (∿ 8660 ft) coincides with the point of maximum flow from the assumed second fracture or flow path.

Table 4-IV gives the measured average flows and pressures in the two boreholes during this experiment along with calculated values of impedance for the various flow connections. It is assumed that there is no significant pressure drop in the entire EE-1 system except at the GT-2B connecting fractures. Also shown are the initial values of impedance on January 30, 1978 before the start of the major flow test. This table shows the original main fracture in GT-2B (at 2686-2688 m) that carried a smaller fraction of the total flow with a significantly smaller impedance.

The location of this secondary flow path or fracture system that provides hot fluid entering GT-2B is uncertain. Figure 4-20 presents a hypothetical case in plan view showing two wellbores (GT-2B and EE-1) connected by main and secondary vertical fractures, which leave the EE-1 wellbore at 2758 and 2940 m (9050 and 9650 ft) respectively. Both fractures are oriented in a northwest-southwest direction. A number of early fracturing experiments in EE-1 activated the fracture zone at 2940 m, while degradation of the casing cement between 2940 m eventually led to the activation of a lower impedance flow path leaving EE-1 at 2758 m. If the proposed fracture at 2940 m extended vertically for 305 m (∿ 1000 ft), it would come very close to the uncased GT-2B wellbore. Furthermore, if this fracture is connected to GT-2B at 2690 m (8660 ft) via a high angle conductive joint, it would serve as the source of "hot water" as shown in Fig. 4-19.

The flow model described above can also be used to explain the residence time distribution and geochemistry results described in Sections 4.2 and 5.1

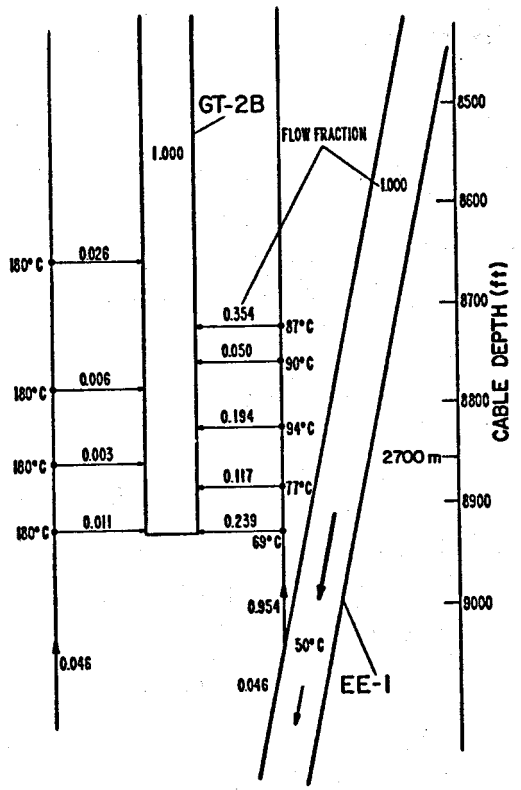

Fig. 4-17.
Conceptual flow model for the GT-2B/EE-1 system.

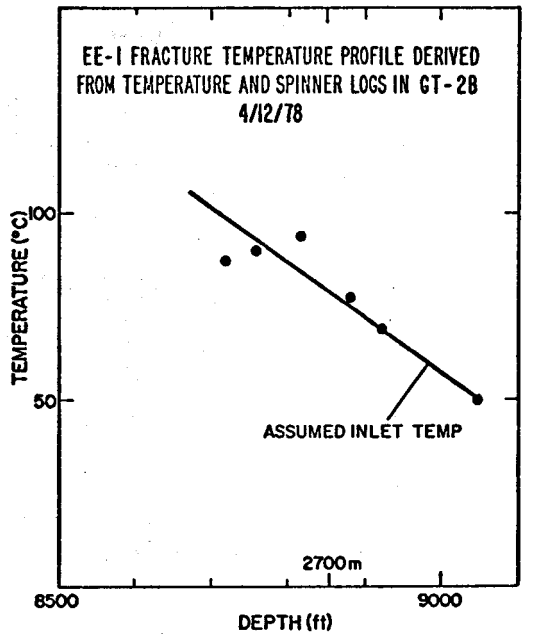

Fig. 4-18.
Derived temperature gradient profile for GT-2B.

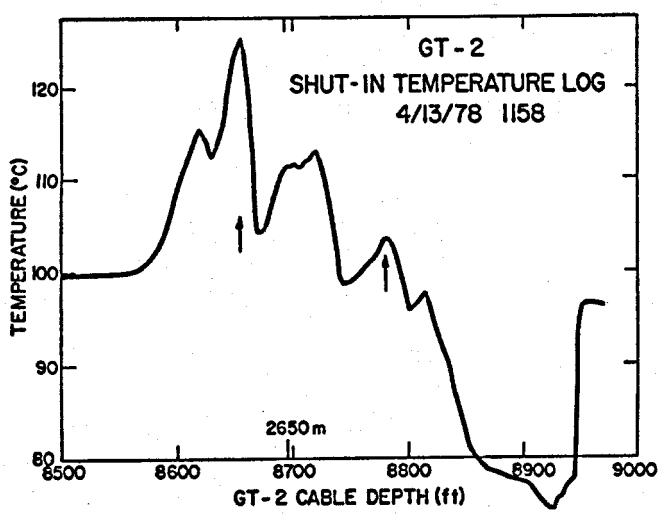

Fig. 4-19.
GT-2B shut-in temperature log taken on April 13, 1978

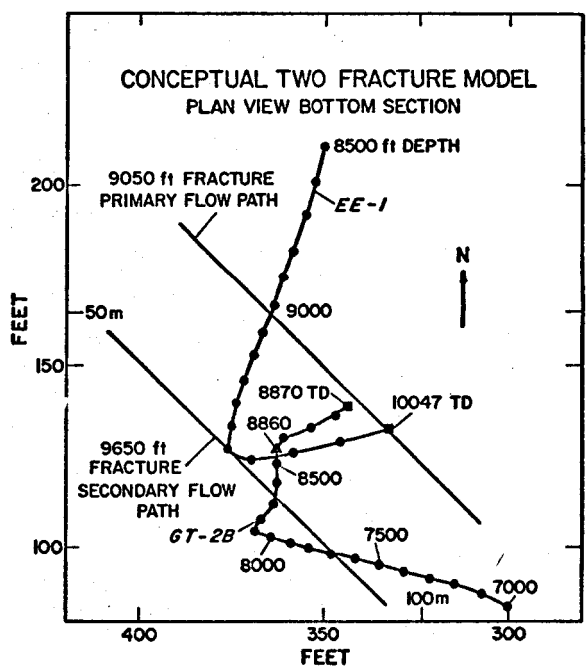

Fig. 4-20.
Conceptual model of primary and secondary flow paths in the GT-2B/EE-1 system.

TABLE 4-IV

VARIOUS IMPEDANCES IN EE-1/GT-2B SYSTEM

(m)	Fracture Depth (ft) in GT-2B	Flow Impedance bar-s/ℓ (psi/gpm) Jan. 30, 1978 Main	Jan. 30, 1978 Secondary	April 12, 1978 Main	April 12, 1978 Secondary
2640	8660				126 (115)
2660	8728			8.2 (7.5)	
2670	8760			66 (60)	
2677	8784				541 (495)
2688	8820	22 (20)		16.7 (15.3)	
2703	8867				1082 (990)
2707	8882			27.8 (25.4)	
2719	8920				295 (270)
2720	8925	87 (80)		13.6 (12.4)	
	Fracture set	17 (16)		3.4 (3.12)	71 (65)
	Entire system	17 (16)		3.26 (2.98)	

On April 12, 1978 EE-1 pressure = 55.9 bar (810 psi)
GT-2 pressure = 14.5 bar (210 psi)
Buoyancy = 8.3 bar (120 psi)
System pressure drop = 49.7 bar (720 psi)
GT-2 flow = 15.9 ℓ/s

respectively. Figure 4-21 presents a simplified version of the flow model with primary and secondary flow paths. The primary path flows each have a small degree of dispersion but widely different residence times in the main fracture between a fixed injection point in EE-1 and the production zone in GT-2B. These flows are mixed to produce an apparent high level of dispersion. Also, a secondary "matrix-like" flow is present, empirically characterized by a volume plug flow in series with a well-mixed volume. Thus the overall RTD observed during the later period of the 75-day test is a combination of all flow paths as shown in Fig. 4-22.

The discussion has illustrated the complex relationships that exist between the geometric, thermal, and chemical properties of the fracture system. A unique model consistent with all the data does not exist, at least with the information we now have on the properties of the reservoir. In fact, we have selected simple models and tested their consistency rather than try to improve our fit to the data by adding unnecessary complexity.

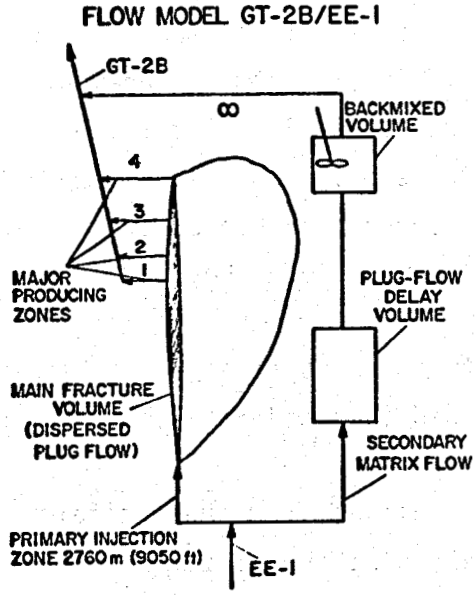

Fig. 4-21.
Simplified schematic depicting dispersed plug flow in the main fracture and "matrix-like" flow in secondary fracture system.

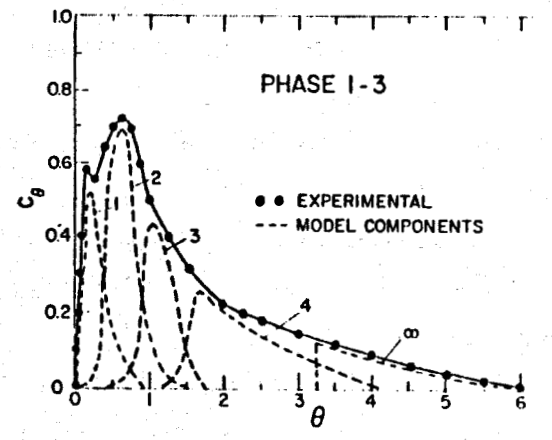

Fig. 4-22.
Normalized residence time distribution (RTD) with individual flow zone contributions shown from the model of Fig. 4-21.

5. FLUID GEOCHEMISTRY

5.1. Major Element Analysis (C. O. Grigsby, J. Abbott, L. Blatz, C. Holley, and J. W. Tester)

During the 75-day period, a gradual rise in the concentration of dissolved species approached steady state levels corresponding to the concentrations observed for water which remains in contact with the reservoir for an extended period. The effects of mixing among various flow paths and mass transfer strongly influenced the observed concentration change of dissolved species with time.

Procedures

Liquid samples were collected during Phase I Segment 2 at four points: Samples designated "G" were collected at the GT-2 producing wellhead by cooling the fluid through a 15-m 1.27-cm (50-foot 1/2-in.) O.D. copper tube, which was immersed in a 0.2-m^3 (55-gal) drum of cold water. The sampling tube was open to atmospheric pressure at all times, and the pressure drop from GT-2 wellhead pressure to atmospheric pressure was taken across a ball valve. Samples were collected in 1-ℓ nalgene LPE bottles, which were rinsed 2 or 3 times with geothermal fluid just prior to actual sample collection. Before each bottle was rinsed, the sampling tube was flushed with 3.8 ℓ (∿ 1 gal) of water to remove the stagnant water from the previous sampling. For the first month of operation, the valve was left open at a flow rate of 3.8 ℓ/min (∿ 1 gpm) to prevent freezing in the tube. This continual flow caused the deposition of calcite on the inside of the tube, which eventually plugged the sample tube. The sample tube was replaced, and the new tube did not develop any observable calcite scale as the danger of freezing had passed, and the valve was closed between sample collections.

Samples designated "E" were collected between pumps #1 and #2. As described in Section 2 these samples represent the fluid injected into the geothermal system at EE-1.

Makeup water samples, labeled "M", were collected from the manifold at the exit of the 100-micron filters. The makeup water was supplied from a 122-m (400-ft) well on site to a 1.5 x 10^6 ℓ (400 000-gal) holding pond near EE-1 where the water was stored and where in emergency situations water from the circulating system was discharged. (See Fig. 2-3.) The pond was at all times open to the atmosphere and exposed to rain, snow and runoff.

About halfway through the 75-day run, the EE-1 annulus began to leak and samples of the fluid were collected for analysis. These samples are labeled "A".

The following analytical techniques were used in the determination of chemical composition of the fluids: standard pH electrode and meter; HCO_3^-, titration with 0.02N H_2SO_4 to a pH of 4.5 endpoint using a pH meter; conductivity with a Hach conductivity probe and meter; F^-, Orion solid state selective electrode with Beckman millivolt meter; SiO_2, ammonium molybdate spectrophotometric technique; Cl^-, argentometric titration; $SO_4^=$, spectrophotometer measurement after precipitation with $BaCl_2$; and Ca, Na, K, Si, Li by atomic absorption with a Perkin-Elmer Model 460AA.

Results

The concentration-time history of various dissolved species collected from the production (GT-2) and injection (EE-1) wellheads is presented in Figs. 5-2 through 5-11. In addition, plots of total dissolved solids and solution conductivity are also presented (Figs. 5-12 and 5-13). There are several features common to all of the graphs. First, the initial samples had high concentrations of each of the species measured. During the early pumping period when makeup rates were high these high concentrations dropped very rapidly due to dilution and mixing with the relatively pure makeup water (see Figs. 5-1, 5-5, 5-8, 5-9, 5-11, 5-12, and 5-13). These initial samples reflect the nature of the water, which had been contained in the reservoir for approximately 3 months. After an initial flushing of the 230 000-ℓ ($\sim$60 000-gal) system in which the water produced at GT-2 was discharged, the system was operated as a closed loop with the makeup water flow supplying water lost to permeability storage in the reservoir. As makeup flow rates dropped, the dilution effect was lessened, and the concentrations of dissolved material began to rise to steady state values.

There were several emergencies that forced the shutdown of the system for various lengths of time. The most noticeable of these was the sudden change in downhole impedance on day 21-1/2. At that time, the GT-2 pressure rose rapidly causing an unacceptably high inlet pump pressure. Consequently a fraction of the produced fluid was vented to the EE-1 storage pond to control the pressure. However the high flow rate through the heat exchangers resulted in an outlet temperature that was too high to operate the pumps. The pumps were shut down, and all of the GT-2 flow was vented to the EE-1 storage pond. Because of the pressure decline in the fracture system, water stored in the permeable rock returned to the wellbore and then to the surface carrying more dissolved material

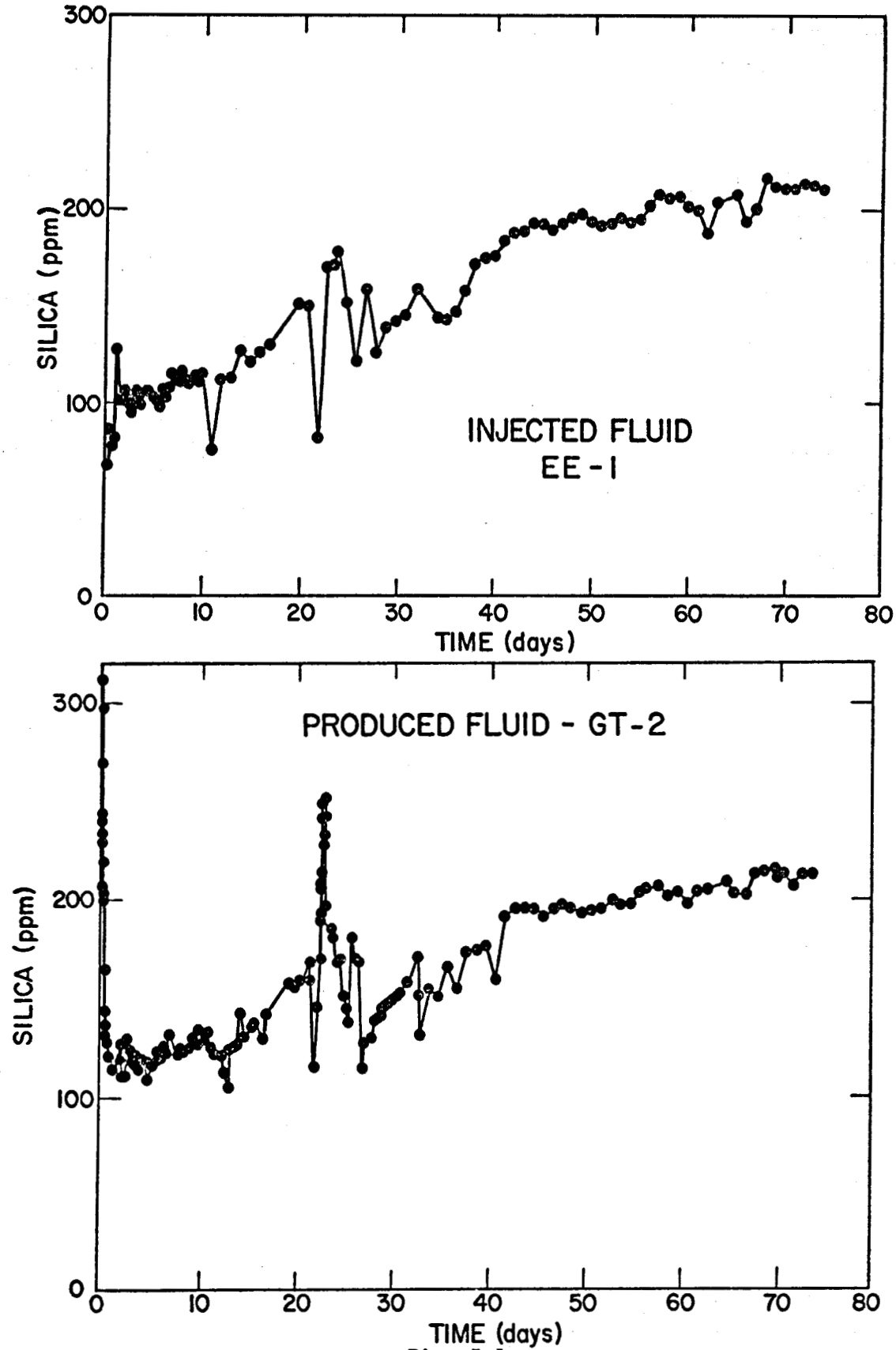

Fig. 5-1.
Dissolved silica in the injected and produced fluids.

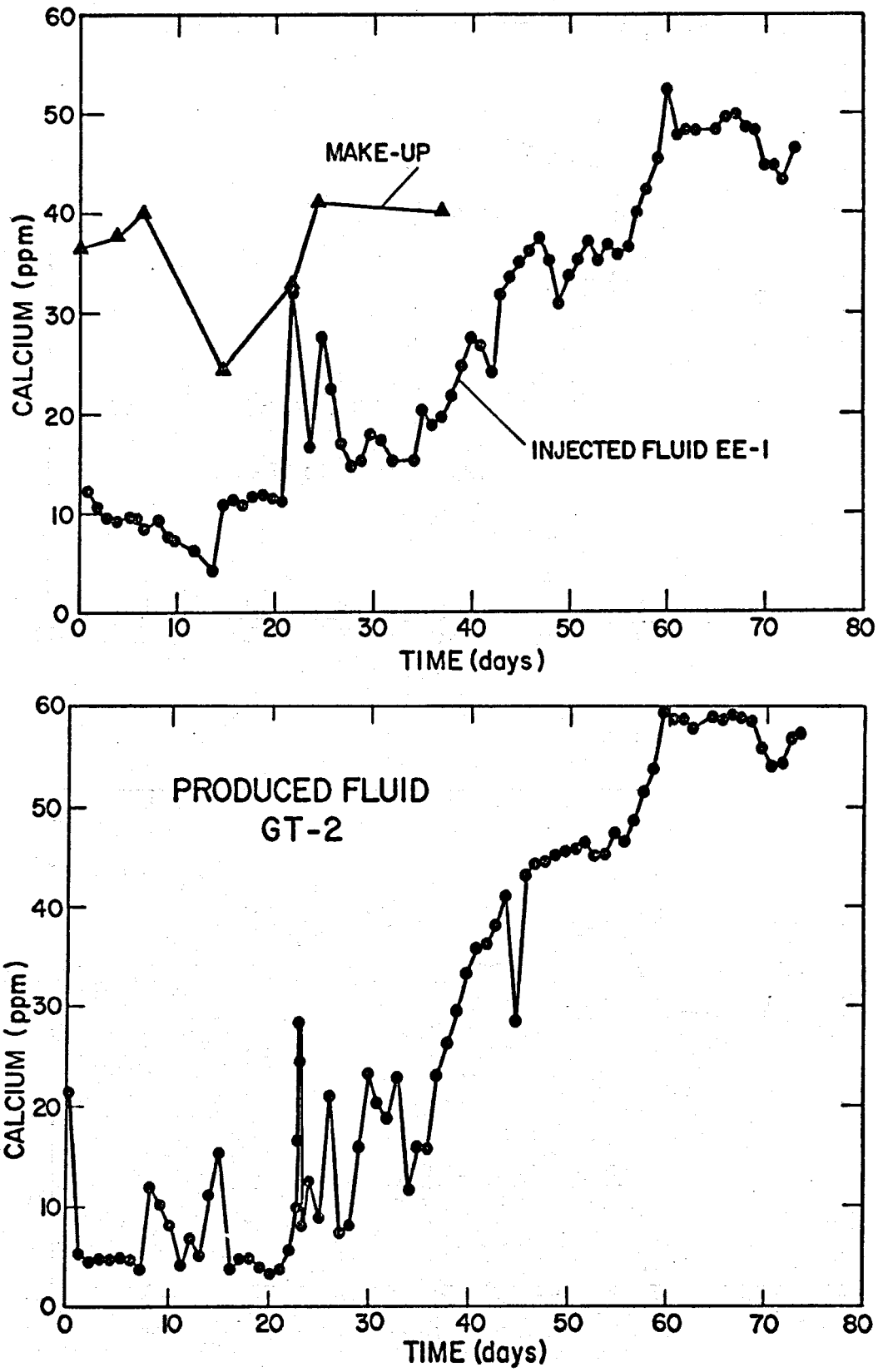

Fig. 5-2.
Calcium concentration in the injected, produced, and make-up fluids.

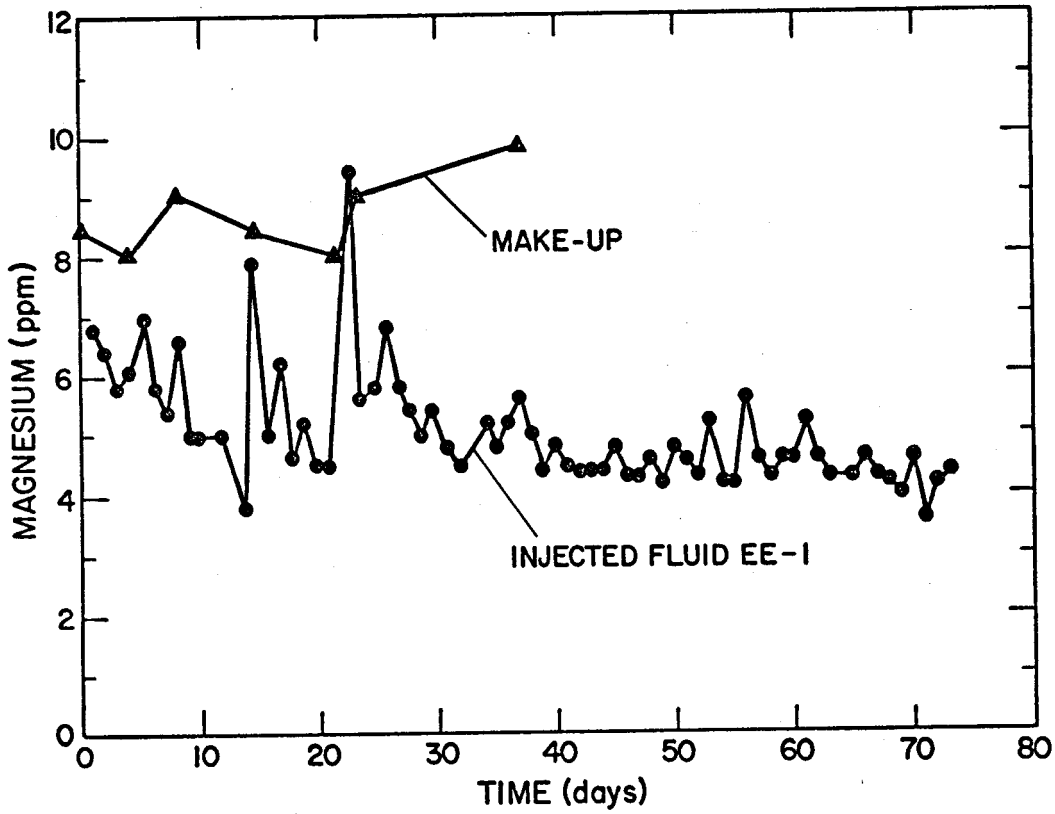

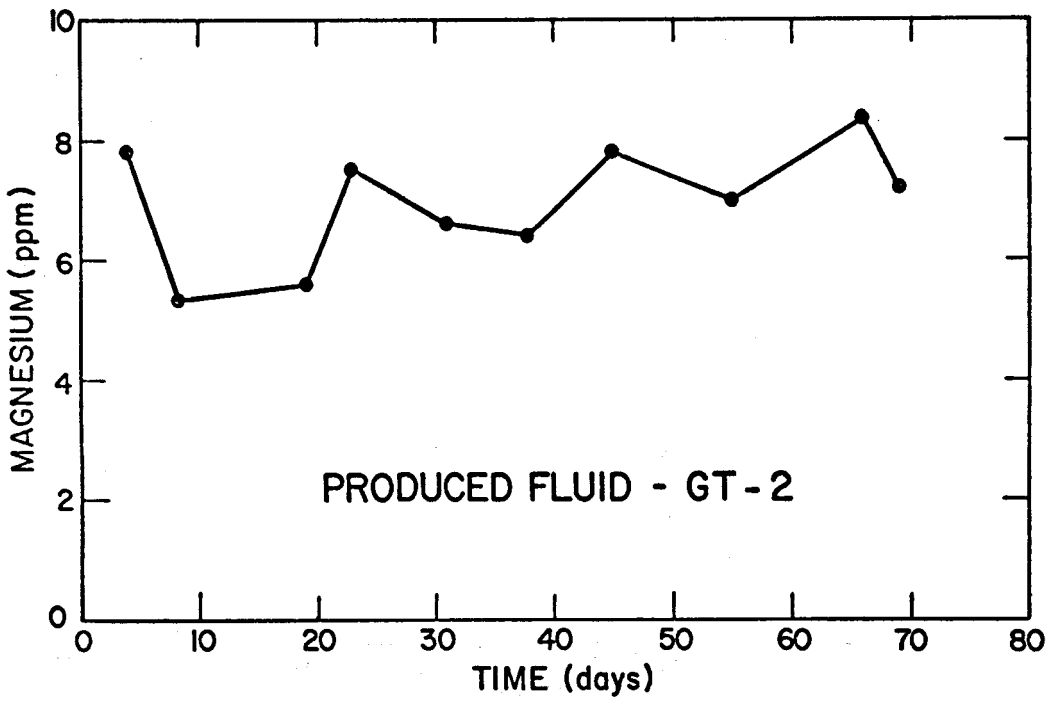

Fig. 5-3.
Magnesium concentrations in the injected, produced, and make-up fluids.

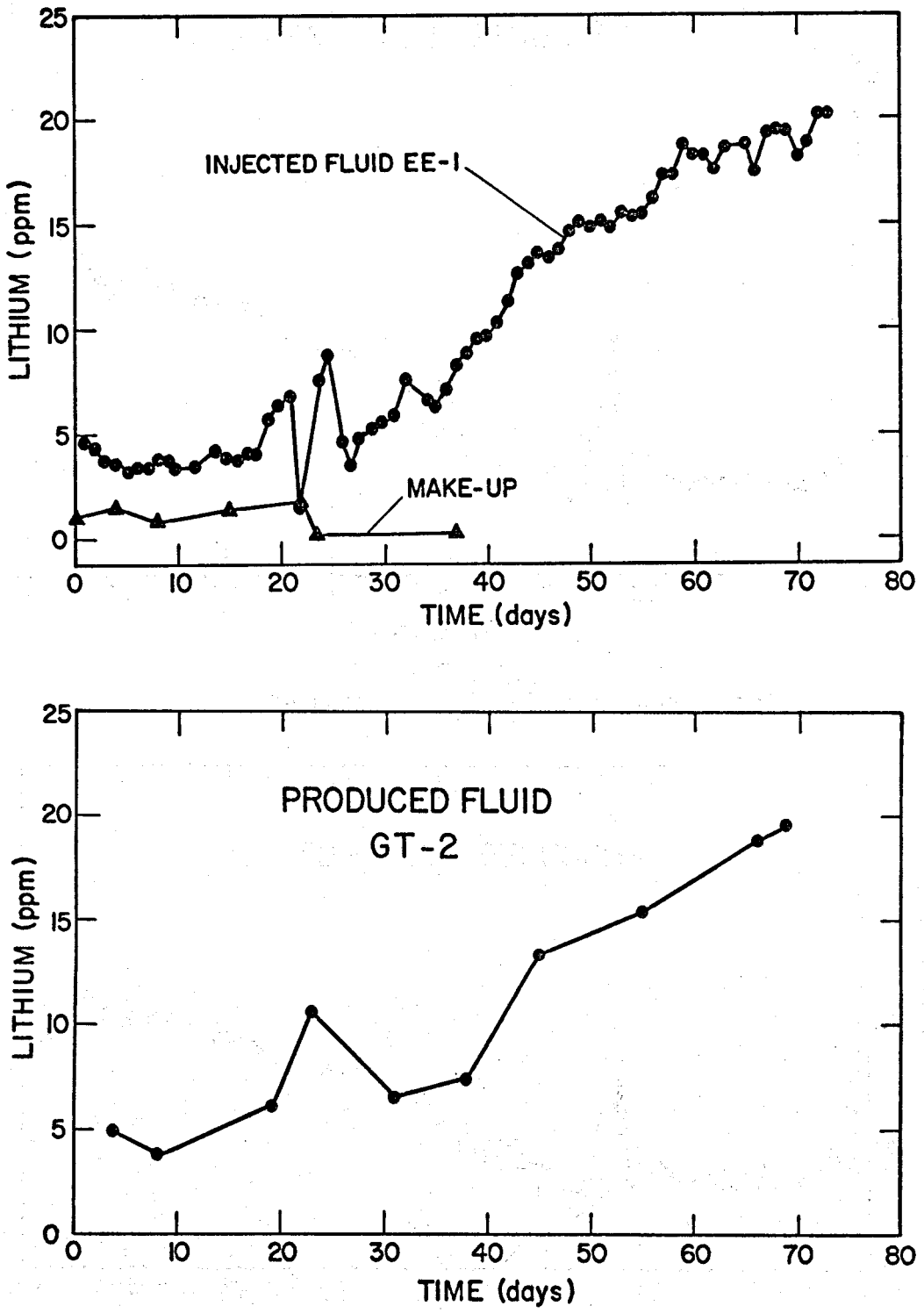

Fig. 5-4.
Lithium concentrations in the injected, produced, and make-up fluids.

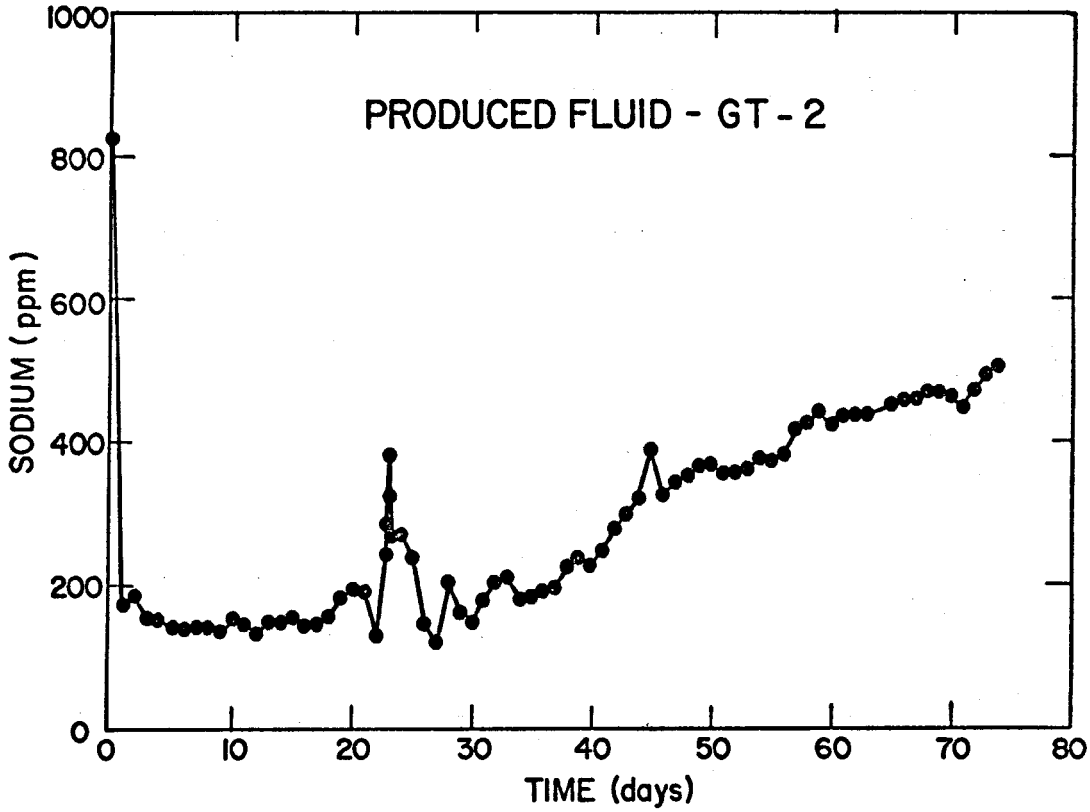

Fig. 5-5.
Sodium concentration in the produced fluid.

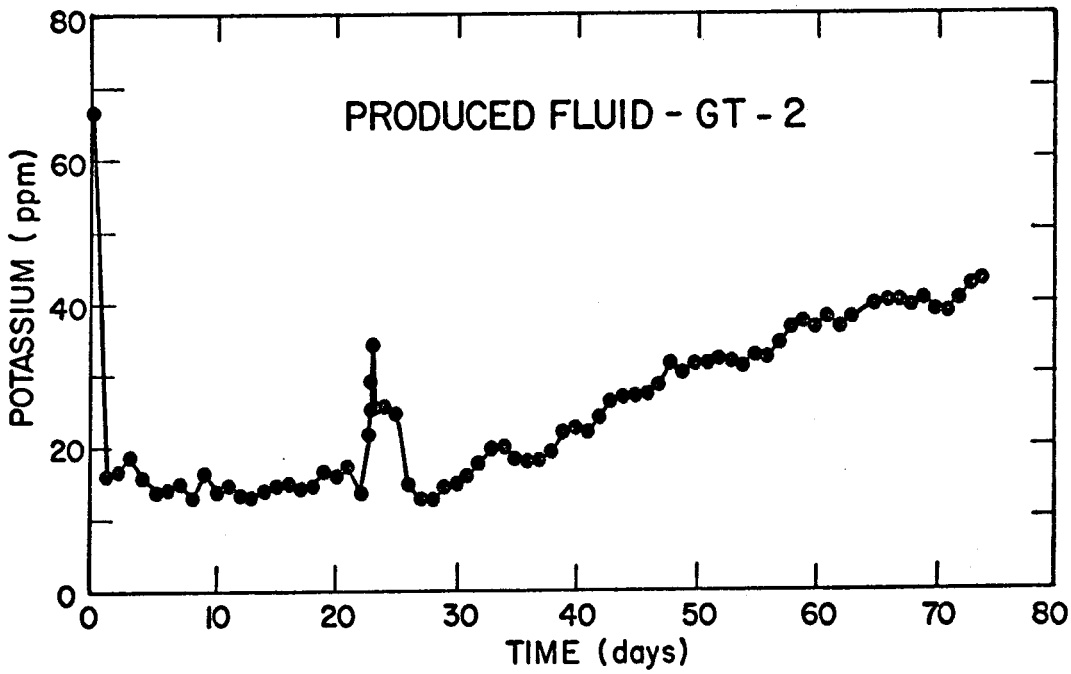

Fig. 5-6.
Potassium concentration in the produced fluid.

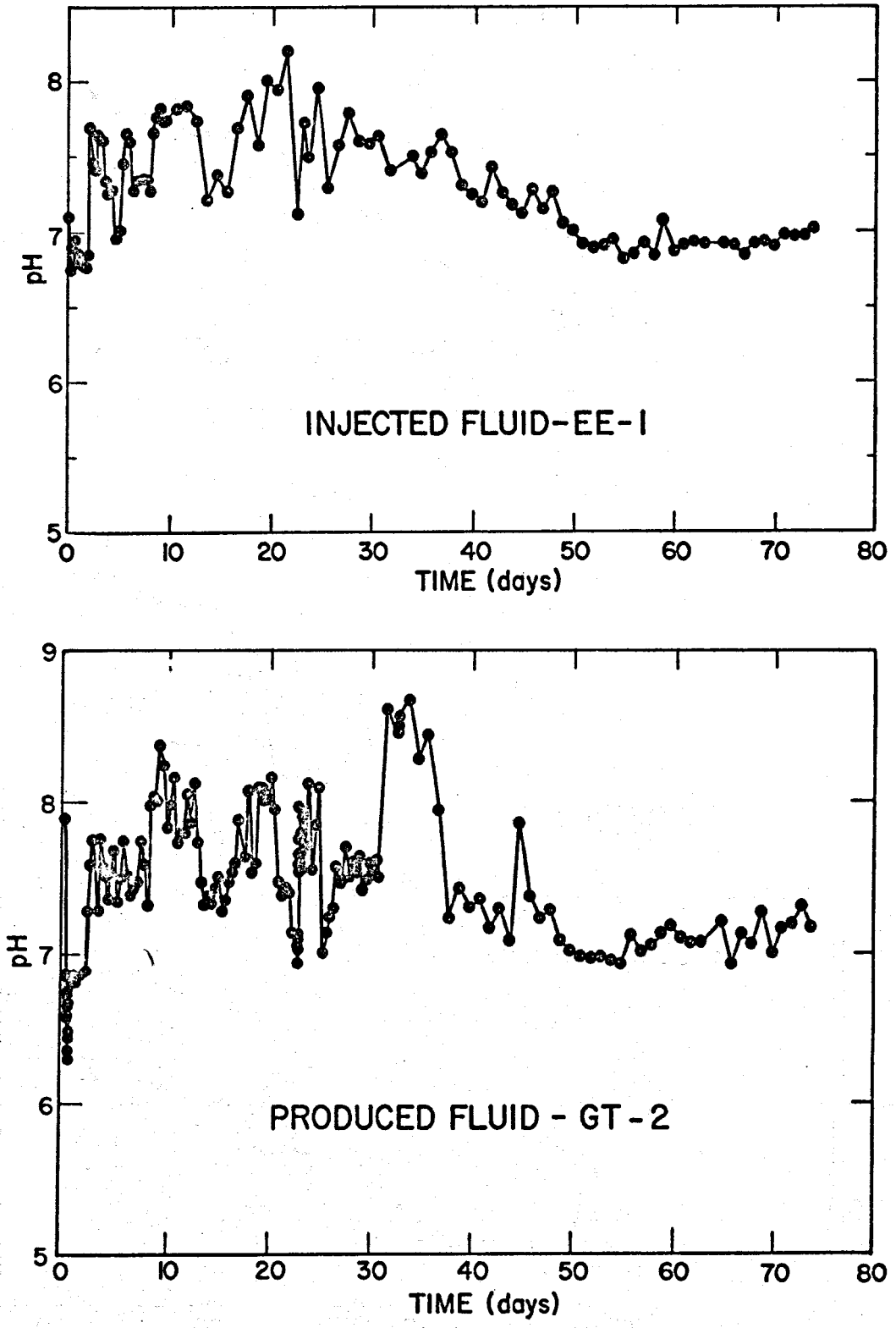

Fig. 5-7.
Hydrogen ion concentrations expressed as pH in the injected and produced fluids.

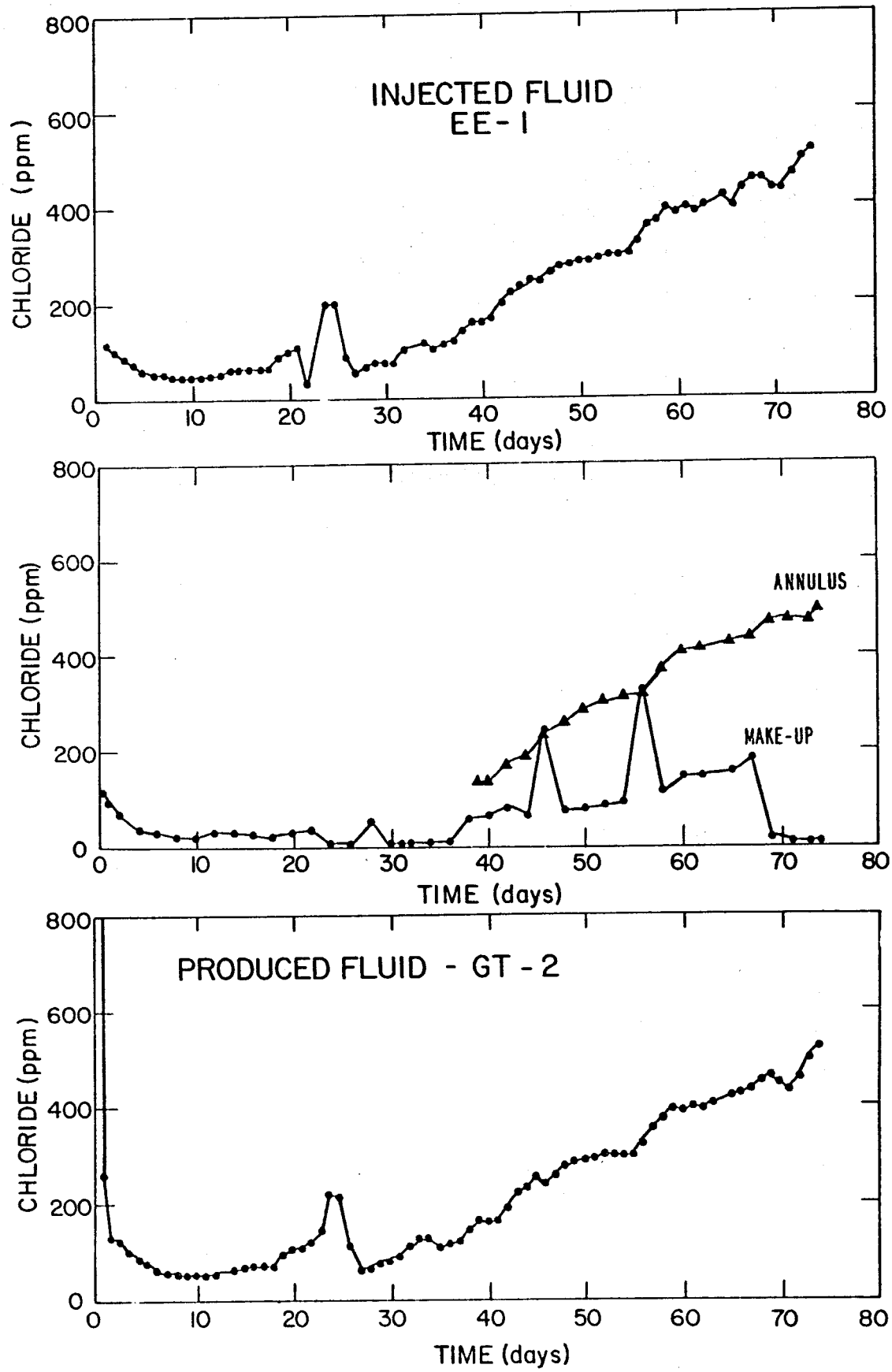

Fig. 5-8.
Chloride concentrations in the injected, produced, make-up, and EE-1 annulus fluids.

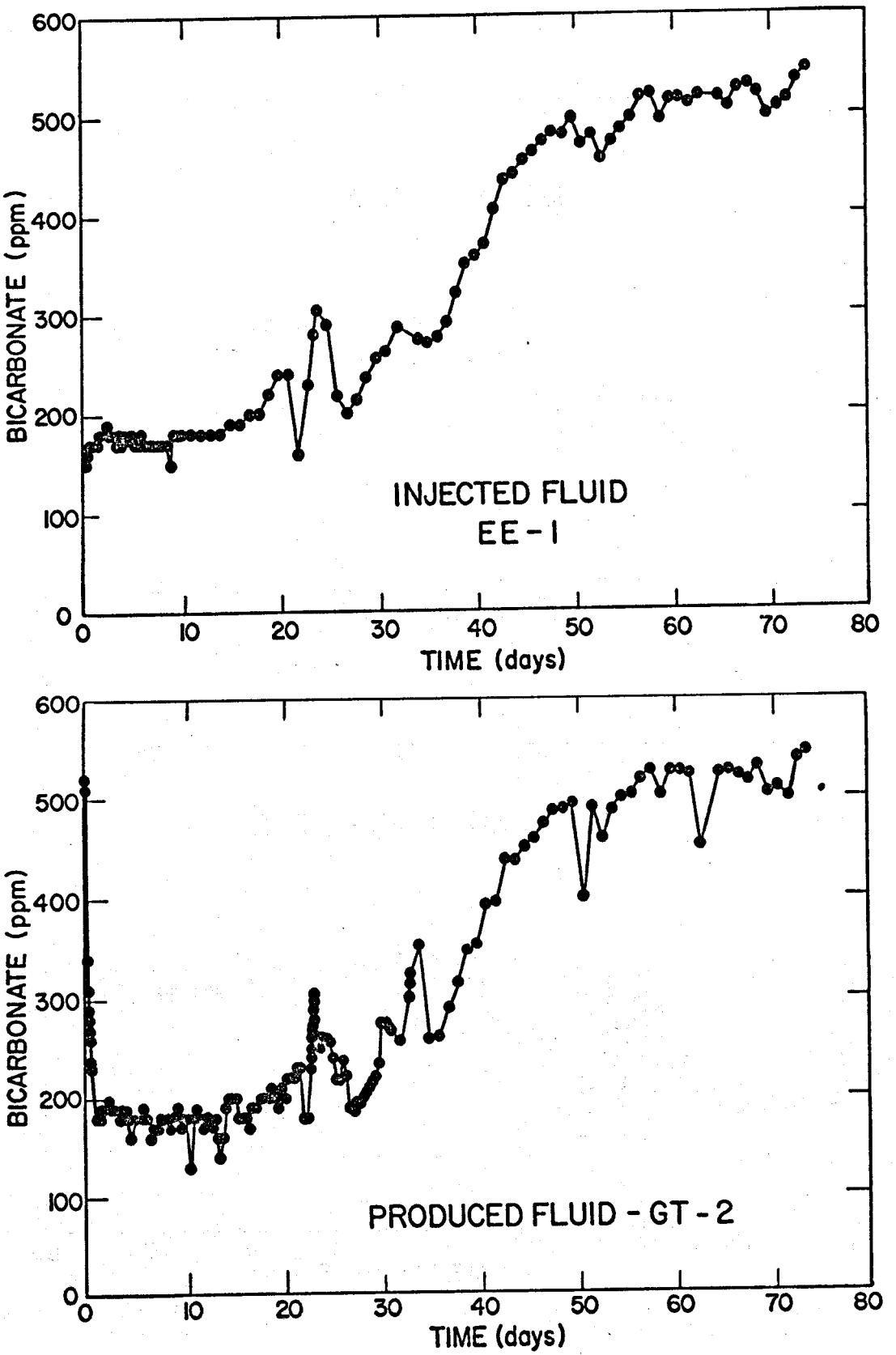

Fig. 5-9.
Bicarbonate concentrations in the injected and produced fluids.

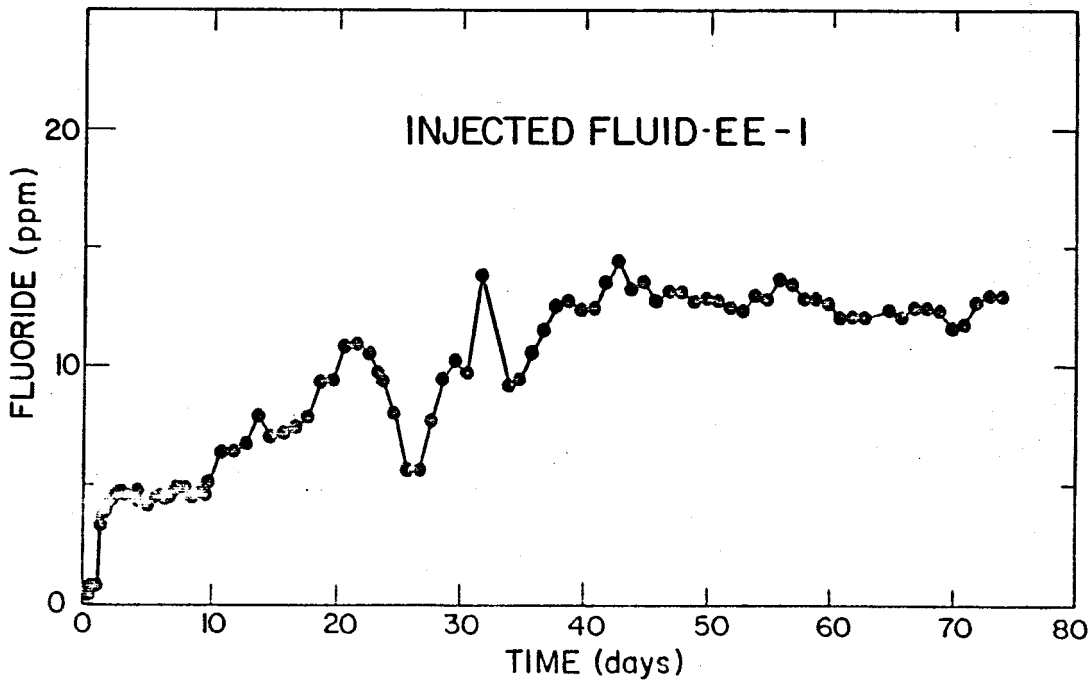

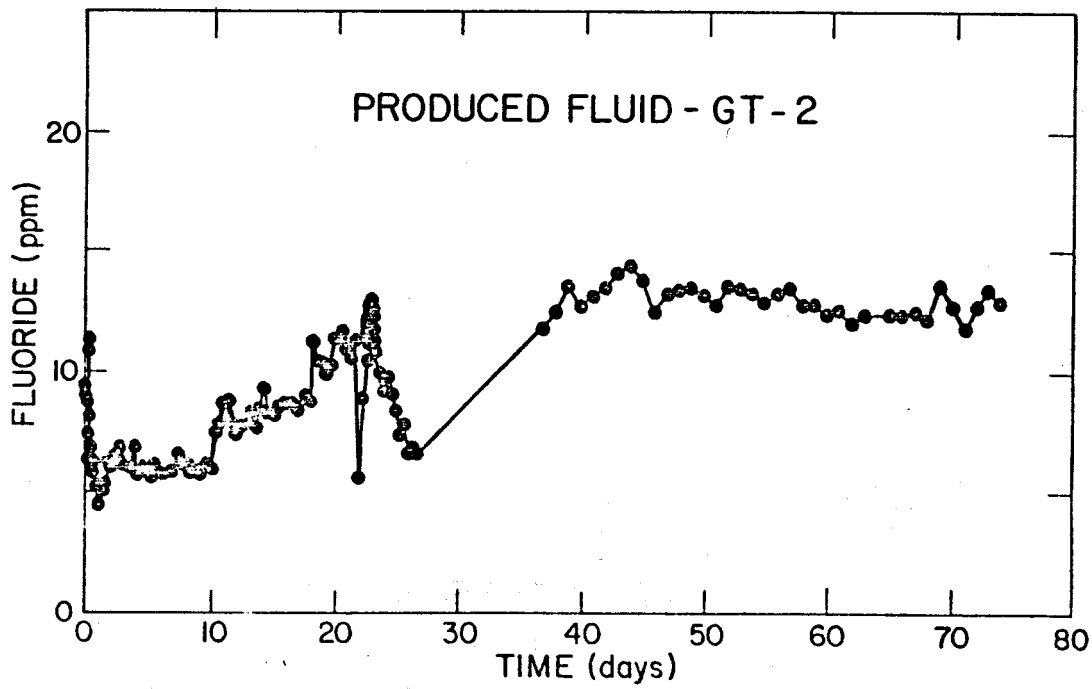

Fig. 5-10.
Fluoride concentrations in the injected and produced fluids.

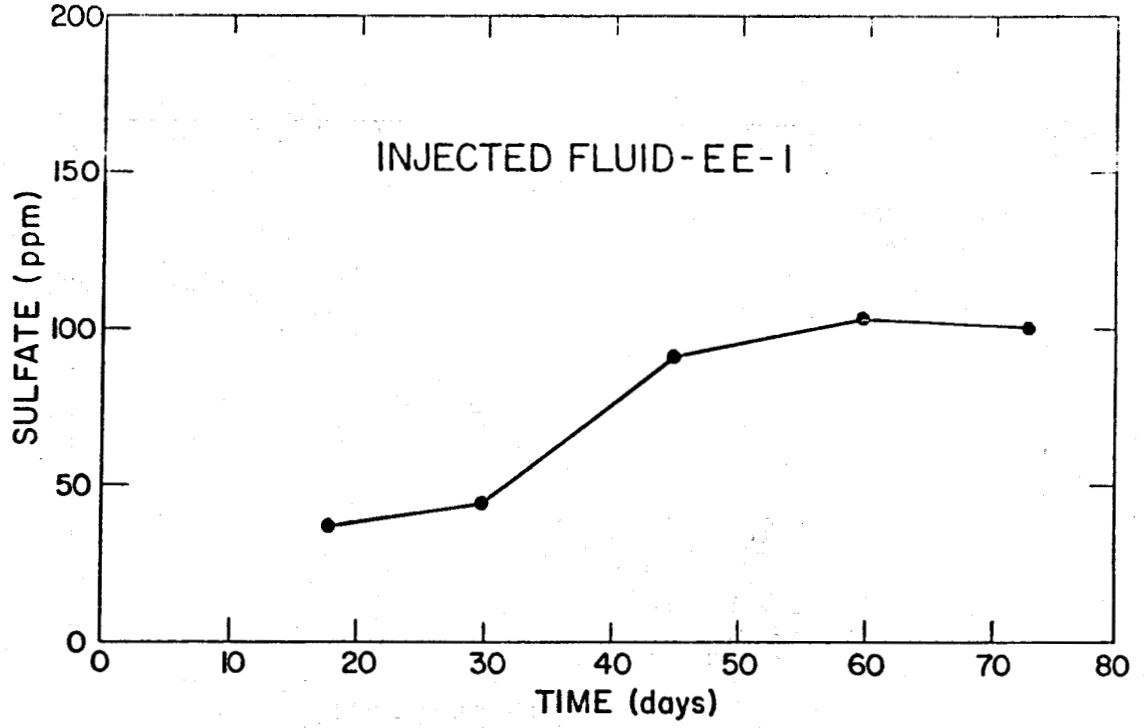

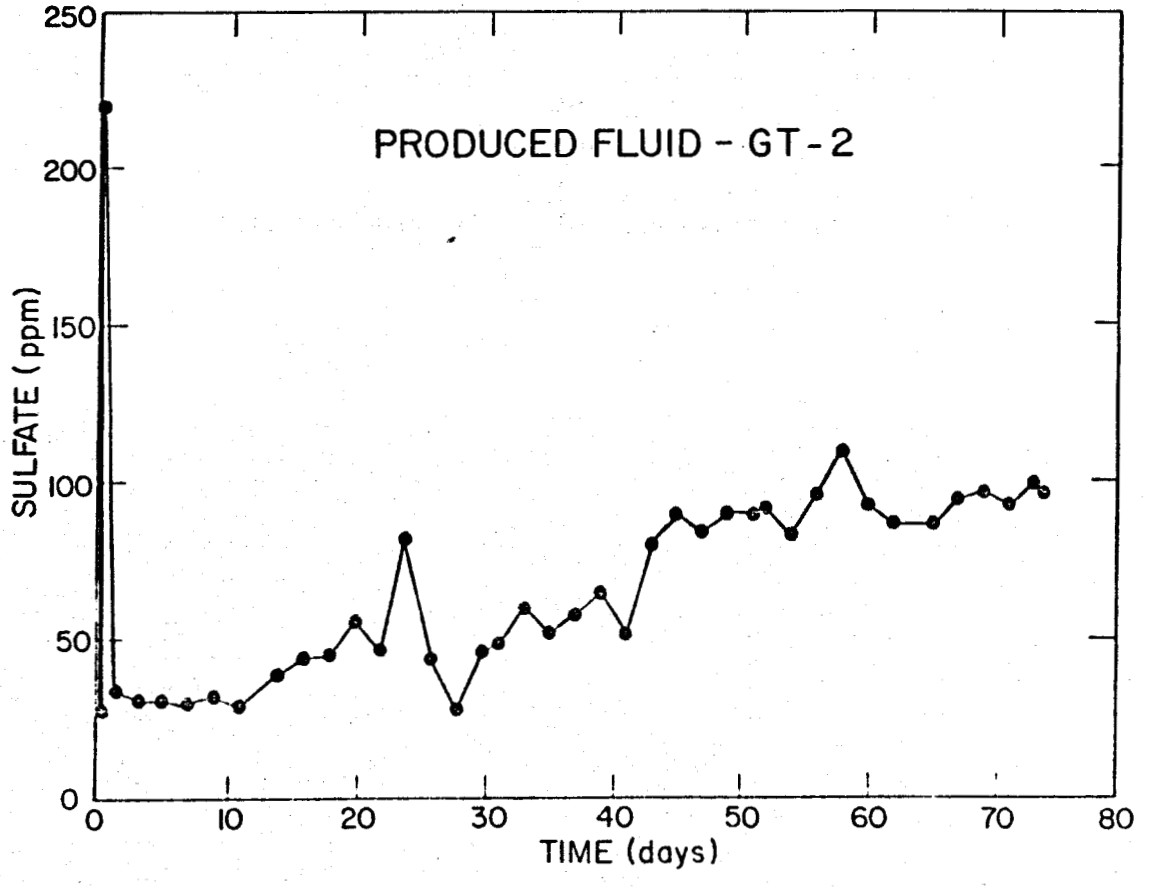

Fig. 5-11.
Sulfate concentrations in the injected and produced fluids.

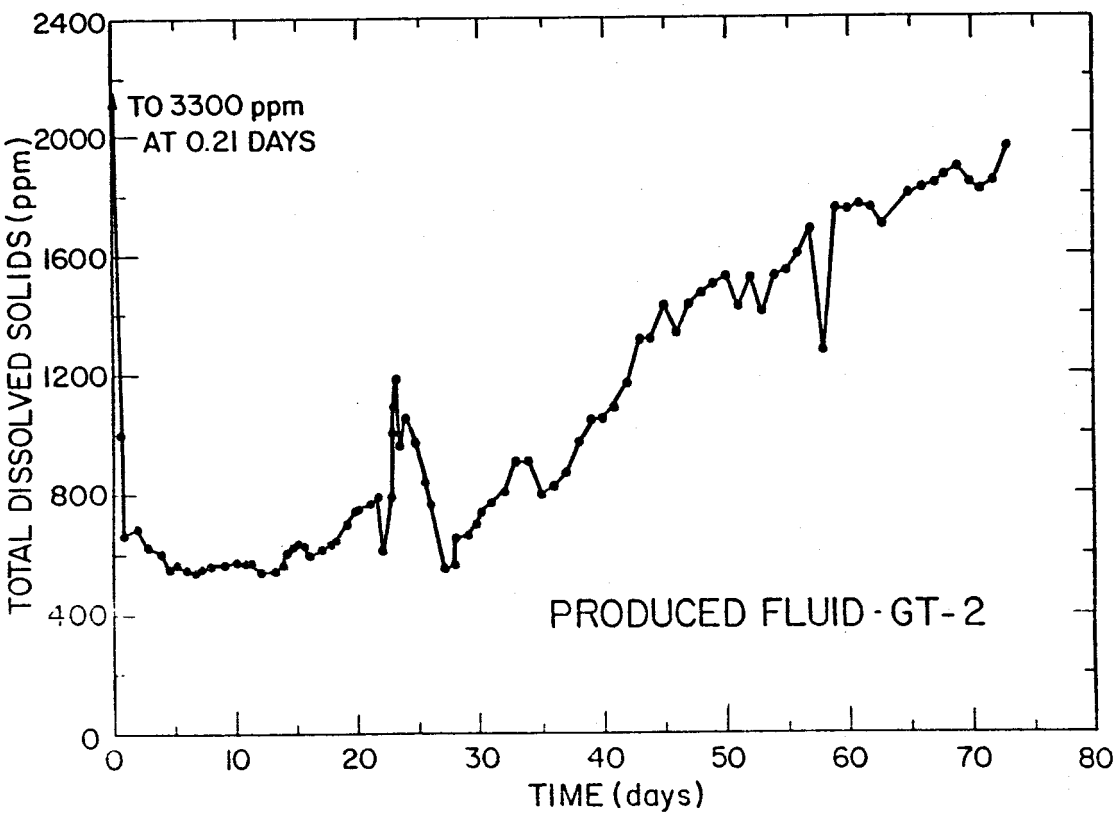

Fig. 5-12.
Calculated total dissolved solids for produced fluid.

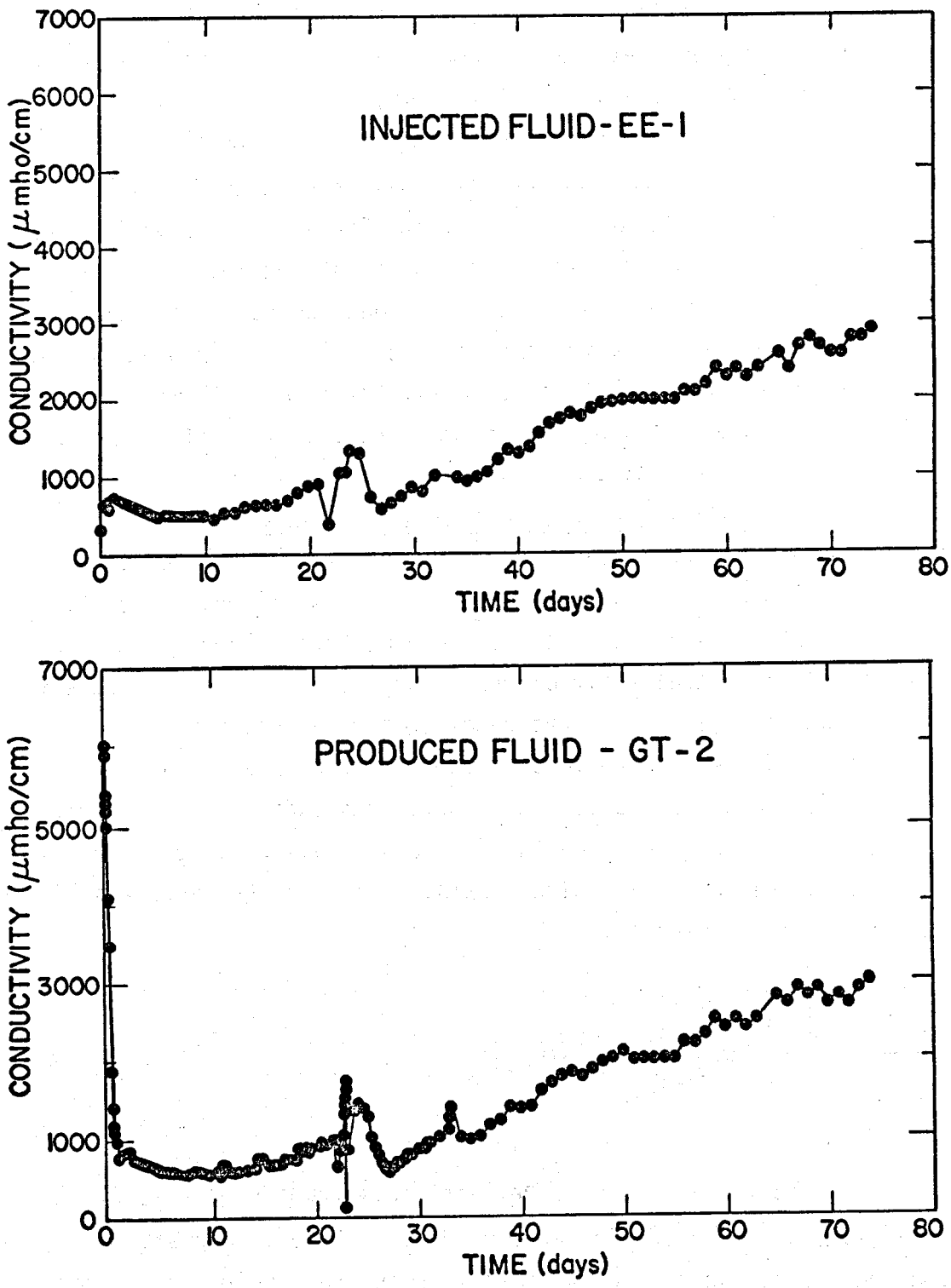

Fig. 5-13.
Solution electrical conductivity for injected and produced fluids.

because of the longer contact times with the rock and higher rock temperatures. This is seen as a local maximum on each graph at day 23. As the system was restored to operating pressures, makeup fluid replaced the fluid that had returned from the permeability storage. This large amount of makeup had a strong dilution effect as seen in the local minimum just after the 23rd day.

Dissolution, mixing, and transport of minerals continued to approach "steady state" conditions toward the end of the 75-day run. Several curves began to level off starting somewhere between day 40 and 50.

At the completion of the 75-day test only one successful gas analysis was achieved. A 3 ℓ-atm gas sample was separated from 140 ℓ of H_2O at 200-mm Hg total pressure. One liter-atm was scrubbed yielding the following analysis: 0.7 mg H_2S; 223 mg CO_2; O_2 and N_2 in a normal atmospheric ratio make up the bulk; N_2O trace; and NH_3 not detected.

Preliminary Interpretation - Reservoir

When the silica concentration exceeded the quartz saturation value at the measured temperature of the fluid entering the GT-2 wellbore, we sought explanations for the "high" SiO_2 concentrations. One mechanism requires that a small fraction of the fluid actually circulates through a portion of the reservoir, which is still at the initial reservoir temperature as described in the flow model of Section 4.5. According to this model, the change in silica concentration with time for that fraction of the flow corresponds to a first order rate depending on the difference between the silica saturation value of the highest reservoir temperature in contact with flowing fluid and the average silica concentration at any particular time:

$$\frac{d(\overline{SiO_2})}{dt} = k\overset{*}{a} \left[\left(SiO_2\right)^{sat}_{T=T_{max}} - \left(\overline{SiO_2}\right) \right] , \qquad (5\text{-}1)$$

where $k\overset{*}{a}$ is a constant that includes relevant mass transfer rates, dissolution kinetics rates, and a rock surface area to fluid volume parameter.

There are two distinct flow paths through the reservoir: one major path ($\sim$95% of the flow) through the main fracture system with its connected joints to GT-2B, and a secondary path ($\sim$5% of the flow) through a hot region that may be a highly fractured matrix-like section with a large effective volume and large

contact area. Thus information in Figs. 4-17 and 4-21 can be used in an equation to describe the rate of SiO_2 buildup. If no further dissolution or reprecipitation occurs in the cooler main flow path, then a differential material balance shows that the rate of accumulation of SiO_2 is due to three principal effects: the relative volumes of each flow path, the fluid loss rate to permeation, and the production of SiO_2 from active dissolution and/or displacement in the hot region. This is approximated in the following equation, assuming that the circulating time t is large compared to the mean residence time $\tau = (V_T/\dot{q}_T)$ in the system:

$$V \frac{d\overline{C}}{dt} = \dot{q}_T (C_{in} - \overline{C}) + \dot{q}_2 (1-e^{-ka^*\tau_2 f}) (C^\infty - C_{in}) \quad , \tag{5-2}$$

where

$$C_{in} = \frac{\dot{q}_T - \dot{q}_{loss}}{\dot{q}_T} \overline{C} + \frac{\dot{q}_{loss}}{\dot{q}_T} C^M \quad , \tag{5-3}$$

and

V_T = total system volume (fracture and wellbores),
V = total volume of all fracture flow paths = $V_1 + V_2$,
V_2 = volume of hot region flow path,
C^M = (SiO_2) makeup = concentration of SiO_2 in the makeup water,
C^∞ = $(SiO_2^{sat})_{T=T_{max}}$ = quartz controlled saturation concentration of SiO_2 at T_{max},
$\overline{C}$ = $(\overline{SiO_2})$ = average concentration of SiO_2 at time t,
k = dissolution mass transfer coefficient, cm/s,
a^* = rock surface area to fluid volume ratio, cm^{-1},
$\dot{q}_2$ = fluid circulation rate through hot region at time t,
$\dot{q}_T$ = total fluid circulation rate at time t,
$\dot{q}_{loss}$ = $\dot{q}_{makeup}$ = fluid loss rate to permeation at time t,
τ_2 = mean residence time in hot region = $V_2/\dot{q}_2$, and
f = fraction of plug flow conversion = function of dispersion in hot region ($0 \leq f \leq 1$).

By assuming all parameters on the right-hand side of Eq. (5-2) are approximately constant except $\overline{C} = (\overline{SiO_2})$, the equation can be integrated analytically to yield the time dependence of $\overline{C}$:

$$\overline{C} = C^{**} - (C^{**} - C_o\chi)e^{-\dot{q}_2 t/V}, \qquad (5\text{-}4)$$

with constants:

$$C^{**} = (C^{\infty} - B)\,(1 - e^{-ka^*\tau_2 f}) - B\,\dot{q}_T/\dot{q}_2 ,$$

$$\chi = -\frac{(A-1)\,\dot{q}_T}{\dot{q}_2} + A\,(1-e^{-ka^*\tau_2 f}) ,$$

$$A = (\dot{q}_T - \dot{q}_{loss})/\dot{q}_T ,$$

C_o = (SiO_2) = initial silica concentration, and

$$B = \frac{\dot{q}_{loss}}{\dot{q}_T}\, C^M .$$

In the extreme case of low water loss ($A \tilde{=} 1$, $B \tilde{=} 0$) and rapid reaction in the hot region ($ka^*\tau_2 f \gg 1$), Eq. (5-4) reduces to

$$\overline{C} = C^{\infty} - (C^{\infty} - C_o)e^{-\dot{q}_2 t/V} = C^{\infty} - (C^{\infty} - C_o)e^{-\xi t} . \qquad (5\text{-}5)$$

By using the solution to this equation for a negligible water-loss rate and fast kinetics with $\xi = 0.04\ s^{-1}$, $C^{\infty} = SiO_{2\,T=180°C}^{sat}$ = 220 ppm SiO_2 and C_o = $SiO_{2\,initial}^{(t=0)}$ = 80 ppm (the SiO_2 concentration of the initial EE-1 injected water), the predicted SiO_2 time history is given in Fig. 5-14. Rate equations of the same form were applied to the fluoride, sulfate, and the $^{87/86}Sr$ data (Figs. 5-15, 1-16, and 5-17) with the same success. Remarkably, the value of ξ is in each case $0.04\ s^{-1}$. Since in all probability more than one mineral is dissolving to contribute SiO_2, SO_4^{-2}, F^-, and Sr to the solution; this would imply that all dissolution rates were equal. Thus it appears that mass transfer rates, specifically mixing rates between various flow fractions, control the concentration history of these particular species in solution.

The possibility remains that saturated pore fluid is merely being displaced from the hot region at a rate $\dot{q}_2$. Further investigation is under way to consider the difference between active dissolution and pore fluid displacement by examining the time dependence of ratios of various ions including $Na^+/K^+/Li^+/Cs^+$ and $Cl^-/Br^-/I^-$.

As seen in Fig. 5-8 chloride concentrations also show a marked increase in time possibly indicating displacement and/or mixing with "saturated" pore fluid because no solid mineral source of chloride should exist with these reservoir

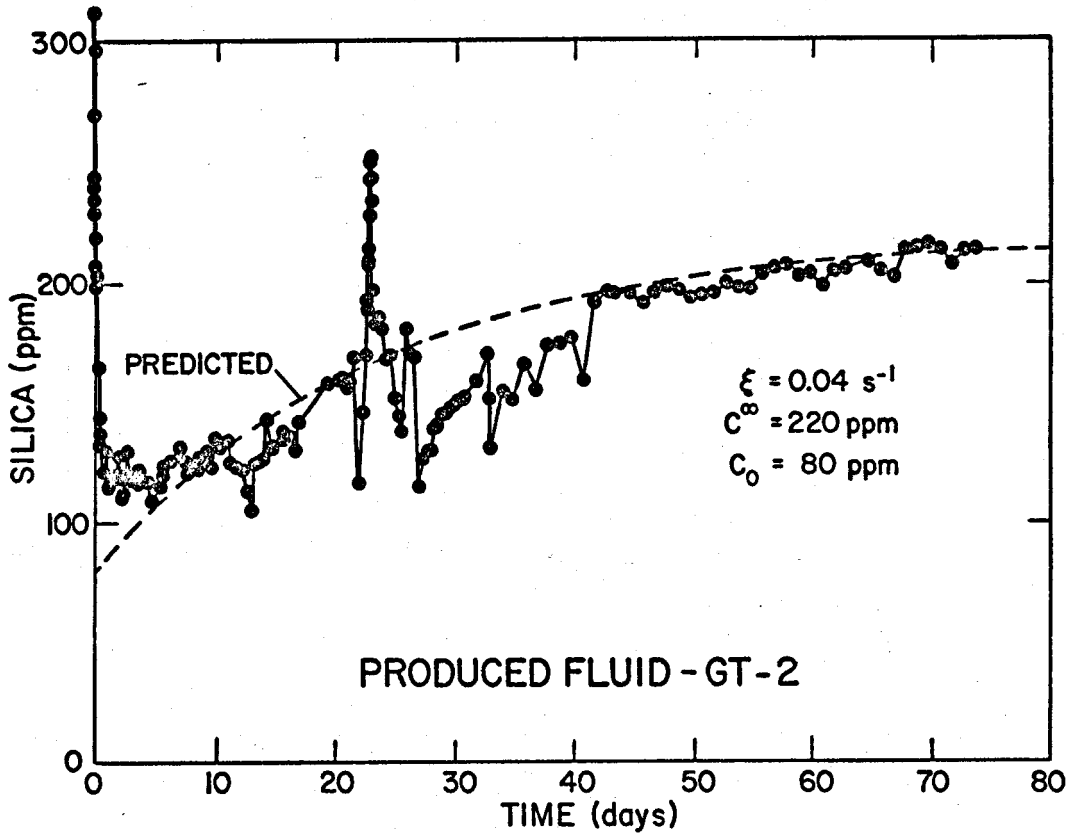

Fig. 5-14.
Observed and predicted silica concentrations in the produced fluid.

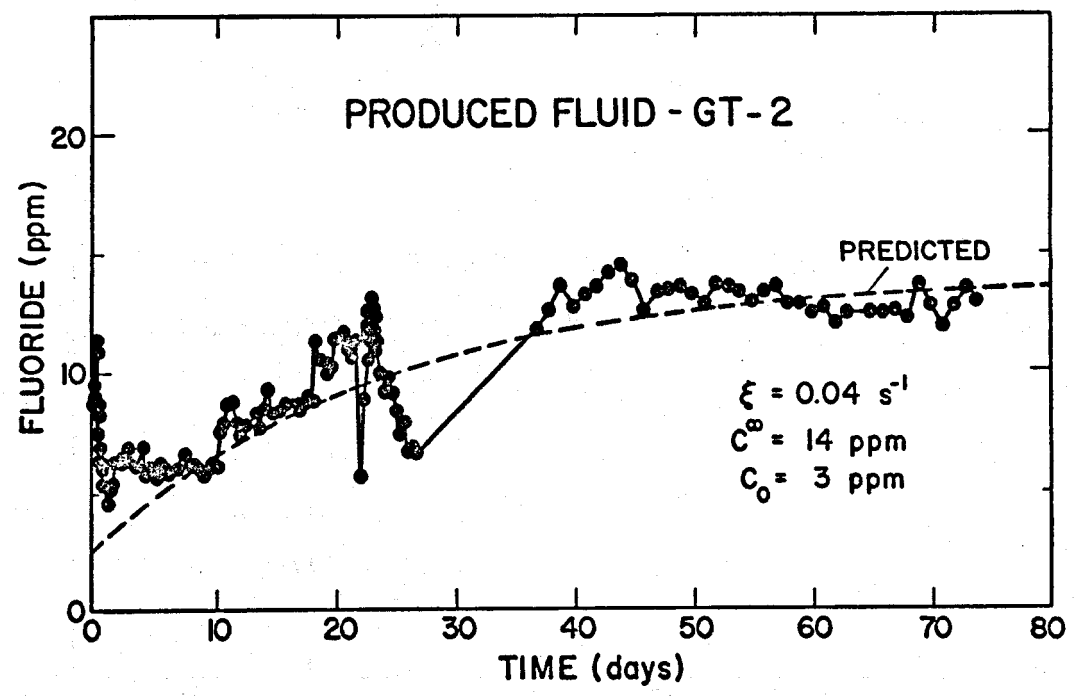

Fig. 5-15.
Observed and predicted fluoride concentrations in the produced fluid.

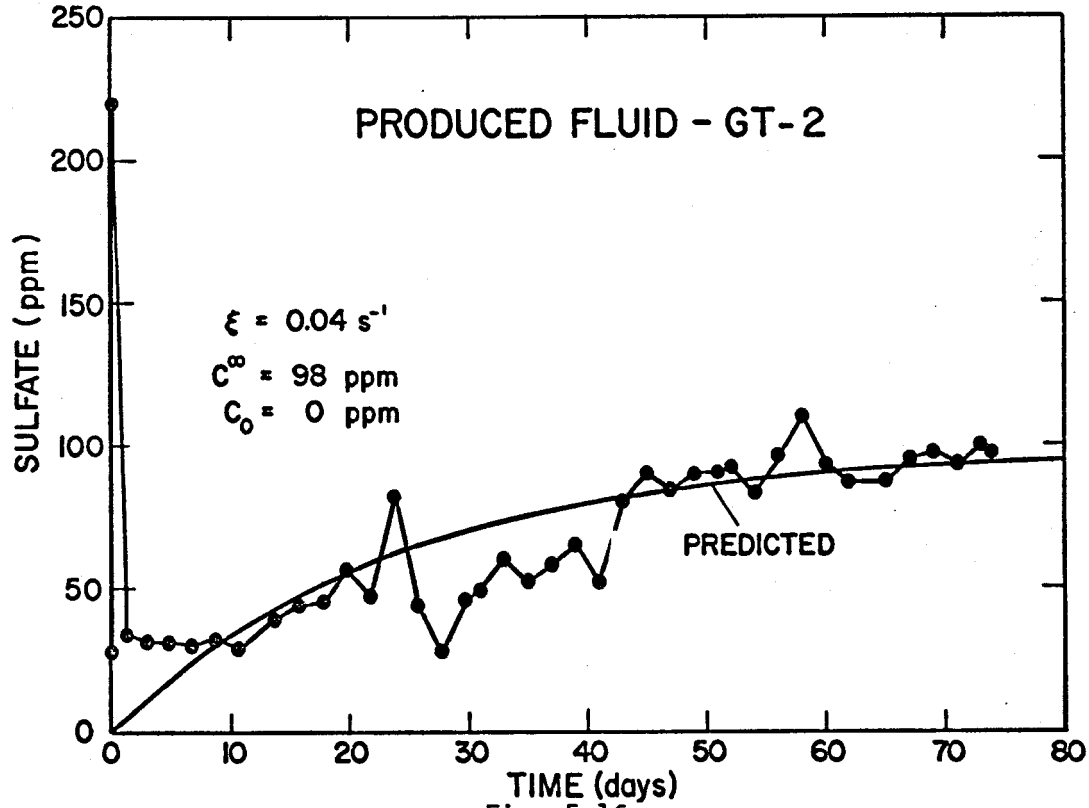

Fig. 5-16.
Observed and predicted sulfate concentrations in the produced fluid.

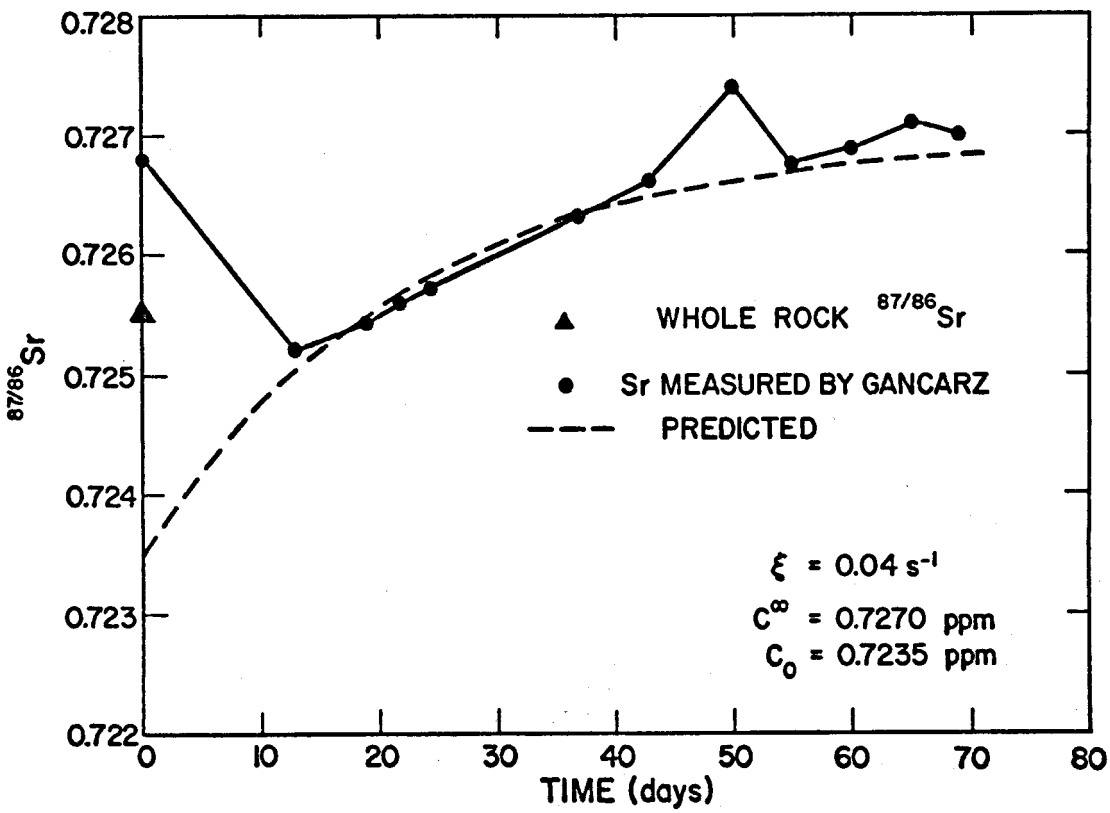

Fig. 5-17.
Observed and predicted $^{87/86}Sr$ concentrations in the produced fluid.

conditions. In addition, the rate of increase of Cl^- agrees with the empirical model proposed to explain SiO_2 buildup if a variable concentration source of Cl^- is being supplied to the flow path through the hot region.

We are determining the distribution of chloride in the GT-2 core samples by microprobe. If chloride is concentrated along calcite-filled fractures, the Cl^- concentration in solution could be dependent on calcite dissolution. The presence of Cl^- in fractures would indicate the Cl^- accompanied the carbonate-rich water, which migrated in and filled the fractures with calcite.

In the case of the bicarbonate concentration vs time, different conditions prevail. Calcite ($CaCO_3$) -- the principal contributor of $CO_3^=$ in solution -- has a retrograde solubility with temperature at constant P_{CO_3}.[9] Hence the lowest temperature of the reservoir may control the bicarbonate dissolution, and this lowest temperature is encountered in the main flow path as shown by temperatures measured at the EE-1-to-fracture system connection. As the fluid passes through the reservoir, however, it heats up and possibly reprecipitates calcite. In fact, there is some evidence of Ca depletion (see Fig. 5-2). If precipitation occurs, the highest temperature in the major flow connections will be the "equilibrium temperature" for Ca^{++} and HCO_3^- in solution. Figure 5-18 is a graph of observed (HCO_3^-) history along with the time dependent $(HCO_3^-)^{sat}$ at the EE-1 fracture connection temperature (see Section 3) and $(HCO_3^-)^{sat}$ at the measured 2621-m (8600-ft) temperature in the producing wellbore GT-2B. Possibly, only minor amounts of calcite are available to the fluid as it passes through the wellbore, and therefore the average reservoir temperature may control calcite solubility. In the first 35 days of the run the calcite solubility appears to be controlled by the temperature of the mixed production flow in GT-2B. The changes in bicarbonate concentration with time can be fit into Eq. (5-5) employed previously with $\xi = 0.04\ s^{-1}$ and $HCO_3^{-\ sat}$ = 325 ppm (determined by the reservoir drawdown temperature at 70 days). During the last 40 days of this run, however, the bicarbonate concentration approaches saturation corresponding to the EE-1 calculated injection temperature. The change in bicarbonate concentration with time after 26 days can be fit to the empirical rate in Eq. (5-5) if the time constant is changed to $0.07\ s^{-1}$ with a saturation concentration of 540 ppm (Fig. 5-19). Since this behavior was not observed for other major solution species, the change in the rate of (HCO_3^-) buildup may be caused by the shift to a new controlling mechanism. One possibility for the apparent shift in control of the calcite solubility to the EE-1 injection temperature is the major

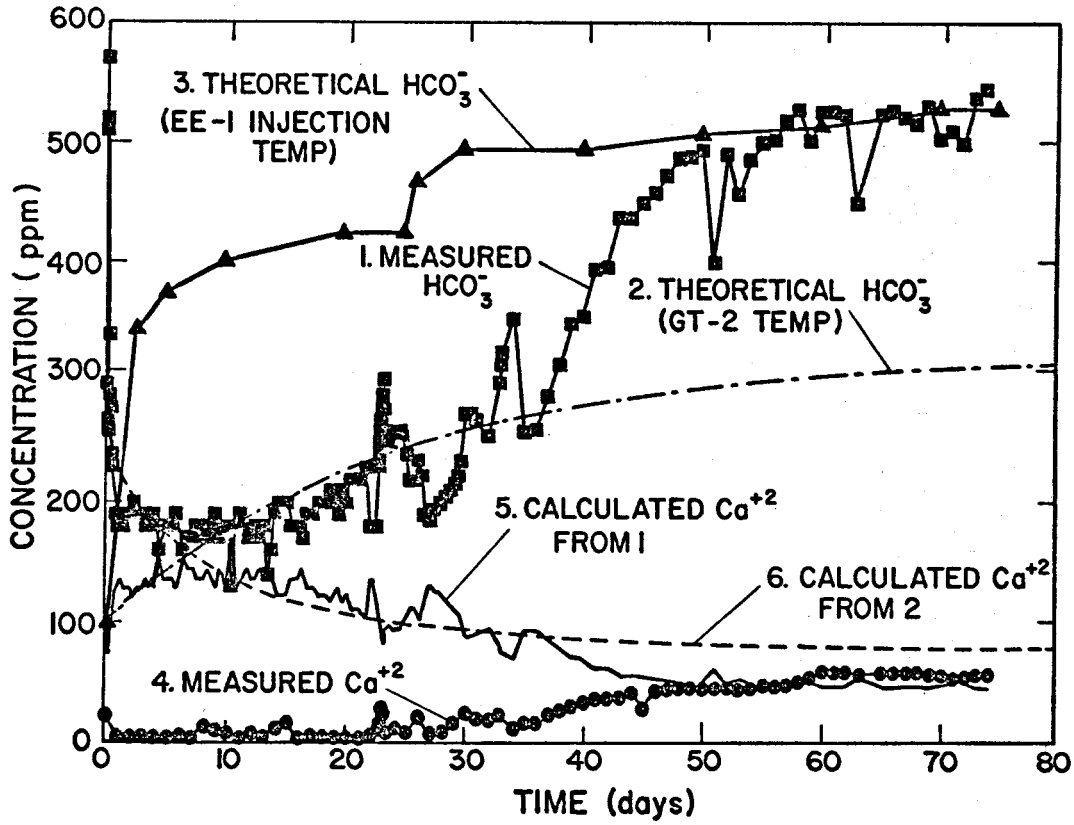

Fig. 5-18.
Observed and predicted Ca^{+2} and HCO_3^- concentrations in the produced fluid.

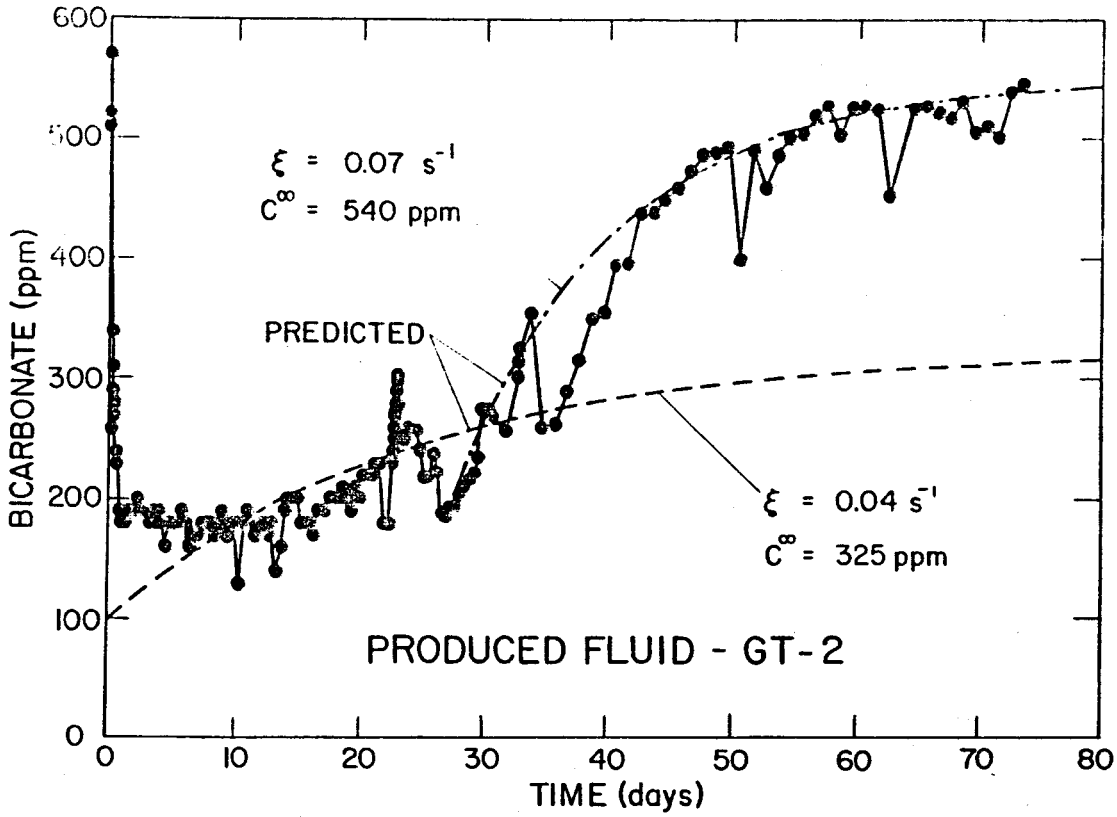

Fig. 5-19.
Observed and predicted bicarbonate concentration in the produced fluid.

change in downhole impedance and a doubling of the EE-1 flow rate that was observed during this period. If the impedance change is due to opening up of pre-existing fractures, the strategic position of calcite as a primary fracture-filling material could certainly increase the amount of calcite exposed to the fluid.

Calcium concentrations in equilibrium with calcite and (HCO_3^-) were calculated in the following manner from the thermodynamic data (equilibrium constants from Garrels and Christ)[9] assuming unit activity coefficients:

$$\frac{[Ca^{++}]\,[CO_3^{=}]}{[CaCO_3]} = 10^{-8.3} \tag{5-6}$$

$$\frac{[H^+]\,[CO_3^{=}]}{[HCO_3^-]} = 10^{-10.3} \text{ or } [CO_3^{=}] = \frac{10^{-10.3}}{10^{pH}}\,[HCO_3^-] \tag{5-7}$$

$$[Ca^{++}] = \frac{Ca \text{ ppm}}{40.1} \times 10^{-3} \tag{5-8}$$

$$[HCO_3^-] = \frac{HCO_3^- \text{ ppm}}{61} \times 10^{-3} \tag{5-9}$$

$$Ca^{++} \text{ ppm} = \frac{61\,(40.1)\,10^{2-pH}}{HCO_3^- \text{ ppm} \times 10^{-6}} \tag{5-10}$$

Temperature corrections are made according to Frear and Johnston.[10] Ca^{++} ppm corresponding to values of HCO_3^- observed and saturation concentration of HCO_3^- at the GT-2 production temperature are also plotted in Fig. 5-18. Notice that the calculated Ca^{++} based on observed HCO_3^- approaches the Ca^{++} observed at day 45. Until that time, however, the Ca^{calc} is much higher than the $Ca^{observed}$. For every 3 ppm $CO_3^{=}$ in solution contributed by calcite, there are 2 ppm Ca^{++} by stoichiometry. Assuming that all the HCO_3^- originally came from calcite, the observed Ca^{++} is an order of magnitude too low during the first 25 days of operation. This could be the result of precipitation of a noncarbonate calcium-rich mineral such as phillipsite $(K_2,Na_2,Ca)Al_2Si_4O_{12} \cdot 4{\cdot}5\ H_2O$. Charles[2,11] observes phillipsite as an overgrowth on plagioclase in his experimental apparatus at 200°C, and Deer, Howie, and Zussman[12] list phillipsite with other calcic zeolites,

which occur in either undersaturated or saturated SiO_2 environments. If phillipsite is indeed precipitating, we might see the effects of its precipitation in the N-K-Ca ratios in the fluid. Figure 5-20 is a triangular diagram showing the Na-K-Ca ratios for the produced Fenton Hill fluid. The time history moves along a constant K line, and although they become richer in Ca relative to Na with time, the sense of the trend cycles up and down as if calcite is dissolved (and therefore increasing the Ca/Na ratio) followed by dissolution of albite (which lowers the Ca/Na ratio along the constant K line). The thermodynamics of dissolution and precipitation in this system have not been examined to see if phillipsite is indeed stable under these conditions, and there is inconclusive evidence that phillipsite exists in the Fenton Hill reservoir.

In the Na-K-Ca triangular diagram of Fig. 5-21, the changes in fluid and mineral compositions with time are shown. In addition, composition changes were observed by Charles[2,11] in a laboratory circulating system at 200°C using a biotite granodiorite from GT-2 and initially distilled water. In his circulating system, the fluid composition changes away from the Na-K-Ca ratios of the whole rock toward the starting solution values for the Fenton Hill reservoir. Apparently, the laboratory rock-water system has not achieved the same degree of reaction completion as is observed at the Fenton Hill reservoir. Therefore, changes in solid phases may correspond to early changes in the solid phases in the Fenton Hill reservoir.

Preliminary Interpretation - Surface Equipment

There were no indications of any solid deposition or corrosion in any surface piping during the Phase I, Segment 2 run. This statement is based on visual observation by J. Skalski. However, he does mention the presence of a "chalky" material produced by evaporation on some exterior components, which dissolves in acid with effervescence and is presumed to be calcite.

During the week of February 20, a crystalline material had filled the 7.94-mm (5/16-in.) stainless steel line, which had not yet been used for gas sampling. (The line had been left running to prevent its freezing.) The material was analyzed by x-ray diffraction and by electron microprobe and was found to be calcite with minor amounts of Sr (probably substituting for Ca). No silica was found.

According to Johnston and Williamson[13] the solubility of calcite in water at 16°C at $P_{CO_2} = 7.63 \times 10^{-5}$ atm is 0.040 g/ℓ. Frear and Johnston[10] report that "the temperature coefficient of solubility is, within the accuracy of the

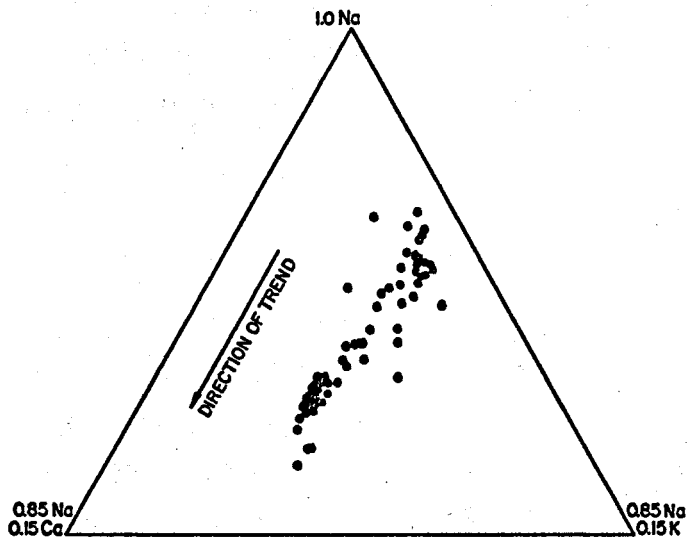

Fig. 5-20.
Na-K-Ca ratios observed in the produced fluid during Phase I.

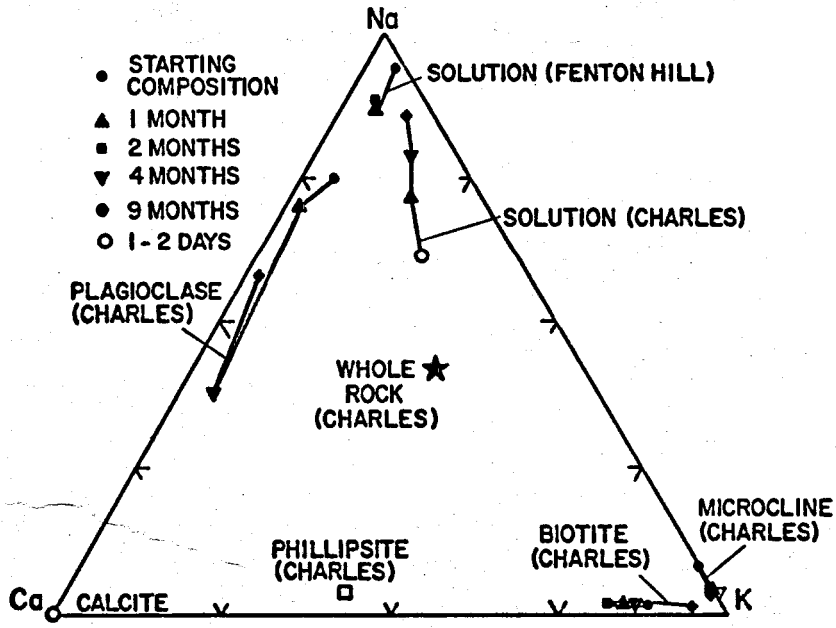

Fig. 5-21.
Comparison of laboratory and field measurements for rock and solution samples using biotite granodiorite as the starting material.

measurements independent of the partial pressure of carbon dioxide particularly in the range of 0.003 to 1 atm; consequently it suffices to give the ratio r of the solubility at T to that at 25°C." The ratio r is calculated by the formula:

$$\log r = (830/T°K) - 2.78 \quad . \tag{5-11}$$

By assuming Eq. (5-11) to hold at the measured P_{CO_2} in the Fenton Hill geothermal fluid of 6.152×10^{-5} atm, for T = 140°C, r = 0.17. The solubility of calcite at $P_{CO_2} = 7.63 \times 10^{-5}$ atm and 25°C is 0.0323 g/ℓ, therefore, the solubility of calcite at 140°C and $P_{CO_2} = 7.63 \times 10^{-5}$ atm is 0.00548 g/ℓ. The calculated Ca^{++} concentration is then 0.00219 g/ℓ or 2.19 ppm. The measured Ca^{++} concentration at day 20 is 3.3 ppm (see Fig. 5-2). According to the calcite equilibria cited earlier, the following equations develop:

$$\frac{[Ca^{++}]\,[CO_3^{=}]}{[CaCO_3]} = 10^{-8.3} \tag{5-12}$$

$$[CO_3^{=}] = \frac{10^{-10.3}[HCO_3^{-}]}{[H^+]} = 10^{-10.3}\,10^{-6.4}\,10^{-1.47}\,\frac{P_{CO_2}}{[H^+]^2} \tag{5-13}$$

$$[HCO_3^{-}] = 10^{-6.4}\,\frac{[H_2CO_3]}{[H^+]} \tag{5-14}$$

$$[H_2CO_3] = 10^{-1.47} P_{CO_2} \quad , \tag{5-15}$$

or

$$\frac{[Ca^{++}]\,P_{CO_2}}{[CaCO_3]\,[H^+]^{-2}} = 10^{9.87} \text{ at } 25°C \quad . \tag{5-16}$$

If at constant pH and constant $[Ca^{++}]$, the P_{CO_2} drops (as it would when the gas phase separates from geothermal fluid at an expansion valve); the $CaCO_3$ solubility would also have to drop enough to cause precipitation.

5.2. Trace Element Analysis (T. Beddoe, I. Binder, E. A. Bryant, A. J. Gancarz, J. S. Gilmore, R. J. Vidale, and R. A. Williams)

Precise, sensitive chemical analyses for trace elements found in the fluids flowing through the Fenton Hill reservoir were conducted to provide reconnaisance information concerning changes within the system that might be useful in determining the extent of rock-water interaction. Neutron activation analysis was chosen because of its great sensitivity for some elements and its capability of yielding data on many elements from the analysis of one sample.

This method involves exposing a sample to a high dose of neutrons, such as can be obtained in a nuclear reactor, and then measuring the resulting radioactivities to determine what was produced and how much. From this information one can calculate the amounts of elements present for those that produce suitable radioisotopes.

Freeze drying has been used to reduce approximately a 200-ml fluid sample taken at Fenton Hill to a solid mass that could be conveniently irradiated in the Omega West Reactor at LASL. This method increases the concentrations of trace species in the sample to increase sensitivity but also may introduce some contamination and inhomogeneity. All sampling and processing apparatus was carefully washed before use. Polyethylene equipment was used to reduce the introduction of additional inorganic elements. Freeze drying removes water by sublimation and reduces the chance that any solid will redissolve.

In addition to the Fenton Hill liquid samples, a 500-g rock core obtained at a depth of 2714 m (8904 ft) was treated to obtain samples of the component minerals. The rock was initially disaggregated by numerous cycles of rapid cooling to the liquid nitrogen temperatures (-196°C), followed by rapid warming to room temperature. The mixture was sieved to obtain a 50-200 mesh fraction between several of the cycles. The properly sized mixture was then separated by use of a hand magnet, a Frantz magnetic separator at several field strengths, and heavy liquids that separate fractions according to density differences by a sink-float technique. The six resulting mineral fractions represent apatite, biotite, magnetite, combined plagioclase and quartz, potassium feldspar, and sphene. An optical examination of the fractions showed the mineral purity to range from better than 50% to exceeding 95% for the desired component.

Either about 100 mg of freeze-dried solids or 20-350 mg of mineral separates were loaded into a special polyethylene vial for the reactor irradiation. These very clean plastic vials show a significant amount of chromium-51 radioactivity following irradiation, causing a background that accounted for all the chromium found in most of the samples. The irradiations were carried out in the Thermal-Column-Rabbit-2 position of the Omega West Reactor for approximately 7 h. The neutron dose received by the sample was monitored by an accompanying chromium wire.

After allowing the intense activities to decay to an acceptable level, the samples were individually examined using a calibrated, large-volume Ge(Li) gamma-ray detector coupled to a multi-channel pulse-height analyzer. The spectral data were immediately analyzed by computer program RAYGUN and recorded on magnetic tape for later computer evaluation with GAMANAL.[14] Such spectral measurements were made several times for each sample.

Using published neutron-capture cross sections, the resulting identifications and measurements were converted into the mass of each element found in the sample, and the fraction of the total solid mass was irradiated and analyzed. Initial results are given in the accompanying tables for several fluid samples (Table 5-I) and the mineral separates (Table 5-II) for the 2714-m (8904-ft) core sample. Values for the whole rock are also given for neutron activation as well as wet chemical analysis. Individual mineral compositions for the 2714-m (8904-ft) core sample are given in Table 5-III.

In addition, delayed neutron counting on activated liquid samples was used to determine uranium concentrations in the produced GT-2 fluid. Concentrations ranged from 0.1 to 2.0 ppb.

It is premature to arrive at any significant conclusions based upon the limited data presently available, but we are encouraged at the general consistancy for the concentrations of several elements and similar results obtained for injected EE-1 and produced fluid GT-2 collected at similar times. Two samples in particular stand out as not conforming to the general pattern: N-1b and 66G. For N-1b this is likely due to the extended residence time in contact with rock for the water that first was produced at GT-2. However, this does not apply to sample 66G, which was obtained during continuous operation. Measurements will be repeated for 66G along with others collected shortly before and afterwards.

TABLE 5-I

CONCENTRATIONS OF ELEMENTS IN GEOTHERMAL WELL FLUID SAMPLES AS DETERMINED BY NEUTRON ACTIVITIES[a]
ng/gH_2O (ppb)

Sample[b]	Time Collected	Na	Ca	Sc	Fe	Co	Zn	As	Br	Sr	Mo	Sb	Cs	Ba	Eu
N-1b	28 Jan 78 1845		8,224		1,860	0.27	1,270		5,603	1,223		1.88	1,043	87	0.080
33G	2 Feb 78 1500	107,100	4,505	0.46	50	0.75	11	60	440	125	14.3	1.85	178	29	0.016
36G	3 Feb 78 1500		6,890	0.050	85		9.9		445	747		1.5	195		0.015
	6 Feb 78 2300						1.9			156		1.15	184	62	
56G	10 Feb 78 0700									210		1.3	183		0.015
66G	13 Feb 78 1500	25,200	12,900	0.25	459	0.16	131	386	382	356		114	169	48	0.010
75G	16 Feb 78 1500								524	220		1.3	228		0.016
84G	19 Feb 78 1500		5,400	0.057					437	221		1.5	239	41	0.018
130E	6 Mar 78 1200														
130G	6 Mar 78 1200														
137G	13 Mar 78 1200	333,000	78,840		219			324	1,460	637	55		400		
141E	17 Mar 78 1200	363,000	42,900		563	0.13		224	1,606	801	46		423	132	
141G	17 Mar 78	349,000	45,400		373			266	1,670	585	45		429		

[a] No entry does not necessarily indicate a non-detectable concentration. Additional results will be added to this tabulations based on further analysis of spectra.

[b] Sample #'s correspond to major element sample # except N-1b which was taken between 9G and 10G at the producing GT-2B wellhead.

TABLE 5-II

ELEMENTAL COMPOSITION OF MINERAL SEPARATES AND WHOLE ROCK FROM CORE 2714 M (8904 FT) ppm (μg/g)

Element	Whole Rock	Av. Biotite Granodiorite[a]	Zircon	Sphene	Apatite	Plagioclase	K-feldspar	Biotite	Magnetite
Na	22,800	24,600	202	~0	1,260	63,150	8,830	~0	294
Mg	-	8,380	-	-	-	-	-	-	-
Al	71,000	76,600	-	-	-	-	-	-	-
K	38,000	35,000	~0	~0	~0	~0	130,000	84,200	443
Ca	20,000	22,200	~0	176,000	375,000	41,500	2,590	~0	~0
Sc	1,310	-	282	348	35.2	53.1	7.15	1,360	20
V	45.9	-	-	-	-	-	-	-	-
Cr	109	-	-	-	-	-	-	-	-
Mn	570	705	54.4	1,520	727	367	122	6,790	1,420
Fe	27,700	43,400[b]	~0	15,400	4,470	4,530	1,030	18,000	730,000
Co	7.29	-	~0	1.69	0.86	1.76	0.18	69.7	44
Zn	88.9	-	~0	~0	~0	54.3	~0	1,120	70
As	1.38	-	~0	11.7	276	4.47	~0	~0	1.0
Br	~0	-	40.6	~0	~0	~0	~0	~0	8.97
Sr	430	372	~0	~0	~0	303	735	~0	638
Zr	~0	-	495,000	~0	24,800	~0	~0	~0	44,000
Mo	10.1	-	298	378	275	~0	4.62	~0	~0
Ag	~0	-	~0	~0	~0	1.43	~0	~0	-
Sb	0.263	-	~0	1.77	14	0.41	~0	1.29	~0
Cs	4.85	-	~0	~0	~0	2.18	3.00	43.1	~0
Ba	1,520	-	~0	1,030	896	~0	6,700	549	~0
La	68.0	-	~0	1,020	336	17.3	3.54	60.0	14
Ce	145	-	~0	5,860	981	~0	10.2	~0	38.6
Nd	48.5	-	443	3,270	321	~0	0.85	~0	~0
Eu	1.30	-	8.13	88.6	4.99	~0	0.19	~0	-
Tb	1.80	-	3.76	179	1.83	~0	0.25	~0	0.43
Dy	11.7	-	35.5	950	~0	~0	1.42	~0	2.0
Tm	1.032	-	~0	91.2	63.6	~0	0.11	~0	~0
Yb	4.57	-	399.0	1,920	24.3	~0	2.79	~0	7.8
Lu	1.75	-	47.1	143	6.71	~0	0.23	~0	0.90
Hf	9.50	-	2,880	63.8	80.2	13.0	128	42.0	26
Ta	3.38	-	56.0	206	1,040	6.68	1.36	~0	2.0
W	~0	-	39.4	~0	183	~0	~0	~0	~0
Th	13.2	-	49.5	458	172	~0	0.66	6.17	2.16

[a] From Laughlin and Eddy (1977)

[b] Large variation from sample to sample.

No entry means that the element was not detected because its concentration was below the sensitivity of the method.

- Not observable with this method.

TABLE 5-III

MINERAL COMPOSITION OF GT-2 CORE SPECIMEN FROM 2714 m (8904 FT)

	Modal Volume %	Calculated Weight %
Quartz	26	26
Plagioclase	37	37
K-feldspar	20	19
Biotite	10	11
Sphene	2.0	2.6
Chlorite	0.2	0.2
Magnetite	1.5	3.0
Zircon	~0.05	~0.1
Apatite	2.0	2.0
Calcite	0.3	0.3
Epidote	2.2	2.8

A substantial amount of data remains to be evaluated to supplement presently available results, and further water samples will be processed and analyzed. Of special interest will be water samples collected for both EE-1 and GT-2 at the same time and a sample of the makeup water.

A more accurate calibration for the neutron activation of various elements will be made by irradiating and analyzing a U. S. Geological Survey standard rock sample for which the composition has been well determined. Not all the elements detected in the water samples have been precisely measured in the USGS standards, and for these elements individual standards will have to be prepared.

5.3. Strontium Isotope Ratio Measurements (A. J. Gancarz)

Different minerals have different rubidium-to-strontium (Rb/Sr) ratios, and as a consequence of the radioactive decay of ^{87}Rb they have different $^{87}Sr/^{86}Sr$. This, coupled with the evidence of the rock-water chemical interaction in the actual field operation and the differential reactivity of minerals observed in laboratory experiments,[2,11] suggests that it might be possible to detect in the field experiment which minerals are reacting preferentially by monitoring the isotopic composition of Sr in the circulating water. Strontium isotopic data were measured for water collected during the 75-day operation. In this unique application, Sr has been used apparently for the first time as a hydrologic tracer. Mixing of fluids from different sources and the interactions of the water with the rocks were observed by monitoring the isotopic compositions.

Three types of water samples were analyzed for Sr isotope ratios: (1) heated water produced at GT-2, designated G; (2) a mixture of cooled water and makeup water, designated E, which is pumped back into the hot-rock reservoir; and (3) filtered makeup water from the holding pond, designated M. In general, all three types of samples were collected simultaneously at various times throughout the 75 days. Thirty-ml aliquots were evaporated and processed to separate the Sr sample. The Sr was analyzed on a National Bureau of Standards type 15.2-cm (6-in.) mass spectrometer. The analytical data are presented in Table 5-IV and illustrated on Fig. 5-22.

Strontium isotope data for each of the three types of fluids (G, E, and M) are presented in Fig. 5-22. For any set of samples collected at a given time, we observe in all cases that the $^{87}Sr/^{86}Sr$ in the fluid produced from the hot-rock reservoir is greater than that in the cooled injected fluid being cycled back down into the rock reservoir. Furthermore, the $^{87}Sr/^{86}Sr$ in the injected

TABLE 5-IV

FENTON HILL SR ISOTOPIC DATA

Day	Sample	$^{87}Sr/^{86}Sr$	Day	Sample	$^{87}Sr/^{86}Sr$
0	N-1a	0.72678 ± 3[a]	23.5	110M	0.70987 ± 7
13	56E	0.72385 ± 6	37	130E	0.72579 ± 12
13	56G	0.72525 ± 8	37	130G	0.72630 ± 12
13	56M	0.71250 ± 18	43	137E	0.72622 ± 11
19	75E	0.72481 ± 4	43	137G	0.72668 ± 26
19	75G	0.72542 ± 8	50	144E	0.72678 ± 12
19	75M	0.71582 ± 14	50	144G	0.72741 ± 11
22	84G	0.72561 ± 12	54	148G	0.72676 ± 13
23	88G	0.72578 ± 5	59	153G	0.72689 ± 4
23.25	96G	0.72578 ± 2	65	158G	0.72704 ± 11
23.5	110E	0.72556 ± 17	69	162G	0.72700 ± 8
23.5	110G	0.72571 ± 10	73	166G	

[a]Accuracy expressed as 0.72678 ± 0.00003.

fluid is greater than that in filtered makeup water. Because the injected fluid is a mixture of produced fluid and makeup water, its intermediate value of $^{87}Sr/^{86}Sr$ is the result of mixing ^{87} Sr-rich produced fluid with ^{87}Sr-poor makeup water. Calculated G/M-Sr-atom mixing ratios range from 0.05 to 0.1 and are in reasonable agreement with the G/M water volume mixing ratios expected if the Sr concentrations are approximately equivalent.

Figure 5-23 is an enlargement of part of Fig. 5-22 included to show in detail the relationship between the produced, G, and injected, E, waters. The G data are indicated by squares and the E by circles. Again the ^{87}Sr-rich nature of the G water relative to the E water is apparent. The mean residence time of water in the reservoir itself determined by Na-fluorescein dye tracer experiments is 1 to 2 h compared to a total circulation time of 3 to 4 h (see Section 4.2). Because this is a continuously circulating system, two effects are apparently causing the enrichment of ^{87}Sr: (1) the reaction between the circulating fluid and the reservoir rock and (2) material balance effects caused by interactions among the permeation water loss rate, the main circulating flow, and a certain small fraction of flow, which mixes with indigenous pore fluid contained in a hot region of the reservoir.

At the beginning of the circulation experiment, the first produced fluid had been in the fracture system for ∿3 months and had a high $^{87}Sr/^{86}Sr$ of 0.72678 ± 0.00003. Initially before recirculation, the injected fluid was filtered well water stored in the EE-1 pond and had $^{87}Sr/^{86}Sr = 0.70981 \pm 0.00008$ (see Fig. 5-22). During the first 10 days, the injected ^{87}Sr-poor water interacts with the reservoir and is enriched in ^{87}Sr, but because of the high makeup rate a large fraction of the injected fluid is ^{87}Sr-poor makeup water, and a net decrease in the $^{87}Sr/^{86}Sr$ from initial values was observed in the produced fluid between successive circulation cycles during this early period. This is consistent with observations for other chemical species (see Sections 5.1-5.2).

During the succeeding ∿40 days, the injected ^{87}Sr-poor fluid continues to be enriched in ^{87}Sr as it interacts with the reservoir. However, in this case, the effect of addition of ^{87} Sr-rich Sr from the reservoir is sufficient to cause a net increase in $^{87}Sr/^{86}Sr$ of the produced fluid. This is reasonable as the percentage of ^{87}Sr-poor makeup water has decreased rapidly from 100% at day 0 to 5% at day 25, and it remained at about the 5% level during the rest of the operation (see also Section 4.3). The parallel nature of the injection E and production G curves from days ∿25 to 50 suggests a quasi-steady-state regime in

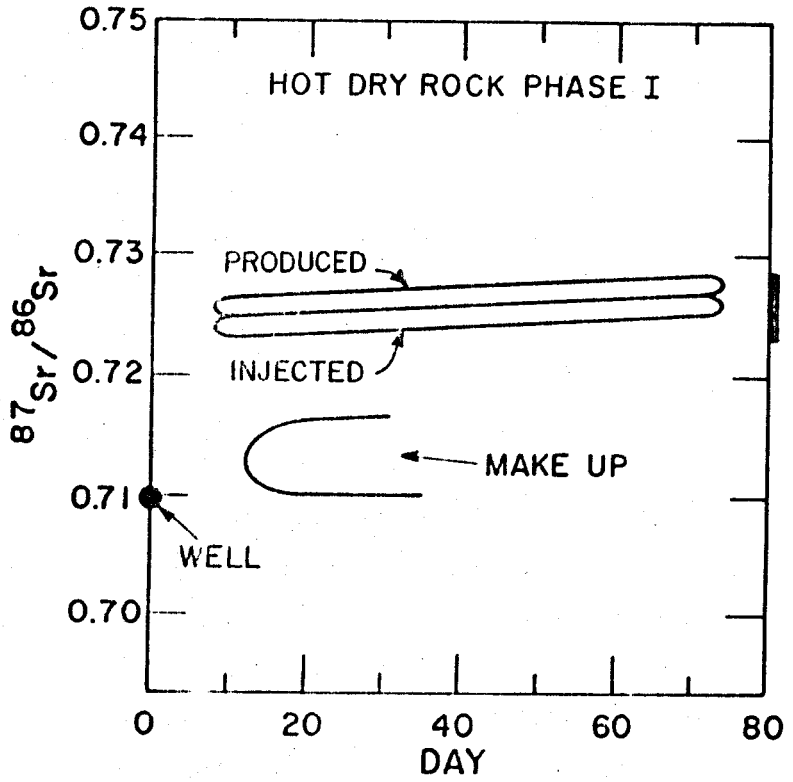

Fig. 5-22.
$^{87}Sr/^{86}Sr$ ratio history during Phase I for injected, produced, and make-up fluids.

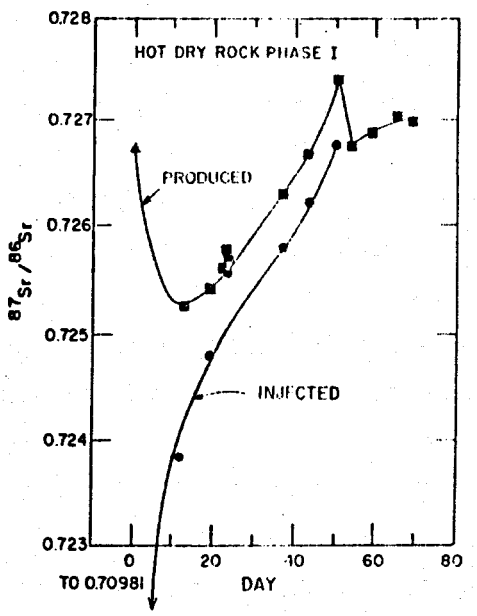

Fig. 5-23.
$^{87}Sr/^{86}Sr$ ratio history during Phase I in the injected and produced fluids.

which the rate of addition of ^{87}Sr-rich Sr from the reservoir is constant. This implies a constant net rate of chemical interaction between rock, circulating fluid, and indigenous pore fluid.

The injected fluid datum for day 23 is not included in the E curve. At this time a sharp drop in impedance occurred and because of associated pumping difficulties the injected water plus a significant fraction of permeation flow returned up GT-2, was passed through the heat exchange modules, and was directed into the EE-1 holding pond. Consequently, the 23E sample does not represent produced water mixed with makeup water as supplied by the 122-m-deep water well.

Between days 50 and 55 there is a decrease in the $^{87}Sr/^{86}Sr$ of G water. In this period there were no significant changes in flow rates or impedances. But as pointed out earlier in Section 4.3, the declining average fracture inflation pressure caused a flow-back phenomenon from permeation, which reduces the nominal water loss rate and provides a new source of fluid. The observed $^{87}Sr/^{86}Sr$ decrease may indicate a change in the rock-pore fluid interaction. Furthermore, other effects such as pore pressure induced fracturing and/or thermal stress cracking may expose a fraction of the circulating fluid to new rock surfaces as well as indigenous pore fluid. "Fresh" rock exposed by the cracking may result in this case in the preferential dissolution of $^{87}Sr/^{86}Sr$-poor and consequently, low Rb/Sr mineral(s). The apparent rapid change in the Sr ratio after day 55 suggests that these $^{87}Sr/^{86}Sr$-poor minerals react rapidly with the water, and by day 55 a different rock-water interaction regime is established.

However, because of the complexity of the downhole environment these postulated effects should be viewed with an appropriate degree of caution. The only unequivocal fact that remains from the Sr isotope data is that distinct changes occurred in $^{87}Sr/^{86}Sr$ during the 75-day experiment and these appear to correlate well with other observed changes.

As noted earlier the average temperature of the produced fluid at the end of segment 2 was only 90°C as compared to an initial value of 175°C. Laboratory experiments on rock samples conducted at 300 and 200°C show not only slower dissolution rates and solubilities at the lower temperatures but also changes in the order of the reactivity of the minerals.[2,11] Extrapolating to temperatures below 200°C, these data may suggest that changes in the isotopic ratios could occur solely because of temperature effects.

Unresolved is the following question: what mineral-water interaction is dominating the observed rock-water Sr isotopic effects? The average of

$^{87}Sr/^{86}Sr$ of 15 "whole-rock" biotite granodiorite samples from the cores is 0.7255 ± 40. This value and its error include the whole range of $^{87}Sr/^{86}Sr$ fluid values observed. If we accept 0.7255 as the whole-rock value (indicated by the symbol ▲ on Fig. 5-23), then we conclude that the Sr from rock-water interactions is dominated by minerals with $^{87}Sr/^{86}Sr$ greater than the average rock. Biotite is a likely candidate and the measured $^{87}Sr/^{86}Sr$ of biotite separated from the rock is 0.80278 ± 0.000010. This is, however, in marked contrast to the laboratory experiments, which indicate biotite is among the least reactive phases. Another possible mineral is potassium feldspar, which in some rocks is enriched in $^{87}Sr/^{86}Sr$ relative to the average rock. Laboratory experiments show this mineral is among the most reactive and thus would appear more reasonable as the mineral providing the Sr and dominating the isotopic effects.

In summary, the Sr isotopic measurements have successfully been used to monitor mixing of fluids from different sources and to indicate when rock-water interactions in a continuously circulating system are in "steady-state" with respect to the production and depletion of Sr. Furthermore, there is some evidence that Sr data record changes in rock-water interaction regimes due to temperature changes or exposure, or both, of "fresh" rock due to thermal or mechanical cracking.

Experiments to determine Sr element abundances in the water and minerals and to determine the isotopic composition of Sr in the minerals composing the Fenton Hill reservoir rock are in progress. These data will facilitate quantitative mass balance calculations for rock-water interactions in the reservoir.

5.4. Radon (P. Kruger*, L. Semprini*, G. Cederberg*, R. Potter)

Radon measurements are useful for obtaining two types of geothermal reservoir data: (1) structural properties of the reservoir as they affect the emanation of radon from rock to pore fluids, and (2) fluid flow properties of the reservoir as they affect radon transport to the wellhead.

Radon has a set of properties which make it a useful internal reservoir tracer. First, radon is the radioactive noble gas produced in nature from decay of radium dispersed in the earth's crust. The principal isotope of radon is 3.83-day ^{222}Rn resulting from alpha-particle emission from 1600-yr ^{226}Ra, which in turn is produced in the natural uranium series originating with a 4.5×10^9 ^{238}U. Since radon is produced essentially "forever" in the reservoir but decays

* Stanford University, Stanford, California

with its characteristic 3.83-day half-life when separated from its radium parent radionuclide in the formation, it introduces a "time element" in tracer studies. This property of radon contrasts sharply with the stable gas components of geothermal fluids, such as CO_2, H_2S, and O_2 isotopes.

Radon concentration in geofluids depends on several reservoir parameters, primarily the concentration and distribution of radium in the reservoir formation, the conditions for emanation and diffusion into the pore and circulating fluids, and the transport properties of the convecting fluids from the reservoir emanation sites to the producing wellhead. These parameters, in turn, are related to different geologic factors. Radium is found rather uniformly distributed in sedimentary and igneous rocks at an average concentration of about 1 pg/g. Its distribution depends on the local thermodynamic and hydrochemical history of the formation. Since radium is a chemical homolog of the alkaline earth elements calcium, strontium, and barium, it can become redistributed with these elements in hydrothermal regions.

The emanation of radon in rock matrices depends on the chemical, mineral, structural, and thermodynamic properties of the rock. The recoil energy of ^{222}Rn on alpha decay of ^{226}Ra is 86 keV, sufficient to migrate about 1 μm in rock. The emanation from the rock is thus strongly dependent on the surface area exposed, the porosity, and the composition of the cementing materials in the rock, as noted by Andrews and Wood.[15] It is also dependent on the pressure, temperature, and density of the pore fluid in the formation. The transport of radon depends on its solubility in the convecting fluid and the hydrodynamic properties of the reservoir, such as permeability-thickness, reservoir pressure gradients, and flow rate.

Two general types of information may be obtained with radon as an internal reservoir tracer. Under steady flow conditions, changes in reservoir properties will result in changes in radon concentration in the produced geofluids. Under steady emanation conditions, changes in flow regime will also result in changes in radon concentration. A discussion of some of the types of information that can be obtained from radon measurements was given by Kruger, Warren, and Honeyman.[16] The challenge of successfully applying radon transient analysis to geothermal reservoir engineering rests with the ability to show the relationships between changes in reservoir or flow properties and changes in radon concentration. Sufficient data are needed to separate the changes due to each effect.

In a particular case, radon measurements were used to study changes in fracture permeability in geothermal systems as noted by Stoker and Kruger.[17]

This section reviews the experimental radon data obtained during the first 75 days of the LASL Phase I experiment and is the first attempt to study radon emanation in a hydraulically-fractured geothermal reservoir. During the 75-day period, five samples were collected at the producing wellhead and shipped to the nuclear civil engineering laboratory at Stanford, where the radon concentration was measured by the method developed by Stoker and Kruger.[17] The system was shut in for 11 days after the flow test period and then vented. Two samples of wellhead fluid were collected during this latter venting period. To obtain a background value of radon due to radium dissolved in the makeup water, one sample of makeup water was collected during the flow test period.

The concentration of ^{226}Ra in the formation rock was reported by L. M. Marple and R. M. Potter as 1.7 ± 0.18 pCi/g determined by gamma-ray spectroscopy at LASL. To determine the fraction of radon due to dissolved radium in the recirculating fluid, double-extraction measurements of radon were made in one of the five flow-test samples and in the makeup water sample. In this method, the fraction of radon in the original wellhead sample due to dissolved radium is determined by complete initial removal of the radon from the sample, then allowing radon to reestablish equilibrium with the dissolved radium, and removing the radon a second time for measurement.

The wellhead conditions and the radon concentration values for the samples analyzed during the Phase I test are given in Table 5-V. Readily apparent over the 73 days of the flow period is the marked increase in radon concentration coupled with the continuous decrease in wellhead fluid temperature and the continuous increase in flow rate. Also apparent in the data is the rapid decrease in radon concentration during the 3 days of venting the system. Table 5-V also shows that the radon concentration due to dissolved radium in the GT-2 produced sample of day 65 was 0.0083 nCi/ℓ compared to a total radon concentration of 1.7 nCi/ℓ. Thus dissolved radium accounts for only 2% of the total radon observed in the wellhead fluid. The double-extraction method for radon in the makeup water sample showed a total radon concentration of 0.0075 nCi/ℓ (corrected to time of sampling) with dissolved radium contributing 0.0018 nCi/ℓ ($\sim$24%).

The experimental data in Table 5-V show a quasi-exponential growth of radon concentration in the recirculated fluid over the 75-day flow test period, a

TABLE 5-V

RADON DATA - PHASE I TEST
JANUARY 28 - APRIL 27, 1978

CIRCULATING SYSTEM
(GT-2 PRODUCING WELL SAMPLES)

Test Day	T (°C)	$\dot{q}$ ℓ/min	$\dot{q}$ (gpm)	Q^a 10^6ℓ	Q^a (10^6 gal)	(Rn) (nCi/ℓ)
0.3	∿170	208	(∿55)	0.08	(0.02)	0.17 ± 0.02
18.9	130	424	(112)	10.6	(2.8)	0.10 ± 0.10
38.2	100	852	(225)	35.2	(9.3)	0.58 ± 0.05
65.9	90	897	(237)	69.3	(18.3)	1.7 ± 0.2
73.1	90	927	(245)	77.6	(20.5)	2.8 ± 0.3
		VENTING SYSTEM (GT-2 WELL SAMPLES)				
86.1	80	416	(110)	80.3	(21.2)	2.3 ± 0.2
89.2	80	≤95	(≤25)	85.2	(22.5)	0.50 ± 0.06
		MAKEUP WATER				
65.9	-	-	-	-	-	0.0075
		RADIUM CONTENT (RADON DUE TO DISSOLVED RADIUM)				
65.9 (for GT-2 produced fluid)	80	897	(237)	69.3	(18.3)	0.0083
65.9 (for makeup)	-	-	-	-	-	0.0018

[a] Total produced fluid volume.

rapid decrease in radon concentration during the venting period, and a low concentration of dissolved radium in both the makeup and circulating fluid.

The radon concentration growth history during the flow period and the decay history during the venting period are shown in Fig. 5-24. The first sample, collected 6 h after initiation of the flow test period, represents water that was resident in the fracture system during the ∿3-month shut-in period prior to the test. Since the shut-in period was longer than 1 month (large compared to the 3.83-day half-life of ^{222}Rn), the radon concentration should have been in equilibrium with the radon emanation from the fractured rock surface. The initial concentration of 0.17 ± 0.02 nCi/ℓ can be considered representative of the radon concentration in the main fracture volume of the large hydraulic fracture system. The second sample was collected after 20 days of flow during which time the flow rate increased by a factor of two and the average reservoir temperature declined steadily from 170 to 130°C. This sample showed a radon concentration of 0.10 ± 0.10 nCi/ℓ, smaller than the initial sample. The uncertainty of this sample is very large (±100%) due to an unfortunate delay in shipping between collection and analysis, resulting in an alpha-particle measurement close to counter background and a large-decay correction factor to sampling time. However the measured concentration may be correct, and the lower value of 0.1 nCi/ℓ may represent the effect of dilution of the shut-in volume of water with makeup water, which is noted during this period to have exceeded 151 ℓ/min (40 gpm) when the flow rate was reaching 379 ℓ/min (100 gpm).

The third sample, collected on day 38 when the system dynamics were reaching steady state, shows the initiation of a rapid rise in radon concentration up to the end of the Phase I flow test at day 75. The rise is shown in Fig. 5-25 as an exponential growth, given by the equation

$$[Rn] = [Rn]_0 \, e^{+kt} \quad , \tag{5-17}$$

where $[Rn]_0$ = initial fracture-volume concentration (0.17 nCi/ℓ) uncorrected for dilution with makeup water, and k = growth constant for the system function of (Q, T, P).

Although the radon concentration exhibits an exponential growth pattern during the test period, it cannot continue to rise indefinitely, but must reach some steady-state concentration given by maximum emanation of radon from the

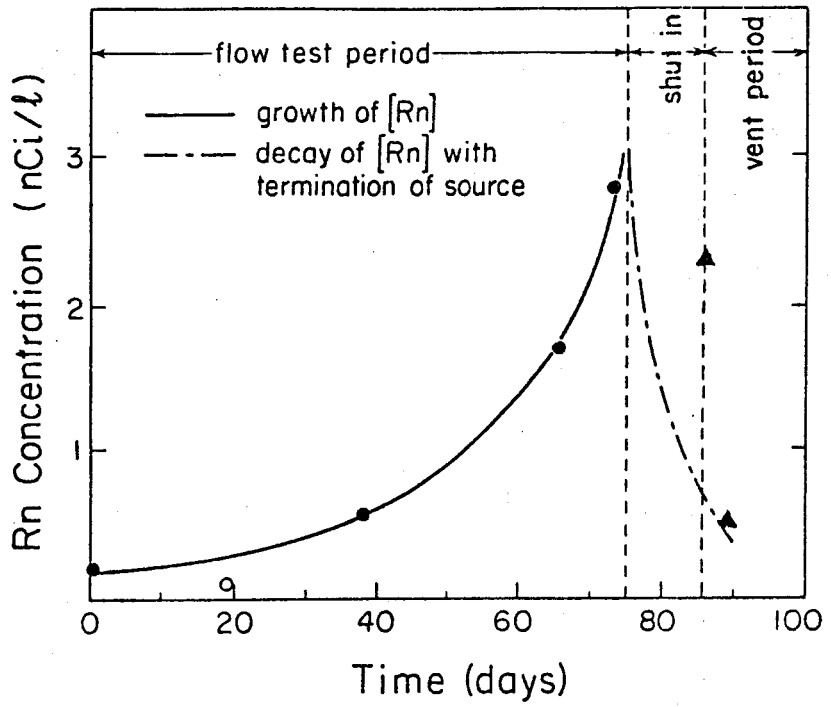

Fig. 5-24.
Radon concentration in the produced fluid.

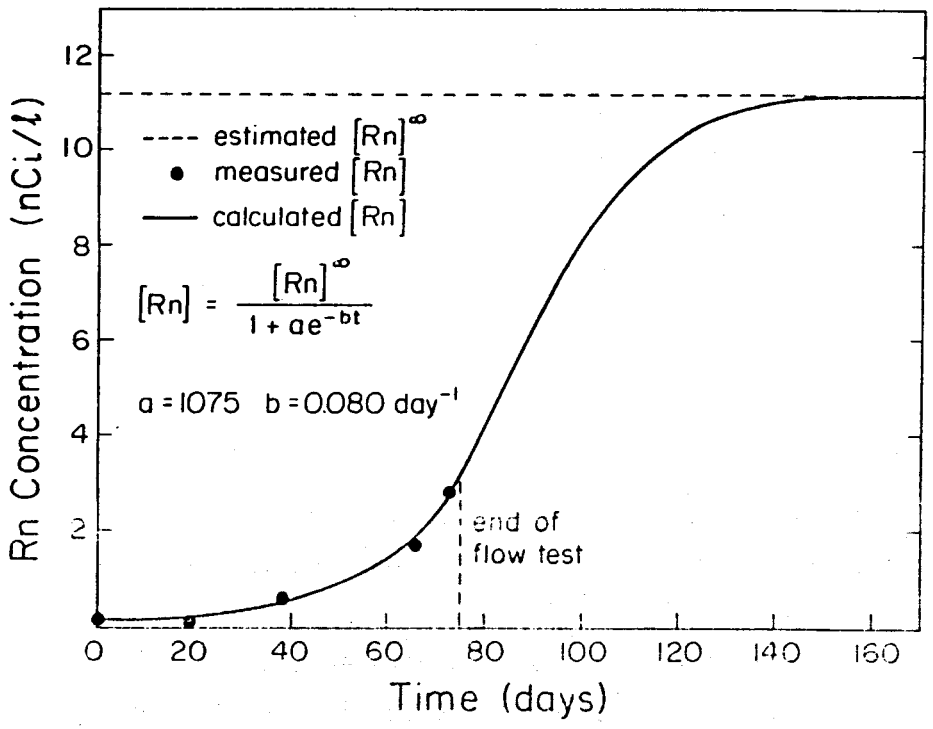

Fig. 5-25.
Observed and predicted radon concentration in the produced fluid.

radium concentration in the formation rock. The trend toward saturation is noted in the nonconstancy of the growth constant, k, and its counterpart, the growth half-life, τ, given by $\tau = \ln 2/k$, as shown below:

Sample Range	k (day^{-1})	τ (days)
1 - 3	0.032	21.8
1 - 4	0.035	19.9
1 - 5	0.038	18.1
3 - 4	0.039	17.8
4 - 5	0.071	9.7

Several mechanisms could potentially explain the observed quasi-exponential rise in radon concentration over the 75-day Phase I flow period. They include: (a) continuous dissolution of radium from the exposed rock surfaces into the recirculating water, (b) increase in solubility of radon in the circulating fluid as the temperature of the rock-water system decreases, (c) increase in the emanating power of the radon by recoil or diffusion from the fractured rock to the circulating fluid, and (d) increase in the area of the fractured rock surface (at constant emanating power) through increased fracturing of the formation by the recirculating fluid pressure and temperature differential.

Table 5-V showed that the dissolved radium concentration in the day 65 wellhead sample accounted for only about 2% of the total radon present in the sample; the value was not much larger than the radium initially present in the makeup water. Both radium values are sufficiently small to preclude the dissolution of radium from fractured rock as the reason for the observed growth in radon concentration over the Phase I flow test period.

The solubility of radon in water is significant at low temperature and decreases rapidly with temperatures above 0°C.[18] The value of 86 cm^3/ℓ at 70°C and 1 atm pressure does not change greatly in the temperature range of 90 to 170°C. Table 5-V notes the decrease in wellhead temperature from 170 to 90°C during the 75-day flow test. This temperature drop might affect the radon concentration in two ways: an increase in emanating power of radon and an increase in its solubility. Since the emanating power is expected to increase with the larger diffusion coefficients at increased temperature (at constant pressure and pore fluid density), it is difficult to accept the inverse

relationship. And unless there is a stagnant volume in the system where degassed gaseous components can accumulate or bypass the wellhead collection site, it is difficult to visualize how a potential for degassing in the closed recirculation system could occur. Therefore, the growth in radon concentration over the flow test period cannot, at this time, be attributed to the decrease in reservoir temperature.

The distinction between increased emanating power and increased fracture surface area is difficult to make. There are few experimental data available on emanating power of radon from geothermal rock mediums. Research is currently underway as part of the Stanford Geothermal Program to determine the dependence of radon emanation power on the thermodynamic conditions of pressure, temperature, and pore fluid density in fractured rock formations.

A reasonable speculation at this time is that the most likely factor contributing to the observed increase in radon concentration is the increase in new surface area created during the experiment. Based on downhole spinner and temperature measurements in GT-2B and compositional changes occurring in other critical chemical species such as SiO_2, Cl, Na, K, and HCO_3, a fraction of the circulating fluid is being exposed to additional surface area by newly created flow paths, which apparently penetrate into hot regions of the reservoir rock containing indigenous pore fluid. At this time, it is difficult to say whether pressure fracturing, thermal stress cracking, or permeation is the source of these new flow paths. If the surface area of new fractures or flow paths increases at a rate greater than the increase in fracture volume (and assuming even a constant emanating power under these conditions), the radon concentration in the recirculating water would be expected to increase. As noted earlier, however, a saturation concentration would eventually be reached, given by a logistics equation

$$[Rn] = \frac{[Rn]^{\infty}}{1 + ae^{-bt}} \quad , \tag{5-18}$$

where

[Rn] = infinite-time steady-state radon concentration for finite radium concentration and constant emanating and thermodynamic conditions

a,b = empirical constants.

An attempt to fit the measured radon concentrations with an estimated $[Rn]^{\infty}$ value is shown in Fig. 5-25. The value for $[Rn]^{\infty}$ was obtained from the relation

$$[Rn] = \frac{[Ra]\ (EP)}{\phi} \tag{5-19}$$

where

[Rn] = radium concentration

(EP) = emanating power

ϕ = porosity.

From the LASL value of 1.7 pCi/g for the radium concentration in the rock, and assumed values of (EP) ≃ 0.1 and $\phi \simeq 0.01$, a rock density of 2.5 g/cm^3, the radon concentration in the fracture volume would be [Rn] = 42.5 nCi/ℓ. For a dilution based on values of the main fracture volume ≃ 54 883ℓ (14 500 gal) and total circulation volume ≃ 208 175ℓ (55,000 gal), the radon concentration in the wellhead fluid would be $[Rn]^{\infty}$ = 11.2 nCi/ℓ.

A least squares fit of Eq. (5-18) to the data in Fig. 5-25 gives values to the two empirical constants of a = 1075 and b = 0.080 day^{-1}. The curve, based on the estimated value of $[Rn]^{\infty}$ = 11.2 nCi/ℓ, indicates that equilibrium would have been achieved if the test had run an additional 2 months. It will be interesting to confirm the values of the empirical constants a and b in future flow tests in the EE-1/GT-2 system.

Figure 5-24 also shows the results of the radon measurements made during the venting part of the Phase I test. The first of the two post-flow samples represents water in the main fracture on day 86 of the test with pressure maintained in the shut-in system. The radon concentration remained at an elevated value of 2.3 nCi/ℓ 11 days after shut in, as contrasted to an expected value of 0.67 nCi/ℓ based on radioactive decay of the dissolved radon if the mechanism for the growth during the flow period were cut off with shut-in of the system. The implication is that the source of radon continued under the pressure conditions reached during the flow period to shut-in. However, the second sample on day 89, collected after fluid pressure reduction shows a radon concentration of 0.5 nCi/ℓ consistent with radioactive decay to pre-flow conditions. The wellhead water obtained for this sample however may not represent fluid from the fracture system due to gas fractionation at the wellhead resulting from depressurization.

An explanation for the sustained high value of Rn may be a flow from permeation into the GT-2B open hole exiting then to the EE-1 annulus through the main flow system. This permeation flow would carry additional Rn to compensate partially for the decay of Rn in the wellbore fluid.

Downhole samples taken later in the vent period on July 27, 1978 showed considerably higher Rn concentrations of 3.3 nCi/ℓ. Samples were taken with the downhole water sampler at the 2590-m (8500-ft) depth in GT-2B which is 46 m (150 ft) above the highest producing zone.[2] This was done to avoid the long borehole residence time and subsequent decay at the low venting rate of 8 ℓ/min (∿2 gpm). In addition, 1900ℓ (∿500 gal) of fluid was pumped into EE-1 with GT-2 vented, and another sample was taken; this time the Rn concentration had decreased to 1.4 nCi/ℓ. Because the experimental error is ≤10%, the difference in concentration between the two samples is real. One possible mechanism is dilution between EE-1 wellbore fluid and fluid which has equilibrated with the fracture system. Because the venting Rn concentration of 3.3 nCi/ℓ is drastically higher than the initial Rn concentration of 0.17 nCi/ℓ, an alternate source of Rn is suggested. During the latter venting period, a very small return flow rate of 8-19 ℓ/min (2-5 gpm) was observed in the GT-2B wellbore. This fluid is returning as permeation stored fluid quite likely in contact with the fine-grained rock matrix of the reservoir, whereas the original flow sample collected on day 0 (see Fig. 5-24) consisted of fluid contained in a self-propped hydraulic fracture system with little or no returned flow from permeation. Consequently, the higher Rn concentration observed is probably caused by a higher effective emanation power of radium exposed to fluid returning via matrix flow.

6. MONITORING FOR INDUCED SEISMIC EFFECTS (C. Newton, J. Albright, R. Potter, and R. Butler)

During Phase I, Segment 2 of the HDR geothermal demonstration, seismic monitoring was done to detect local seismic sources and to discriminate among several possible source types, such as man-made disturbances, earthquakes, and rock failure induced by the pressurized fluid injection into the inlet well of the HDR system.

The monitoring array consisted of seven surface stations at distances up to 750 m from the wells, two shallow borehole stations (∿125-m deep) at about 1 and 3 km, and stations of the LASL regional seismic network -- the nearest of which is about 10 km away. The two borehole stations were positioned a few meters below the Permian sandstone - Quaternary tuff interface.

The only local earthquakes identified during the loop operation were located by the regional array near a fault 15 km west of the HDR geothermal site (see Fig. 6-1). These three events, and a fourth that occurred in May, were in the same epicentral zone as a swarm of earthquakes that were observed in late September 1975. The largest event observed to date had a local magnitude, M_L = 3.2. These small earthquakes may be premonitory activity to a much larger earthquake (whose magnitude and time of occurrence are not yet predictable), which might occur sometime in the next few years. Figure 6-1 shows the capability of the regional network to locate microearthquakes in the vicinity of Fenton Hill. For $M_L > 0.0$ more than five stations can be used to locate the epicenter (Fig. 6-1 a,b,d), but as the magnitude approaches -1.0 the existing network is close to its location-limiting threshold (Fig. 6-1 c).

There were many blasts, sonic booms, and earthquakes observed with more distant epicenters. Some of the smaller of these acoustic signals needed positive identification by the seismograms of the regional network.

The background noise was generally high during the day, beginning with sunrise thermal expansion of the metal buildings, which shelter the surface seismic stations. These amplitudes of noise bursts frequently exceeded levels expected for M_L = 1.0 earthquakes. At night, however, the background noise was nearly always below signal levels for M_L = -1.0 earthquakes.

Although it is likely that $M_L < 0.0$ earthquakes would not have been identified during the daytime, the absence of detectable, induced earthquakes with $M_L > -1.0$ at night is reasonable evidence that none with $M_L > 0.0$ occurred during the loop operation. Although the stress alterations to the reservoir during the

nearly 3 months of the loop operation were significant but not overwhelming [5 677 500ℓ (1 500 000 gal) of water in situ, pressures to 1400 psi above hydrostatic, and nearly 250 MW-days of thermal energy removed] the absence of detectable earthquakes (i.e., $M_L > -1.0$) is an encouraging observation. The seismic monitoring will continue with an improved network during future flow experiments.

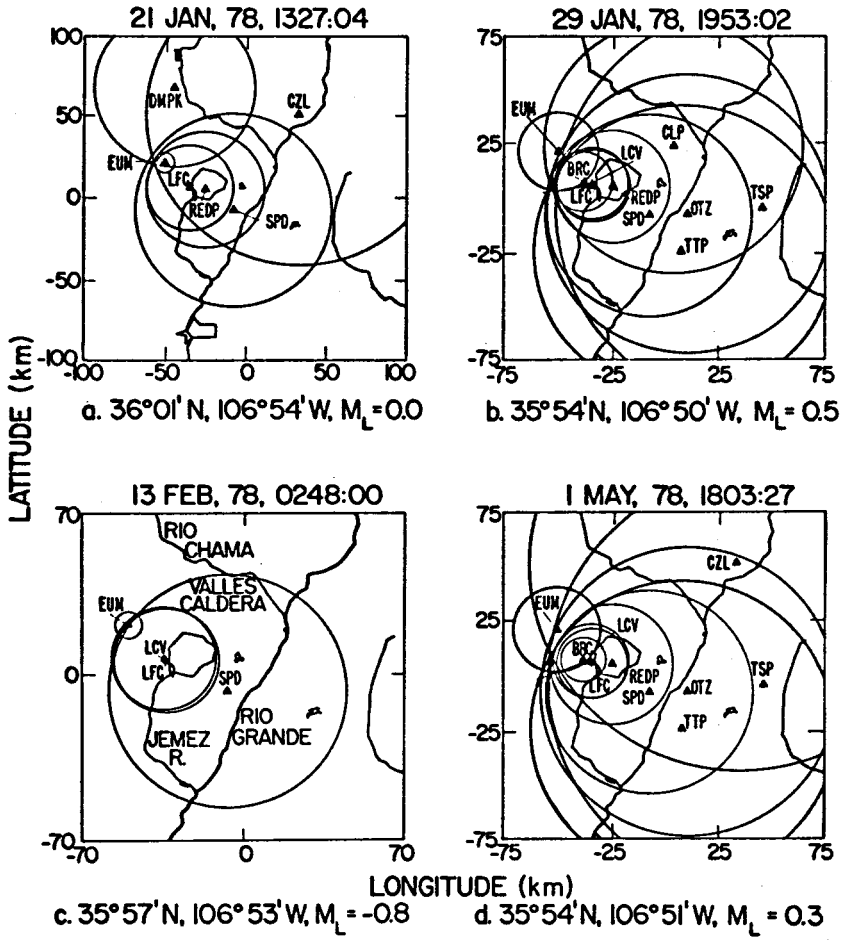

Fig. 6-1.
Calculated epicenters for four earthquakes near Señorita, New Mexico.

7. SUMMARY OF SYSTEM PERFORMANCE AND MODELS (J. W. Tester and J. N. Albright)

A brief review of the redrilling program at Fenton Hill, which culminated in the completion of the present GT-2B/EE-1 connected fracture system, is presented in Figs. 7-1 through 7-4. Projections showing the bottom sections of EE-1 and GT-2 with GT-2A and GT-2B, the sidetracked hole sections, are shown in Figs. 7-1 and 7-2. The redrilling was completed in the following sequence: GT-2 (December 1974), EE-1 (November 1975), GT-2A (May 1977), and GT-2B (June 1977). A complete description of the drilling activity between 1975 and 1977 is contained in Project reports (LASL HDR Project Staff, 1978[2]). GT-2B is cased through the sidetrack points from GT-2 and GT-2A. Figure 7-3 is a horizontal projection to a vertical plane parallel to the most probable direction of a main hydraulically induced fracture (NW-SE) and perpendicular to the least principal horizontal stress. A low impedance flow between wells was finally achieved by the redrilling, which entered a region of the reservoir with increased permeability due to hydraulic fracturing. Because of the low formation breakdown pressures (100 bar or 1500 psi) encountered, previously sealed natural fractures were probably opened.

The current production system at Fenton Hill is represented schematically in Fig. 7-4. GT-2B terminates at 2707 m (8882 ft) and EE-1 at 3050 m (10 007 ft), a greater depth than represented in the figure. Both wells penetrate basement rocks at approximately 732 m (2400 ft) and terminate in biotite granodiorite. Four fractures in GT-2B account for 90% of production. In order of decreasing flow, the fractures are located at 2661 m (35%), 2719 m (25%), 2687 m (20%), and 2706 m (12%). GT-2B is cased to 2603 m (8541 ft) and openhole from there to the bottom. The bottom of the casing in EE-1 is at 2919 m (9578 ft), but 90% of the flow moves behind casing in a poorly cemented region from 2919 to 2759 m (9578 to 9050 ft) where it enters the reservoir through a hydraulic fracture. Water then moves vertically 64 m (210 ft) before the lowest entry point in GT-2B is reached. Several other fractures over the depth interval of 2134-2941 m (7000-9650 ft) accepted water on pressurization of EE-1, but this accounts for only a small percentage of the injection into the reservoir. The injection zone at 2941 m (9650 ft) accepts up to 5% of the flow.

A synthesis of geophysical logging data, core studies, and pertinent results of the pressure, temperature, and flow measurements acquired to date at Fenton Hill are presented in Fig. 7-5. Shown is the projection of the four wellbore sections onto a northeasterly striking vertical plane. Bulk rock properties of

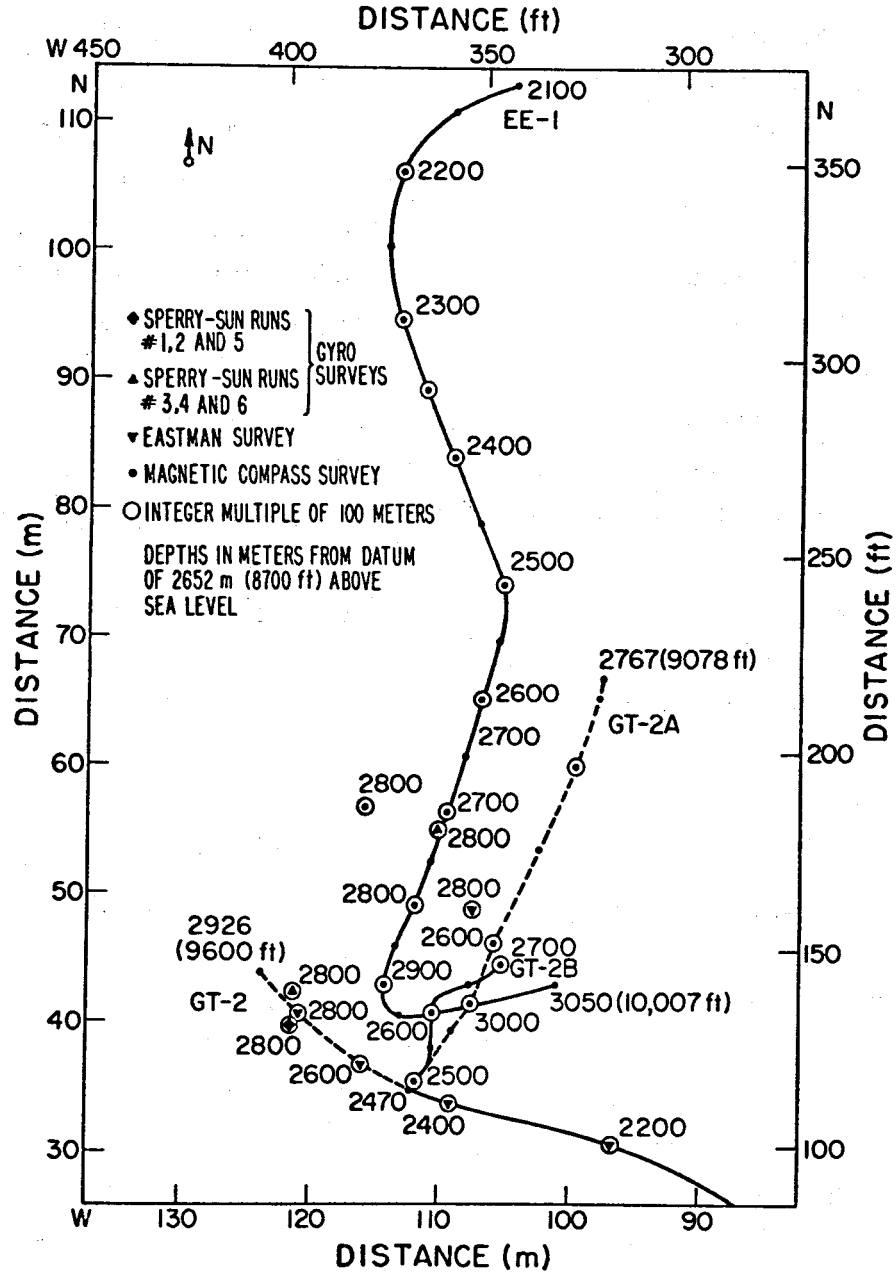

Fig. 7-1.
Plan view projections of the lower sections of the GT-2 and EE-1 wellbores.

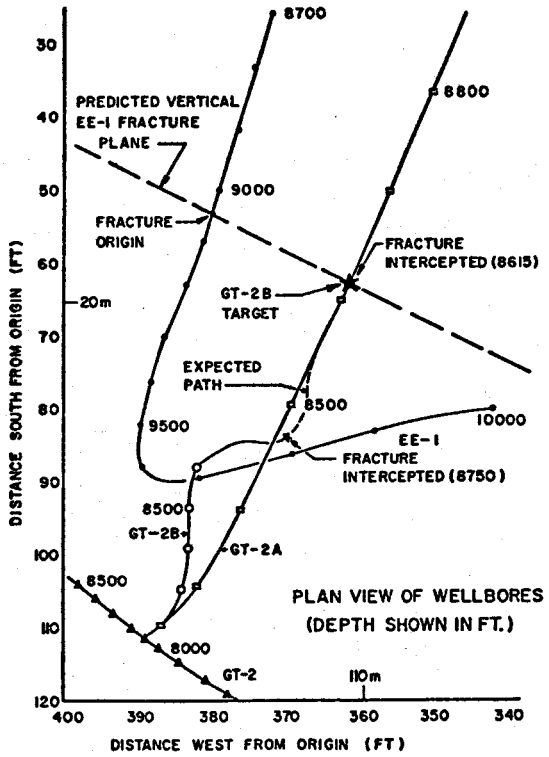

Fig. 7-2.
Enlarged plan view of the lower sections of the GT-2 and EE-1 wellbores.

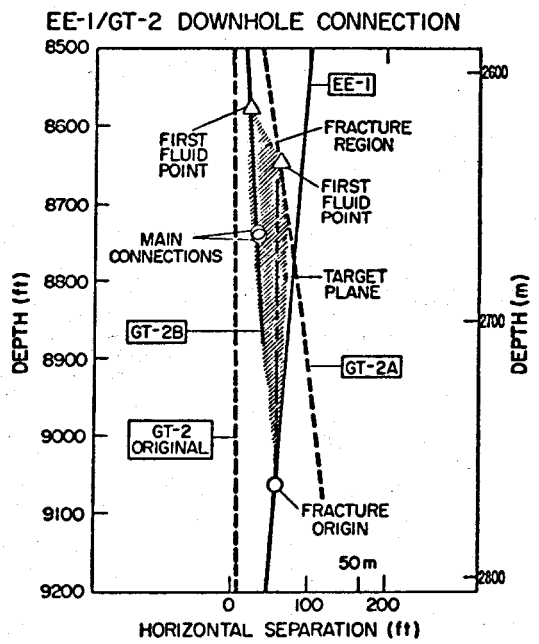

Fig. 7-3.
Elevation view of the GT-2 and EE-1 wellbores parallel to the NW-SE direction.

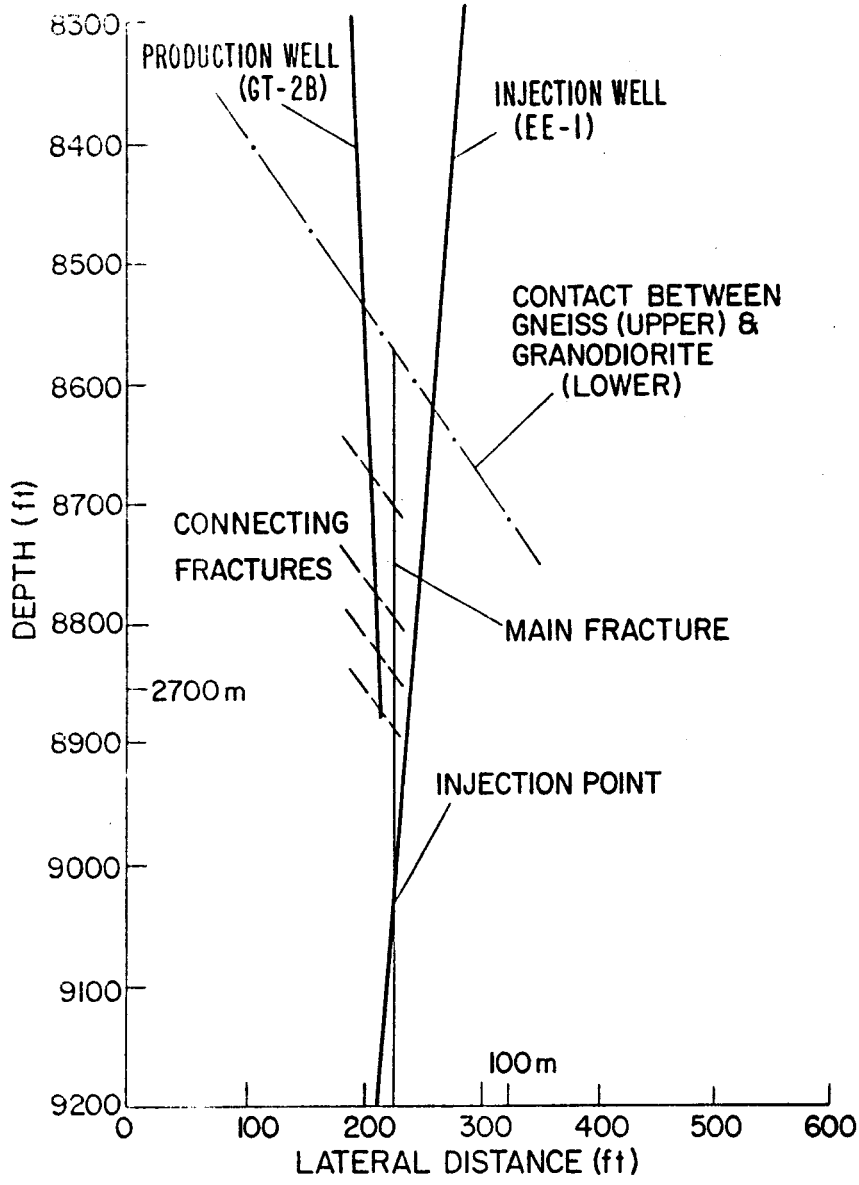

Fig. 7-4.
Simplified schematic of the GT-2B/EE-1 connected fracture system.

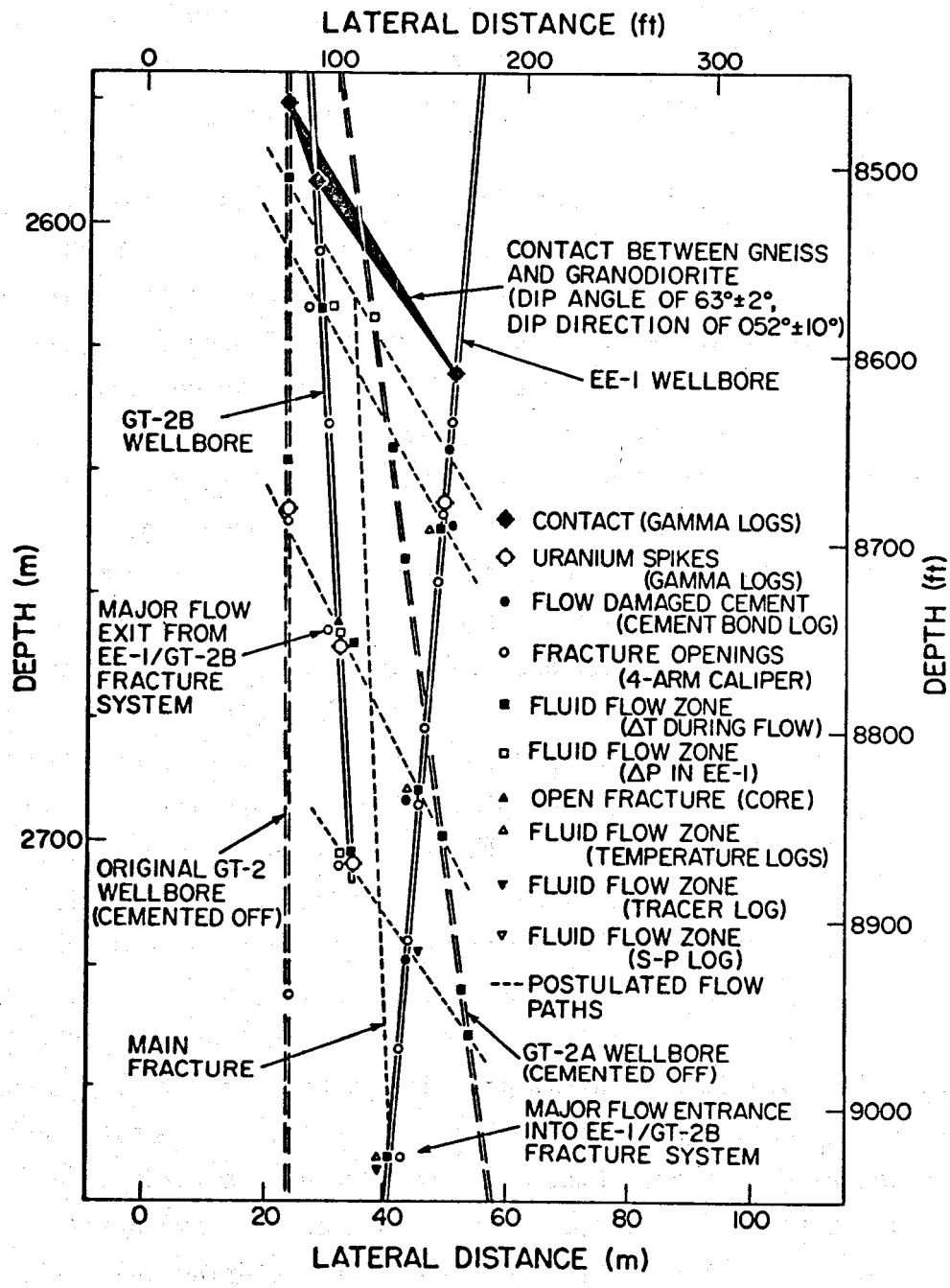

Fig. 7-5.
Elevation view showing GT-2, GT-2A, GT-2B, and EE-1 wellbores with geophysical information shown and the fracture model depicted with dotted lines.

the reservoir have been determined through pressure and flow testing, analysis of cores,[19] and geophysical logs.[2] The properties of individual fractures accepting or producing fluids were established, where and when possible, in terms of flow fraction, temperature, trace of wellbore intersection, and probable secondary mineralization.

The principal geologic feature in the reservoir is a contact between granitic gneiss and granodiorite lithology, which effectively caps the region of heat extraction. Hydraulic stimulation of the reservoir has resulted in gaining access to a system of at least two definable sets of previously existing fractures for use as heat exchange surfaces. The first may consist of vertical fractures that are parallel, uniformly spaced (~10 m), and northwesterly striking. They are characterized by low flow impedance at intersections with wellbores as well as low internal impedance due to self propping. Injection into the reservoir is principally through an incompletely isolated member of this set. A second set of fractures, as steep as 60°, are roughly coplanar with the gneiss-granodiorite contact and have an order of magnitude higher impedance to flow. GT-2B production comes from several of these high angle fractures. Very little is known about the spatial relationships between fractures not penetrated during drilling because of the inherent complexity of the reservoir; therefore details of the flow between wells in the fracture system can only be inferred. The path for the current production (Fig. 7-5, dashed lines) satisfies established criteria. In addition, temperature logs, fluid geochemistry, and fluid residence time studies suggest that a secondary flow path exists, with a possible entrance passing through a hydraulic fracture originating at 2940 m (9650 ft) in EE-1. This secondary flow path may provide a source of hot fluid, which contains a relatively high concentration of silica, chloride, bicarbonate, and radon thus explaining the rise in concentration observed during the 75-day run. Because the final silica concentration was saturated with quartz at approximately 185 to 200°C, fluid of at least this temperature must be entering the GT-2B wellbore. The high chloride concentration suggests a mechanism of pore fluid displacement and mixing before entering the GT-2B wellbore, because the origin of chloride is most likely not caused by dissolution of the rock.

Although a model that uniquely describes all facets of the data from Phase I and earlier experiments cannot be specified at this time, the results of the 75-day test have provided an extremely valuable experience with a prototype hot

dry rock system in low permeability rock, and it will facilitate expansion to a much larger capacity Phase II system.

The main observations, in fact, suggest a very optimistic future for hot dry rock. Reservoir flow impedance decreased from an initial 16 bar-s/ℓ (15 psi-gpm) to about 3.3 bar-s/ℓ (3 psi/gpm) by both continuous and discontinuous drops in impedance with an increase in reservoir volume as shown by tracer studies. Permeation water-loss rate quickly decreased to less than 0.19 ℓ/s (3 gpm) which is <1-1/2% of circulation rate and could be modeled by one-dimensional transient flow in a homogeneous reservoir. Geofluid chemistry is most acceptable, with 1550-2000 ppm total dissolved solids and no evidence of scaling in main flow passages in the reservoir or surface equipment. Thermal drawdown for the first small prototype system followed the theoretical prediction for an 8000-m^2 system. The surface facilities and data acquisition systems proved sufficient for a short-term test. There is no evidence of any measurable seismicity induced at the site.

From early experience at Fenton Hill, we thought that flow impedance was going to present a formidable problem because high mass flows of >9.5 ℓ/s (>150 gpm) were not possible with impedances of 11 bar-s/ℓ (10 psi/gpm) and a formation breakdown pressure of 100 bar (∿1500 psi). The 75-day test demonstrated that extended periods of fluid pressurization could significantly lower the impedance without an increase in flow short-circuiting. The dye tracer indicated that well-mixed flow occurs in the fractured region and that the average size or volume of the system increased. Periodic initiation and activation of new flow paths from pore-pressure-induced cracking or thermal stress cracking or both may have caused the observed decline in impedance as well as the change in the apparent system volume. Whatever the mechanism, the reservoir has responded in a dynamic manner. The impedance changes did not however represent significant changes in either the effective heat transfer or effective fluid-permeating area. Thermal drawdown and fluid permeation were adequately modeled with one-dimensional heat and fluid diffusion into the rock from the two-dimensional pressurized fracture of fixed area. Because permeating areas inferred from an acceptable range of average compressibilities and permeabilities for the reservoir are much larger than the 8000-m^2 effective heat transfer area and because flow communication was observed from a hotter region of the reservoir, the <u>potential</u> heat exchange area must be considerably greater.

Further tests of the present reservoir will be aimed at characterizing methods for activation of this larger region of hot rock.

ACKNOWLEDGMENTS

The authors would like to acknowledge M. Brown, G. Nunz, and the late A. Blair for their helpful suggestions and comments in reviewing the manuscript. B. Ramsay and D. Elsner are thanked for their aid in the preparation.

REFERENCES

1 H. D. Murphy, "Thermal Stress Cracking and the Enhancement of Heat Extraction from Fractured Geothermal Reservoirs," Los Alamos Scientific Laboratory report LA-7235-MS (April 1978).

2. LASL HDR Project Staff, "Hot Dry Rock Geothermal Energy Development Project - Annual Report FY 1977," Los Alamos Scientific Laboratory report LA-7109-PR (February 1978).

3. H. D. Murphy and R. M. Potter, "Fracture and Borehole Mapping Technique Development," in Hot Dry Rock Geothermal Energy Development Project - Annual Report FY 1977, (Los Alamos Scientific Laboratory report LA-7109-PR February 1978), pp. 126-128.

4. R. D. McFarland and H. D. Murphy, "Extracting Energy from Hydraulically Fractured Geothermal Reservoirs," Proceedings of 11th Intersociety Energy Conversion Engineering Conference, State Line, Nevada, 1976.

5. F. H. Harlow and W. E. Pracht, "A Theoretical Study of Geothermal Energy Extraction," Journ. Geophy. Res., 77, (35), 7038 (1972).

6. R. G. Lawton, "WELLBOR - Wellbore Heat Transmission Code," unpublished results (1976).

7. H. N. Fisher, "An Interpretation of the Pressure and Flow Data for Two Fractures of the Los Alamos Hot Dry Rock (HDR) Geothermal System," Proc. of the 18th U. S. Symposium on Rock Mechanics, Keystone, Colorado, June 22, 1977.

8. R. G. Lawton, "The AYER Heat Conduction Computer Program," Los Alamos Scientific Laboratory report LA-5613-MS (May 1974).

9. R. M. Garrels and C. L. Christ, Solutions, Minerals and Equilibria (Harper and Row, New York, 1965), pp. 403-428.

10. G. L. Frear and J. Johnston, J. Am. Chem. Soc. 51, 2082-2093, in Solubilities of Inorganic and Metal Organic Compounds, Vol. I, 4th ed. (A. Siedell, Am. Chem. Soc., Washington, D. C.,1958), p. 539.

11. R. W. Charles, "Experimental Geothermal Loop: I, 295°C Study," Los Alamos Scientific Laboratory report LA-7334-MS (July 1978).

12. W. A. Deer, R. A. Howie, and J. Zussman, Introduction to Rock Forming Minerals (John Wiley and Sons, Inc., New York, 1966), pp. 400-401.

13. J. Johnston and E. D. Williamson, J. Am. Chem Soc. 38, 975-983, in Solubilities of Inorganic and Metal Organic Compounds, Vol. I, 4th ed. (A. Siedell, Am. Chem. Soc., Washington, D. C., 1958).

14. R. Gunnink and J. B. Niday, "Computerized Quantitative Analyses by Gamma-Ray Spectrometry," Lawrence Livermore Laboratory report UCRL-51061 (March 1972).

15. J. N. Andrews and D. F. Wood, "Mechanism of Radon Release in Rock Matrices and Entry into Groundwaters," Inst. of Mining and Metallurgy Trans/Sec. B, 81, No. 792 (November 1972).

16. P. Kruger, G. Warren, and B. D. Honeyman, "Radon as an Internal Tracer in Geothermal Reservoirs," paper presented at 3rd International Conf. on Nuclear Methods in Environmental and Energy Research, ANS/ERDA, Univ. of Missouri (October 1977).

17. A. Stoker and P. Kruger, "Radon in Geothermal Reservoirs," in Proc. Second United Nations Symp. on the Development and Use of Geothermal Resources San Francisco, California, 1975.

18. A. S. Rogers, "Physical Behavior and Geologic Control of Radon in Mountain Streams," USGS Bulletin 1052-E (1958).

19. A. W. Laughlin and A. Eddy, "Petrography and Geochemistry of Precambrian Rocks from GT-2 and EE-1," Los Alamos Scientific Laboratory report LA-6930-MS (August 1977).

APPENDIX A

FRACTURE OPENING BY COOLING

A. INTRODUCTION

When a fracture is cooled, thermal stress cracking normal to the fracture face will probably occur. In addition, there is a shrinkage of the rock normal to the fracture face which produces no stress over most of the fracture face because it is free to move.

If the fracture is unpressurized, then after some long time, proportional to the fracture radius, this cooling will cause the fracture to open. If however, the pressure is high enough to open the fracture, its width will begin to increase immediately. The time required to open the fracture is calculated in this appendix under the following assumptions:

(1) The fracture is penny shaped.

(2) Heat is withdrawn at the same rate over the entire fracture surface.

(3) The heat flow is considered to be one-dimensional, normal to the fracture face.

(4) The rock is impermeable.

A.1 Thermal Contraction of Rock Face

When rock is cooled under these assumptions, the contraction of the rock face is proportional to the total heat withdrawn. Let $\dot{q}(x,t)$ be the net rate of power extraction per unit volume at time, t, at a distance x into the rock from the fracture face. The change in temperature of an element of unit area and thickness dx about x, at time t, is

$$-\frac{1}{\rho c}\int_0^t \dot{q}\, dt \quad ,$$

the shrinkage of dx is

$$\frac{\delta dx}{dx} = \frac{\alpha}{\rho c}\int_0^t \dot{q}\, dt \quad ,$$

and the total shrinkage from o to x is

$$\int_0^x \delta dx = -\frac{\alpha}{\rho c}\int_0^x\int_0^t \dot{q}dt\,dx = -\frac{\alpha Q}{\rho c} \qquad \text{(A-1)}$$

where, if x is sufficiently large, Q is the total energy extracted per unit area of the fracture face. Thus, if energy Q is withdrawn per unit area, the thermal contraction of the rock face is

$$\delta W = -\frac{\alpha Q}{\rho c} \qquad \text{(A-2)}$$

where α is the thermal expansion coefficient of the rock and ρ and c are its density and specific heat, respectively.

The equations of elasticity are independent of the sign of the stress, and since the deflection of the walls of the pillbox-shaped cavity in Fig. A-1 will differ only infinitesimally from that of the penny-shaped fracture when $P > \sigma$ the theory of the penny-shaped fracture[1] may be applied to calculate the inward deflection of the wall when $P < \sigma$. This deflection, which must be overcome by thermal contraction before the fracture opens is $b = 4(\sigma-P)(1-\nu^2)R/(\pi E)$, where P is the internal pressure, σ the normal earth stress, ν is Poisson's ratio, R the radius, and E, Young's modulus. A fracture will begin to open when

$$-\frac{\alpha Q}{\rho c} + \frac{4(\sigma-P)(1-\nu^2)R}{\pi E} = 0 \quad . \qquad \text{(A-3)}$$

Some typical values of these constants for granite are as follows (E, ν, and ρ are typical acoustic log values in EE-1 and GT-2; α and C are taken from Clark[2]):

$E = 8 \times 10^4$ MPa

$\alpha = 8 \times 10^{-6} K^{-1}$

$\nu = 0.25$

$c = 1000$ J $kg^{-1}K^{-1}$

$\rho = 2700$ kgm^{-3}

Using these values, (A-3) becomes

$$Q = 5.04\,(\sigma-P)R \quad . \qquad \text{(A-4)}$$

If cold water enters near the center of the fracture, at temperature T_w, and the rock temperature is T_R, then a reasonable approximation for Q is

$$Q = \frac{2\lambda(T_R - T_w)}{\sqrt{\pi\kappa}} \sqrt{t} \qquad \text{(A-5)}$$

from the standard formula for linear heat diffusion with a step function change in temperature. The thermal conductivity λ of granite is near 2.7 w/m-k,[3] so using the definition $\kappa = \frac{\lambda}{\rho C}$, with the values of ρ and C given above, Eq. (A-5) becomes:

$$A = 2725\ (T_R - T_w)\ \sqrt{t}. \qquad \text{(A-6)}$$

We may equate Eqs. (A-4) and (A-6) and solve for the ratio $R/(T_R - T_w)$ vs $(\sigma - P)$ at fixed t. Some results are given in Fig. A-2. Since both R and $T_R - T_w$ are of the order 100, the most interesting times are those with $R/(T_R - T_w) \simeq 1$. If $P \simeq \sigma$ (i.e., $\sigma - P \leq 10^5$ Pa) cooling helps on the first day. If $P \simeq 0$ (i.e., $\sigma - P \geq 10^7$ Pa) it takes $\sim$5 years to open the fracture by cooling.

REFERENCES

1. I. N. Sneddon, "The Distribution of Stress in the Neighborhood of a Crack in an Elastic Solid," Proc. Roy. Soc. London, A187 (1945) p. 229.

2. S. P. Clark, "Rock Properties Related to Rapid Excavation," in Handbook of Physical Constants PB 184, 767.

3. W. L. Sibbitt, J. G. Dodson, and J. W. Tester, "Thermal Conductivity of Crystalline Rocks Associated with Energy Extraction from Hot Dry Rock Geothermal Systems," Jour. Geophys. Research (to be published 1979).

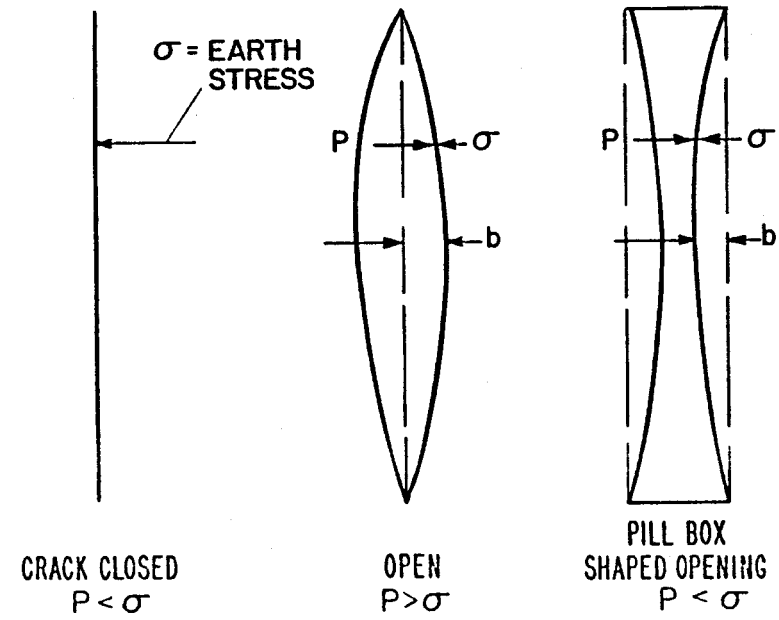

Fig. A-1.
Cavity geometries.

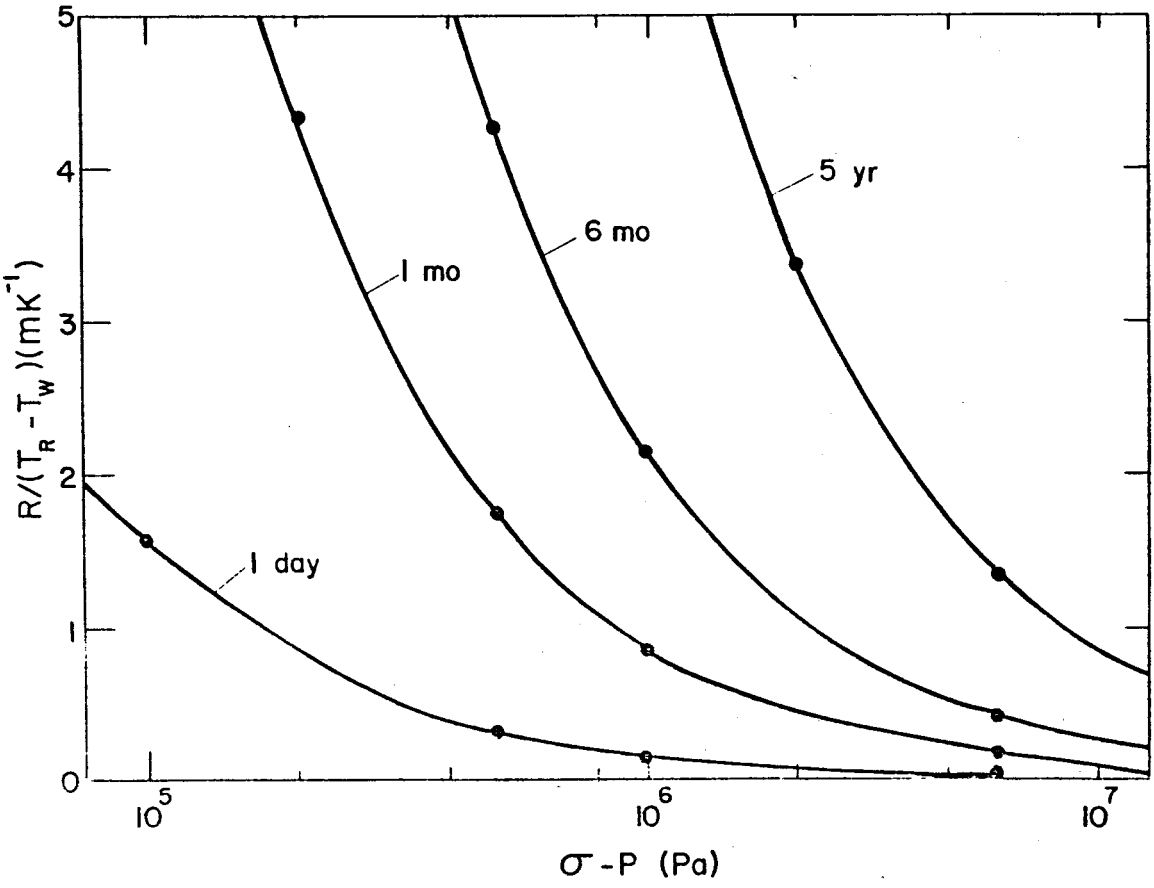

Fig. A-2.
Curves for deriving time for unpressurized fracture to open by cooling.

APPENDIX B

THERMAL EFFECTS IN SPHERICALLY COOLED REGIONS

B. INTRODUCTION

Appendix A discussed the opening of a cooled and pressurized penny-shaped crack. This appendix gives an exact solution for the onset of thermal stress cracking when a spherical portion of a large homogeneous mass of rock is cooled below the surrounding rock temperature by an amount $|\Delta T|$, and pressurized above the pressure of the surrounding rock by an amount $P - P_0$ where P_0 is the pore pressure.

As before in Appendix A, E is Young's modulus, ν is Poisson's ratio, α is a stress in the rock matrix, positive in compression, and α is the thermal expansion coefficient of the rock.

A.1 Displacement at r - a

It is convenient to consider the mass of rock in two parts. The external rock may be modeled as a very thick-walled hollow sphere of internal radius a, with a normal stress σ on the outside and normal stress σ_1 on the inside. The remainder of the rock may be treated as a homogeneous sphere of radius a, subjected to a normal stress σ_1 on its surface and cooled by an amount $|\Delta T|$. By requiring the displacements δa for the external and internal rock to be equal, we may solve for σ_1 for any given $|\Delta T|$.

The displacement of the inner surface of the external rock is given by the expression[1]

$$\delta a = \frac{-\sigma(1-2\nu)}{E} a + \frac{(1+\nu)(\sigma_1-\sigma)}{2E} a \quad . \tag{B-1}$$

The displacement of the surface of the inner sphere arising from the normal stress σ_1 is easily derived from the compressibility,

$$\beta = \frac{1}{K} = \frac{3(1-2\nu)}{E} = -\frac{\delta V}{\sigma_1 V} \simeq -\frac{3\delta a}{\sigma_1 a} \quad ,$$

so

$$\delta a = -\sigma_1 \frac{1-2\nu}{E} a$$

from compression. The displacement due to cooling is $-\delta a|\Delta T|$, so the total displacement is

$$\delta a = -\sigma_1 \frac{1-2\nu}{E} a - \alpha a|\Delta T| \quad . \tag{B-2}$$

By equating (B-1) and (B-2), we have

$$\sigma - \sigma_1 = \frac{2}{3} \frac{\alpha E}{1-\nu} |\Delta T| \quad . \tag{B-3}$$

In this expression, σ_1 represents the stress acting on the rock matrix inside the cooled region. To open an existing fracture under this stress, an internal pressure $P = \sigma_1$ must be applied to the fracture. If a uniform pore fluid pressure P_0 is present throughout the rock, then $P - P_0$ must equal σ_1 in order to open the fracture, i.e., $P = \sigma_1 + P_0 = S_1$, where S_1 is the total stress inside the cooled region. The expression, Eq. (B-3), may also be written as,

$$\sigma + P_0 - (\sigma_1 + P_0) = S - S_1 = \frac{2}{3} \frac{\alpha E}{1-\nu} |\Delta T| \quad . \tag{B-4}$$

In conclusion, the requirement for a preexisting fracture to open in a region where the fluid pressure is P is

$$P + \frac{2}{3} \frac{\alpha E}{1-\nu} |\Delta T| = S \quad ,$$

the total stress in the surrounding rock. In a rock with many weakly cemented fractures, this condition may be considered as describing the onset of thermal stress cracking.

REFERENCES

1. Raymond J. Roark, Formulas for Stress and Strain (McGraw-Hill, New York, 1965), p. 308.

☆ U.S. Government Printing Office: 1979 — 677-013/66